Review

Near-infrared emitting iridium complexes: Molecular design, photophysical properties, and related applications

Yanxin Zhang[1] and Juan Qiao[1,2,*]

SUMMARY

Organic light-emitting diodes (OLEDs) have become popular displays from small screens of wearables to large screens of televisions. In those active-matrix OLED displays, phosphorescent iridium(III) complexes serve as the indispensable green and red emitters because of their high luminous efficiency, excellent color tunability, and high durability. However, in contrast to their brilliant success in the visible region, iridium complexes are still underperforming in the near-infrared (NIR) region, particular in poor luminous efficiency according to the energy gap law. In this review, we first recall the basic theory of phosphorescent iridium complexes and explore their full potential for NIR emission. Next, the recent advances in NIR-emitting iridium complexes are summarized by highlighting design strategies and the structure-properties relationship. Some important implications for controlling photophysical properties are revealed. Moreover, as promising applications, NIR-OLEDs and bio-imaging based on NIR Ir(III) complexes are also presented. Finally, challenges and opportunities for NIR-emitting iridium complexes are envisioned.

INTRODUCTION

Infrared radiation (IR) extends from the nominal red edge of the visible spectrum at 700 nm to 1 mm, corresponding to a photon energy range of approximately 1.7 eV down to 1.24 meV. The infrared band is often divided into three sections of IR-A (700–1,400 nm), IR-B (1,400–3,000 nm), and IR-C (3,000 nm–1 mm) according to the International Commission on Illumination (CIE) division scheme. Alternatively, it is divided into three bands of near-infrared (NIR) radiation (780–3,000 nm), mid-infrared radiation (3–50 μm), and far-infrared radiation (50 μm−1 mm) according to ISO 20473 scheme. The dividing point between visible and infrared light is different in various situations. In the published literatures, NIR-emitting materials usually refer to those with emission peak above 700 nm.

Thanks to its unique properties, NIR-emitting materials are particularly useful for various military and civilian applications, such as night-vision and information-secured displays, infrared signaling, optical communications, biometric identification, bio-imaging, medical diagnostics, and photodynamic therapy (Antaris et al., 2016; Frangioni, 2003; Hilderbrand and Weissleder, 2010; Qian and Wang, 2010; Xiang et al., 2013; Zampetti et al., 2019; Zhang et al., 2018b). Recently, the applications of NIR-emitting materials and devices are becoming more and more common in daily life. Face recognition modules based on active NIR light are carried on hundreds of millions of smart phones to improve the security level of personal privacy, such as iPhone with Face ID and HUAWEI Mate series. Hundreds of millions camera lens and focusing modules employ the time-of-flight of active NIR light to improve the performance of distance detection and focusing speed, such as so-called TOF lens, Laser focusing, and Apple's LiDAR Scanner. NIR light is also employed in photo biomodulation therapy, such as LG's "Pra.L MediHair." All these commercial products have been equipped with point light sources, such as inorganic light-emitting diodes (LEDs) and lasers based on GaAs-related materials, which have various disadvantages, such as low flexibility, relatively heavy weight, and nonuniform effects. The huge market is in urgent need of novel NIR-emitting materials with advanced performance for flexible and wearable devices.

Currently, there are several types of novel NIR-emitting materials under development, mainly consisting of quantum dots, organometallic halide perovskites, and various organic materials including small-molecule

[1]Key Lab of Organic Optoelectronics and Molecular Engineering of Ministry of Education, Department of Chemistry, Tsinghua University, Beijing 100084, P. R. China

[2]Center for Flexible Electronics Technology, Tsinghua University, Beijing 100084, P. R. China

*Correspondence: qjuan@mail.tsinghua.edu.cn

organic dyes, low energy-gap polymers, and organometallic complexes. Significant efforts have been made to realize highly efficient NIR-emitting devices. Vasilopoulou et al. employed silica-encapsulated silver sulfide ($Ag_2S@SiO_2$) colloidal quantum dots (QDs) dispersed in a cesium-containing triple cation perovskite matrix as NIR emitter and achieved NIR-QDLEDs with maximum external quantum efficiencies (EQEs) up to 16.98% at 1,397 nm (Vasilopoulou et al., 2020). Gao et al. minimized non-radiative recombination losses by weakening the hydrogen bonding between the passivating functional moieties and the organic cation featuring in the perovskite and achieved perovskite LEDs (PeLEDs) with a maximum EQE of 21.6% at 800 nm (Xu et al., 2019). Li et al. developed spin-allowed doublet radical organic emitters and demonstrated an NIR-organic light-emitting diode (OLED) with a maximum EQE of 27% at 710 nm (Ai et al., 2018). Chi et al. revealed an ordered solid-state packing arrangement of Platinum (II) complexes in the vacuum-evaporated thin films and realized NIR-OLEDs with a maximum EQE of 24% at 740 nm (Tuong Ly et al., 2017) and 2.14% at 930 nm (Wei et al., 2020).

Despite the respective record-high efficiencies, these NIR-emitting materials still have much room for improvement on the way to practical applications. Most of NIR-QDLEDs suffer from severe efficiency roll-offs at high current density (Pradhan et al., 2019; Vasilopoulou et al., 2020). Organometallic halide perovskites have multiple intrinsic stability issues, so that the NIR-PeLEDs still demonstrate poor lifetimes (Cao et al., 2018; Xu et al., 2019). Both of them usually contain toxic elements, such as lead (Pb), which would limit their applications in specific areas. NIR-OLEDs based on the doublet radical emitters also suffer from serious efficiency roll-offs and short lifetimes (Ai et al., 2018). Pt(II) complexes with edge-on preferred orientation demand neat film as the emitting layer with a platinum mass content above 30 wt%, which would lead to high material cost (Tuong Ly et al., 2017).

In comparison, iridium (III) complexes have demonstrated relatively comprehensive properties for practical applications, which have been tested and proved in visible OLED display area, being the preferential choices of green and red emitters in current commercial active-matrix OLED products. In the NIR region, Ir(III) complexes have demonstrated some superior qualities (Xiang et al., 2013; Zampetti et al., 2019; Zhang et al., 2018b): (1) octahedral configuration separates excitons effectively in space and reduces exciton annihilation and efficiency roll-offs significantly; (2) high thermal and electrochemical stability benefit more sustainable and stable devices; (3) low cytotoxicity and high biocompatibility make them good candidates for biological applications; (4) greatly reduced material cost benefits from ∼10 wt% doped emission layer with Iridium mass content as low as 1 wt% in comparison with the neat film of Pt(II) complexes; (5) the production process of devices are well compatible with their commercialized counterparts in visible region.

Although being the preferred choices in visible OLED displays and inheriting so many advantages, Ir(III) complexes still underperformed in the NIR region. To date, the overall performances of these Ir(III) complexes are inferior to those of their neighbor rival Pt(II) complexes in the NIR region. In particular in recent years, Chi and Chou et al. have made a significant progress in NIR-emitting Pt(II) complexes. They reported a series of Pt(II) complexes with bidentate ligands and realized ordered solid-state packing arrangement with an edge-on preferred orientation in the vacuum-evaporated thin films (Tuong Ly et al., 2017; Wang et al., 2020; Wei et al., 2020). With the intermolecular Pt-Pt interactions, the emissive excited states have dominant metal-to-ligand charge transfer (MLCT) character, which are in contrary to traditional Pt(II)-porphyrin complexes with ligand-centered (LC) character states and lead to efficient spin-orbital coupling (SOC) and high radiative decay rate. Most recently, Chou and Chi et al. revealed that the exciton-vibration decoupling strategy through exciton delocalization in Pt(II) complex aggregates can significantly reduce the effective reorganization energy and enable NIR-OLEDs with 930 nm peak wavelength, a high EQE up to 2.14% (Wei et al., 2020). The energy gap law is bypassed to a certain extent, which is no doubt a result of deep understanding of the basic theory. In comparison, the development of NIR Ir(III) complexes is largely based on the trial and error approach. There is plenty of room at the bottom, Richard P. Feynman once said, and it is true for NIR Ir(III) complexes.

Recently, there have been several inspiring reviews summarizing the recent developments and applications on various NIR-emitting materials (Kim et al., 2018b; Zampetti et al., 2019; Zhang et al., 2018b) or various transition-metal complexes (Ho et al., 2020; Zhen et al., 2021). Rather than being exhaustive, this review focuses on NIR-emitting iridium complexes by highlighting their fundamental electronic structures and design strategies. Herein, we first revisit the theoretical backgrounds of phosphorescent Ir(III) complexes and explore their full potential for NIR emission in terms of coordination structures and excitation

Homoleptic Ir(III) complexes

fac-Ir(ppy)$_3$ *mer*-Ir(ppy)$_3$

Heteroleptic Ir(III) complexes

Ir(ppy)$_2$(acac)   [Ir(ppy)$_2$(bpy)]$^+$ [Ir(ppy)$_2$(CN)$_2$]$^-$
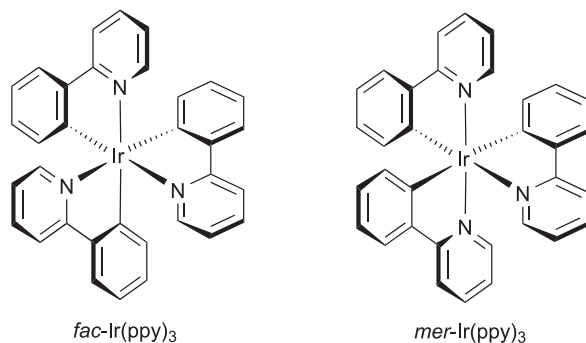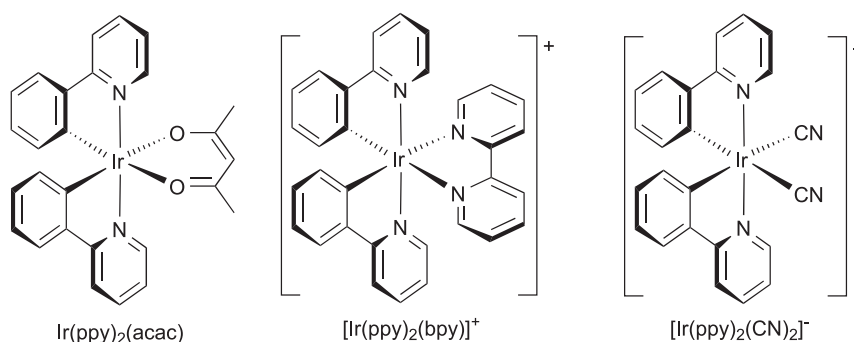
Figure 1. Molecular structures of representative Ir(III) complexes containing 2-phenylpyridine (ppy) as cyclometalated ligands

processes in section basic knowledge and theoretical background. Keeping all this in mind, we systematically summarize the design strategies and photophysical properties of reported NIR-emitting iridium complexes in the light of various modifications in the cyclometalated ligands, ancillary ligands, and coordination geometry, with an aim to provide a fundamental understanding on the structure-property relationship in section molecular designs for NIR-emitting Ir(III) complexes. Several implications for molecular design and modification are proposed. In addition, two promising applications including NIR-OLEDs and biological imaging based on NIR Ir(III) complexes are presented in sections applications in NIR-OLEDs and Applications in biological imaging, respectively. In the end, a perspective and outlook in research and development of NIR Ir(III) complexes and applications are offered from a personal perspective in section perspective and outlook.

BASIC KNOWLEDGE AND THEORETICAL BACKGROUND
Basic structure of phosphorescent Ir(III) complexes

Generally, a typical phosphorescent Ir(III) complex consists of one Iridium atom as core and three bidentate ligands (Figure 1). The atoms of the ligands bonded to the Iridium core are either C (carbon) or N (nitrogen), where C has a formal negative charge to balance positive charges of Ir. The coordination around the Iridium core forms a five- or six-membered metallacycle. These C^N ligands are called after cyclometalated ligands. The other ligands with different structure are named ancillary ligands. For example, in Ir(ppy)$_2$acac, 2-phenylpyridine (ppy) and acetylacetonate (acac) are the cyclometalated ligand and ancillary ligand, respectively. In addition to the neutral complexes, some complexes are ionic, for example, in [Ir(ppy)$_2$bpy]$^+$, the electroneutral bipyridine (bpy) is the ancillary ligand, thus the complex is monocationic and need a counterion (e.g., Cl$^-$, PF$_6^-$) to balance charge; another example is anionic [Ir(ppy)$_2$(CN)$_2$]$^-$ with positive counterions, such as sodium and substituted ammonium (Di Censo et al., 2008; Dumur et al., 2013). The cyclometalated ligands usually have one neutral (N) coordinating part and one anionic (C) part. The Ir-C and Ir-N bonds between the iridium core and these C^N ligands are strong enough compared with covalent bonds, which lead to high thermal stability and favor efficient
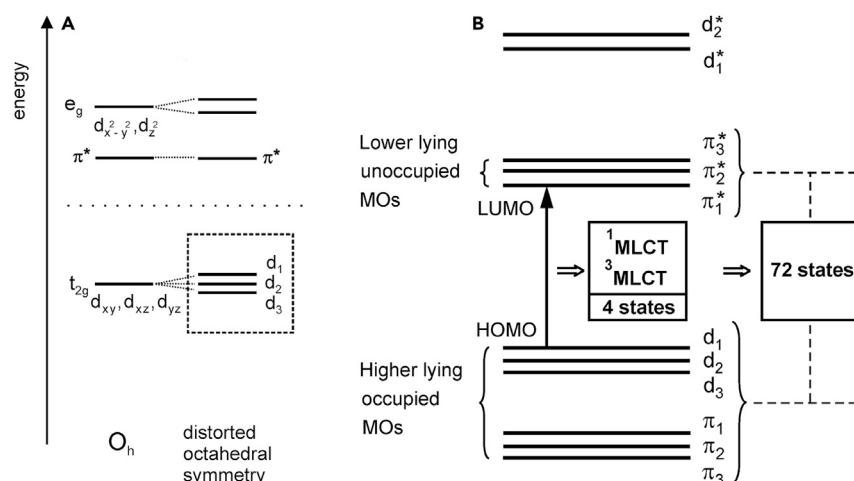
Figure 2. Schematic diagram of the selected orbitals and energy states

(A) Schematic splitting of the d-orbitals in an octahedral and a distorted octahedral compound. The π^*-orbital represents the LUMO. Other unoccupied π^*-orbitals and occupied π-orbitals are neglected for clarity.

(B) Schematic diagram of selected MOs for a (pseudo)octahedral complex with low lying LC and MLCT transitions.

(Yersin et al., 2011). Copyright 2011 Elsevier B.V.

SOC between the Iridium core and ligands, and thus facilitate strong phosphorescence at room temperature.

In most cases, the synthesis of an Ir(III) complex consists of a two-step process. The first step is the reaction forming a chloride-bridged dinuclear Ir(III) dimer (Lamansky et al., 2001b). The Ir(III) dimer contains four cyclometalated ligands and two chloride ions. The second step is substitution of the third ligand for the chlorides yielding the final complex. The third ligand can be either a cyclometalated ligand or an ancillary ligand. If it is the same with the existing cyclometalated ligands in the dimer, the resulting complex is called homoleptic, and if not, heteroleptic. Meanwhile, since the Ir(III) complex has an octahedral coordination conformation, the homoleptic complex may have geometric isomers, which are designated as either the facial (*fac-*) or meridional (*mer-*) form (Figure 1). The facial form with a C_3 axis has a higher symmetry than the meridional form, which leads to different photophysical properties (Tamayo et al., 2003). In the case of heteroleptic complexes, the two nitrogen atoms of cyclometalated ligands are usually in the opposite position, as said in N-N *trans* configuration.

HOMOs-LUMOs excitations and energy states

For metal ions with a d^6 configuration like Ir(III), if in perfect octahedral symmetry (O_h symmetry), the d-orbitals split into sets of three t_{2g} and two e_g orbitals (Figure 2A), where the t_{2g}-shell is fully occupied. Even for facial homoleptic Ir(III) complexes, which are ideally thought to have C_3 symmetry, the Jahn-Teller effect (Jahn and Teller, 1937), saying that a non-linear system in a degenerate energy state cannot be stable, would lead to split in energy of t_{2g} orbitals. Hence, a homoleptic Ir(III) complex will spontaneously distort itself in some way (compressed, elongated, etc.), so that its energy state will split, in such a way as to remove its degeneracy. Such a distortion always has the effect of lowering the energy of the system to a small extent and is thus energetically favorable. However, because the d^6 Ir(III) ion takes a low-spin electron configuration, it is not as Jahn-Teller active in octahedral symmetry as other transition ions, such as Cu(II) ion (Halcrow, 2013) In fact, for most octahedrally coordinated complexes, the symmetry is lower than C_3. As a result, the orbitals of the t_{2g} manifold are no longer degenerate and split into the three orbitals d_1, d_2, and d_3, but they will still be rather proximate in energy (Yersin et al., 2011). As shown in Figure 2B, for a simplified model of a quasi-octahedral homoleptic Ir(III) complex, such as Ir(ppy)$_3$, under assumption of lower symmetry than C_3, it obtains three π and three π^* molecular orbitals from the three cyclometalated ligands. And the t_{2g} set of Ir(III) split into three d-orbitals. Each occupied orbital contains two electrons with opposite spins. An excitation from an occupied orbital to an unoccupied orbital generates four energy states, one singlet state and three triplet substates, with different magnetic spin quantum numbers ΔM_S (1, 0 or −1 in single excitations). Excitations involving all orbitals mentioned above give 72 energy states. These states can be either

MLCT states or LC states. A further consideration taking configuration interaction (CI) and SOC into account will lead to significant energy shifts and modifications of the electronic states. Thus, the 72 states of this model would not be sufficient to approach the experimental situation. Only an inclusion of about 200 states, meaning 32 additional excitations between molecular orbitals (MOs), might result in a somewhat more realistic description for a rather simple molecule like Ir(ppy)$_3$ (Yersin et al., 2011). Moreover, according to quantum chemical calculations, the emissive triplet excited states are usually mixtures of MLCT, intra-ligand charge transfer (ILCT), ligand-to-ligand charge transfer (LLCT), etc., which are rather complex for a qualitative analysis.

Photoluminescence quantum yield (PLQY) of organic molecules can be expressed as Equation 1:

$$PLQY = \frac{k_r}{k_r + k_{nr}} = \tau k_r$$
(Equation 1)

where k_r and k_{nr} are the radiative and nonradiative decay rate constants and τ is the emission decay time. PLQY reflects the luminous efficiency of organic molecules. In the following, we mainly focus on the intrinsic and extrinsic influencing factors of PLQY for NIR-emitting Ir(III) complexes. Some important design strategies for efficient NIR-emitting Ir(III) complexes are revealed.

Spin-orbital coupling and radiative decay rate k_r

Without SOC interaction, the radiative transition of a pure triplet excited substate to the singlet ground state is strictly spin forbidden. Yersin et al. have given solid reviews about how SOC makes radiative transition possible for a triplet substate of organo-transition metal complexes (Yersin et al., 2011). Here we give a relatively simplified introduction for the analysis of NIR-emitting Ir(III) complexes. Ideally, one substate of triplet MLCT state (^{3}MLCT) can undergo SOC with all other substates. However, since the SOC Hamiltonian is a sum of one-particle operators, only substates can be coupled by SOC, which differ in just one spin-orbital and obey the selection rule $\Delta M_S = 0, \pm 1$, according to the Slater-Condon rules for matrix elements of such operators (Yersin et al., 2011). Furthermore, the contribution of many coupling routes is little with respect to a few dominating routes and thus can be neglected (Rausch et al., 2007; Rausch et al., 2010). For example, SOC between an ^{3}MLCT substate and the singlet/triplet $\pi\pi^*$-states (^{1,3}LC states) is weak, since the d- and the π- or π^*-orbitals are located at different atomic centers. According to quantum mechanics, the resulting matrix elements can be described as two- or three-center integrals, which are vanishingly small and thus can be neglected due to the exponential decay of each orbital with increasing distance from its center (Rausch et al., 2010). Besides, SOC between an ^{3}MLCT substate and a singlet MLCT state (^{1}MLCT) from the same d-orbital can also be neglected since the SOC operator cannot couple the same d-orbital (Rausch et al., 2010). In comparison, strong direct SOC can occur between an ^{3}MLCT substate and the singlet/triplet MLCT (sub)states involving the different d-orbital. In these cases, two different metal d-orbitals are coupled by the SOC operator at the central metal ion; thus, only one-center integrals at the metal center with a large SOC constant result (Yersin et al., 2011).

The impact of effective SOC paths on the photophysical properties of the substate can be illustrated by using perturbation theory. Many states can contribute to the emitting triplet substates via direct SOC, when the selection rules for SOC are fulfilled: the resulting matrix elements correspond to one-center integrals at the central metal ion and no symmetry restrictions are effective (Yersin et al., 2011). For a substate i of T$_1$ state with MLCT character, in a relatively realistic treatment of SOC, the k_r can be expressed by Equation 2, as given below (Rausch et al., 2010; Obara et al., 2006; Yersin et al., 2011).

$$k_r(i) = \frac{64\pi^4 \bar{\nu}^3}{3hc^3} \cdot \left| \sum_m \frac{\langle S_m | H_{SO} | T_1(i) \rangle}{E[T_1] - E[S_m]} \cdot \langle S_0 | er | S_m \rangle \right|$$
(Equaiton 2)

S_m is an ^{1}MLCT state that originates from different d-orbital with T$_1$. $E[T_1]$ and $E[S_m]$ are the energies of the corresponding unperturbed states. The "$E[T_1] - E[S_m]$" term is called the energy denominator of SOC matrix elements. H_{SO} is the SOC operator. $\bar{\nu}$ and er represent the electronic transition energy in cm^{-1} and the electric dipole operator, respectively. The matrix element $S_0|er|S_m$ represents the transition dipole moment between the electronic singlet ground state S$_0$ and the S$_m$.

The emissive triplet state of a realistic NIR-emitting Ir(III) complex has both MLCT and LC character. For a substate of the ^{3}LC state, the direct SOC between this ^{3}LC substate and higher lying states is negligible. Instead, the indirect SOC came up based on a two-step mechanism consisting of CI of the ^{3}LC substates

with ^{3}MLCT substates and subsequent direct SOC of the latter ones with ^{1}MLCT states (Kimachi et al., 1997; Miki et al., 1993; Obara et al., 2006). CI is based on electron-electron interaction. CI-induced mixing can only occur between states of equal spin multiplicity. Thus, the CI selection rules are ΔS = 0 and ΔM$_S$ = 0. There is also an important energy denominator for CI, i.e., the energy difference between the ^{3}LC state and ^{3}MLCT state involving in CI, "$E[^3LC] - E[^3MLCT]$" (Azumi and Miki, 1997; Rausch et al., 2010; Yersin et al., 2011). However, even without giving explicit equations, it should become clear that, owing to the involvement of different matrix elements, i.e., for CI and for SOC, and different energy denominators, this indirect SOC path to the substates of an ^{3}LC state has less influence on k_r than direct SOC to the substates of an ^{3}MLCT (Yersin et al., 2011).

As the emission of Ir(III) complexes into the NIR region, the electronic transition energy $\overline{\nu}$ inevitably gets smaller, thus we should work on the other parameters except $\overline{\nu}$ to boost k_r. Based on the theory and equation above, some valuable implications toward high k_r for efficient NIR-emitting Ir(III) complexes could be revealed as follows:

(1) **Increase the proportion of the MLCT component in the emissive triplet state.** The MLCT component can undergo direct SOC and has more influence on k_r than the LC component. With the help of quantum chemical calculation, the contributions of different transitions to the triplet state could be estimated and used to calculate the MLCT percentages of the emissive triplet state, which is beneficial for molecular design.

Although there is no clear solution to practically enhance the MLCT component for iridium complexes yet, there are some inspiring works on increasing the proportion of excited state components that can undergo direct SOC. For example, Shafikov et al. reported a dinuclear Ir(III) complex Ir$_2$I$_2$, which contains two Ir(III)-iodide moieties (Shafikov et al., 2021). According to their TD-DFT calculations, the T$_1$ state of Ir$_2$I$_2$ originates from the highest occupied molecular orbital (HOMO)→lowest unoccupied molecular orbital (LUMO) electronic transition (98%). The HOMO of Ir$_2$I$_2$ has 16% contribution from iridium and 74% contribution from iodide, thus a total contribution of 90% from MX (M stands for metal, X stands for halide). Meanwhile, the LUMO of Ir$_2$I$_2$ has only 4% contribution from iridium and negligible contribution from iodide. With the SOC coefficient of iodide being 5,069 cm^{-1}, even higher than that of iridium (3,909 cm^{-1}), the iodide atoms can facilitate the halide-(X)-to-ligand charge-transfer (XLCT) and undergo direct SOC. As a result, the dominant MXLCT character, along with their dinuclear strategy, leads to a very large radiative rate of 2.65 × 10^6 S^{-1}, which is even higher than that of its counterpart Ir$_2$Cl$_2$ (k_r = 2.27 × 10^6 s^{-1}), which contains two Ir(III)-Chloride moieties.

(2) **Decrease the energy separation of ^{3}MLCT and ^{1}MLCT and increase the pairs of ^{3}MLCT and ^{1}MLCT with close energy.** One has to note that the two states involving in "direct SOC" originate from different d-orbitals, and the energies of ^{3}MLCT and ^{1}MLCT are unperturbed. The energy separation of ^{3}MLCT and ^{1}MLCT corresponds to the energy denominator in Equation 2. When the energy denominators get smaller and the state pairs with close energy get more, k_r will become larger.

Let us simplify the energy states to illustrate this point qualitatively. Suppose there is a perfect octahedral Ir(III) complex with six identical coordination points, the t$_{2g}$ set of iridium d-orbitals do not split, which is an ideal model of that shown in Figure 2A. Since the ligands are the same, the ^{3}MLCTs and ^{1}MLCTs are degenerate in energy, respectively. In this ideal case, the energy denominators are minimized and state pairs with close energy are maximized. However, for most Ir(III) complexes, the six coordination points are usually donated by three asymmetric ligands. The symmetry is reduced, and the numbers of states with degenerate energy decrease. When the complex is heteroleptic with symmetric non-chromophore ancillary ligand, it has quansi-C$_2$ symmetry with two identical ligands and the t$_{2g}$ set splits. When the complex is *mer*-homoleptic or heteroleptic with asymmetric ancillary ligand, it has C$_1$ symmetry and the t$_{2g}$ further splits. Accordingly, the configurations of *fac*-homoleptic and heteroleptic with symmetric ancillary ligand are relatively recommended and are just right now the main streams in NIR Ir(III) complexes. In addition, the ligand structures are better to be rigid to keep symmetry and avoid distortions in excited states (Baek et al., 2020; Sajoto et al., 2009; Zhou et al., 2016).

(3) **Increase the oscillator strength between ^{1}MLCT and S$_0$.** The matrix element S$_0$|er|S$_m$ represents the transition dipole moment between the electronic singlet ground state S$_0$ and the excited state S$_m$. Thus, k_r depends on the allowedness of this singlet-singlet transition, i.e., its oscillator strength.

(4) **Reduce the energy separation between ^{3}MLCT and ^{3}LC to increase the efficiency of indirect SOC.** In the reported literatures, the calculated ^{3}MLCT contributions of T_1 states of NIR Ir(III) complexes are usually lower than 40% (Zhang et al., 2020; Xue et al., 2017). That means more than half of the contributions come from ^{3}LC. Since ^{3}LC needs CI with ^{3}MLCT to further undergo SOC with ^{1}MLCT, the efficiency of CI needs to be improved. One effective way to improve the efficiency of CI is reported for NIR-emitting Ir(III) complexes by Teets et al. (Lai et al., 2020). They use electron-donating ancillary ligand to destabilize the iridium-centered HOMO and lower the MLCT energy (see section the ancillary ligand). In this way, the energy separation between ^{3}MLCT and ^{3}LC is reduced and the corresponding energy denominator of CI is reduced as well. This approach increases the overall MLCT character of the emissive triplet excited state and contributes large k_r (Lai et al., 2018).

Vibrational coupling and nonradiative decay rate k_{nr}

Intramolecular emission quenching is an intrinsic property of a molecule in an inert matrix (Yersin et al., 2011). One quenching mechanism is via the thermal population of metal-centered states of dd* character (^{3}MC), so-called ligand-field (LF) states (Sajoto et al., 2009). This is a major issue for blue-emitting Ir(III) complexes but not for NIR-emitting Ir(III) complexes. Since these Ir(III) complexes have relatively similar C^N ligands that produce roughly similar ligand field, their metal-centered dd* state energies would be relatively close. But the NIR emission is much lower in energy than the blue emission, which makes it rather difficult for the NIR excited state to be quenched by ^{3}MC states. Another thing that needs to be noticed is that the excited state geometry may have distortions with respect to that of ground state (Zhou et al., 2016). The Ir-ligand bonds may be slightly elongated or even broken, assisted by a structural motion of the ligands. This structural distortion may reduce the energy gap between the ^{3}MLCT and ^{3}MC states and thus accelerate the nonradiative decay. An effective way to inhibit the structural distortion is reported by adding steric hindrance on the non-chromophore ancillary ligand (Baek et al., 2020, see section the ancillary ligand in details).

The major issue of NIR-emitting Ir(III) complexes to deal with is the accelerated non-radiative processes as governed by the energy gap law. Non-radiative processes from an excited state to the ground state can be effective via an involvement of vibrational modes of the ground state. This phenomenon is often termed vibrational quenching (Yersin et al., 2011). Such quenching can occur when the involved electronic states are coupled by promoting vibrational modes and the subsequent vibrational relaxation takes place via the so-called accepting vibrational modes of the electronic ground state. More than five decades ago, a theoretical description has been derived already by detailed formalisms based on Fermi's golden rule (Englman and Jortner, 1970; Freed and Jortner, 1970; Robinson and Frosch, 1963; Siebrand, 1967). Accordingly, k_{nr} for vibrational quenching can be expressed as Equations 3 and 4 (Kober et al., 1986; Stufkens and Vlček, 1998; Treadway et al., 1996; Whittle et al., 2001; Yersin et al., 2011):

$$\ln(k_{nr}) = \ln(\beta) - \frac{1}{2}\ln(a \cdot \hbar\omega_m E_0) - S_m - \frac{\gamma E_0}{\hbar\omega_m} + \left(\frac{\gamma+1}{\hbar\omega_m}\right)^2 \left[\frac{\left(\Delta\bar{\nu}_{1/2}\right)^2}{16\ln 2}\right]$$ (Equation 3)

With

$$\gamma = \ln\left(\frac{E_0}{S_m \hbar\omega_m}\right) - 1$$ (Equation 4)

The first term β of Equation 3 represents the nonadiabatic electronic coupling between the involved electronic states, whereas all the other terms result from the vibrational coupling of the initial vibrational mode of the excited state with the vibrational accepting mode m of the ground state being in resonance. a is a constant in units of $(cm^{-1})^{-2}$. $\omega_m = 2\pi\nu_m$ is the angular frequency of the accepting mode m. E_0 is the transition energy from the excited electronic substate to the ground state. S_m is the Huang-Rhys parameter, which describes the displacement of the potential energy surfaces of the involved electronic states along the vibrational normal coordinate of the accepting mode m. Within the above-described framework, the last term treats low-energy intramolecular vibrations and solvent effects, which are classically described with the half-width of the emission bands $\Delta\bar{\nu}_{1/2}$.

Equation 3 can be further simplified when compounds with similar electronic couplings (represented by β) and similar interactions with the solvent (represented by $\Delta\bar{\nu}_{1/2}$) are compared. Thus, a more common form of the energy gap law can be given by Equation 5 (Yersin et al., 2011):

$$k_{nr} \propto \text{const} \cdot \exp\left(-\frac{\gamma E_0}{\hbar \omega_m}\right) \qquad \text{(Equation 5)}$$

The parameter β in Equation 3 is essentially determined by a small number of promoting vibrational modes. The contribution of one specific promoting mode k is determined by an expression of Equation 6 (Yersin et al., 2011):

$$\left|C_{S,T}^k\right|^2 \omega_k \sqrt{\frac{\pi}{2}} \qquad \text{(Equation 6)}$$

where ω_k is the angular frequency of the promoting vibrational mode k. $C_{S,T}^k$ is given by Equation 7 (Yersin et al., 2011) and is basically determined by the vibronic coupling matrix element between the wavefunctions of the T_1 state, or more exactly of a substate, and the electronic ground state S_0.

$$C_{S,T}^k = \frac{\hbar i}{\sqrt{M_k}} \langle \varphi_S \left| \frac{\partial}{\partial Q_k} \right| \varphi_T \rangle \qquad \text{(Equation 7)}$$

where M_k is the reduced mass of the specific mode k. This vibrational mode promotes the coupling between the two states involved. Q_k is the respective normal mode coordinates. φ_S and φ_T are the electronic wavefunctions of the ground state S_0 and a substate of the excited triplet state T_1, respectively. Note that these wavefunctions depend parametrically on the nuclear geometry, i.e., on the normal coordinates Q_k. In this approach, φ_T represents a perturbed wavefunction of one triplet substate. That means the wavefunction is already modified by SOC and contains admixtures from higher lying singlet states. Furthermore, to a very good approximation, the unperturbed wavefunction of the singlet ground state may be applied for φ_S.

As the emission of Ir(III) complexes into the NIR region, the electronic transition energy E_0 inevitably gets smaller; thus, one has to work on the other parameters except E_0 to lower k_{nr}. Based on the theory and equation above, some valuable implications toward low k_{nr} for efficient NIR-emitting Ir(III) complexes could be revealed as follows:

(1) **Reduce the amount of vibrational modes.** There are many vibrational modes that contribute to vibrational quenching. For NIR Ir(III) complexes, their cyclometalated C^N ligand structures and core coordination structures are roughly derived from Ir(ppy)$_3$ or Ir(ppy)$_2$acac. As a result, the frequencies of related vibrational modes for these structures are expected to be roughly similar. But the peripheral structure of the cyclometalated ligands and ancillary ligands can be very different. It would be better to avoid using structures with extra vibrational modes, in other words, better to employ rigid and compact ligand frameworks.

(2) **Reduce the Huang-Rhys parameter.** The Huang-Rhys parameter S_m describes the displacement of the potential energy surfaces of the involved electronic states along the vibrational normal coordinate of the accepting mode. Again, it would be better to employ rigid and compact ligand frameworks to reduce S_m. At low temperatures the parameter can be obtained by dividing the intensity of the (0-1) transition by the (0-0) transition (Lo et al., 2006). But sometimes there may be more than one vibronic mode appearing and the peaks may overlap with each other. In this situation, the Huang-Rhys parameter could be estimated from the relationship $I_{0-0} = I_{total} \times e^{-S_m}$, in which I_{0-0} is the intensity at the electronic origin (0–0 transition) and I_{total} is the total emission intensity (Lai and Teets, 2019). The estimated Huang-Rhys parameters may help with molecular optimization and discussion of photophysical properties for a parallel series of molecules and have been employed in some reports of NIR-emitting Ir(III) complexes (Kim et al., 2018a; Lai et al., 2020; You et al., 2020a).

Extrinsic influencing factors of PLQY

Besides the above-mentioned intrinsic influencing factors, the external environment and interactions between emitters and other molecules would also have influences on the PLQY of the emitters (Yersin et al., 2011). The environment (host matrix cage) of an emitter can alter d- and π-orbital mixing by variations of the cage geometry, which can distinctly alter SOC efficiencies (Yersin et al., 2011). The rigid environment in solid films favors higher PLQYs than those in solutions, which mainly benefit from the suppression of harmful vibrations. In terms of intermolecular quenching of the emission, at least one other molecule of the same or a different species is necessary. If molecules of the same species are involved, luminescence

quenching preferably occurs at higher concentrations via annihilation of excited emitters in close proximity (e.g., triplet-triplet annihilation, TTA [Baldo et al., 2000; Giebink and Forrest, 2008; Reineke et al., 2007a; 2007b]) or via energy transfer according to the Förster and/or the Dexter mechanism from excited to non-excited molecules.

Energy transfer to other molecules can also result in serious exciton quenching, such as molecular oxygen. Ground state molecular oxygen is a natural triplet quencher for triplet excited states. The corresponding mechanism can be either energy transfer from an excited emitter to ground state triplet oxygen ($^3O_2$) with subsequent conversion to the excited singlet oxygen ($^1O_2$) or electron transfer processes (Demas et al., 1977; Djurovich et al., 2007; Schweitzer and Schmidt, 2003). To avoid quenching by O_2, fluid solutions of the triplet emitters have to be carefully and quantitatively deaerated, and films doped with triplet emitters should be handled in an inert atmosphere (Yersin et al., 2011). The tendency to be quenched by oxygen is usually correlated with a long emission decay time of an emitter, so in this respect short radiative emission decay times are favorable. Benefiting from the octahedral coordination structure, Ir(III) complexes feature shorter triplet emission lifetimes compared with square-planar Pt(II) species.

MOLECULAR DESIGNS FOR NIR-EMITTING IR(III) COMPLEXES

In this section, we systematically review the reported NIR-emitting Ir(III) complexes and describe their over-all progress in molecular designs. For these NIR-emitting Ir(III) complexes, their molecular structures are shown in Figure 3 and the detailed photophysical data are summarized in Table 1. Herein, we attempt to summarize the design strategies and photophysical properties of reported NIR-emitting iridium complexes based on various modifications in the cyclometalated ligands, ancillary ligands, and coordination geometry. Our ambition here is to provide a fundamental understanding on the structure-efficiency relationship. Some important trends and guidelines for controlling photophysical properties are revealed.

As stated in introduction, NIR Ir(III) complexes have relatively comprehensive properties for practical applications. But there are two major issues hindering the advance of practical process. One is the relatively low emission efficiency, for which we have recalled the related basic theories in section basic knowledge and theoretical background and proposed some important implications. The other is that the emissions are just not "red" enough. The ideal NIR emission for practical applications should be totally invisible to human eyes. However, for most of the NIR emitters reported so far, not limited to Ir(III) emitters (Figure 4), their emission peak wavelengths are merely over 700 nm and the whole emission bands have significant parts in the visible region. Considering that the wavelength of the reddest light perceivable by human eyes is greater than 700 nm (even up to 780 nm), and the broadening of the emission band, a peak emission wavelength of 800 nm (even up to 850 nm) may be proper for the completely invisible applications. As shown in Table 1, one can notice that, for the emission into the real invisible NIR region, the related reports are few and the PLQYs are low. This is just the big issue in this section we attempt to explore how to make one emitter redder and efficient at the same time.

The cyclometalated ligands—the C^N ligands

For the majority of homoleptic Ir(C^N)$_3$ type or heteroleptic Ir(C^N)$_2$(L^X) type complexes, the cyclometalated C^N ligands are dominant for their photophysical properties because the C^N ligands not only anchor the emission energies of the final complexes but also largely determine the SOC strengths and structure rigidities. To make the emission step into the NIR region, the structure of the C^N ligands would inevitably be more complex than their counterparts in the visible region. Thus the design and synthesis of C^N ligands would be the major part of the development workflow of NIR Ir(III) complexes. What is more is that the coordination ability of C^N ligands largely decide the final coordination configuration of the resulting complexes, for which it would be facial homoleptic or heteroleptic. Accordingly, for the molecular design of an NIR Ir(III) emitter, constructing an appropriate C^N ligand is in first priority.

Generally, in a wide range, all these C^N ligands can be seen as derivatives from ppy by employing different derivation methods or the combination of several derivation methods. There are three widely used derivation methods: (1) extending the conjugation of the aromatic rings; (2) replacing carbon atoms/rings with hetero atoms/rings; (3) decorating the ligand core with peripheral substituents connected with a single bond. These methods either individually or jointly adjust the distribution of the frontier molecular orbitals (FMOs) and composition of emissive triplet states, thus leading to various complexes with different photophysical properties.
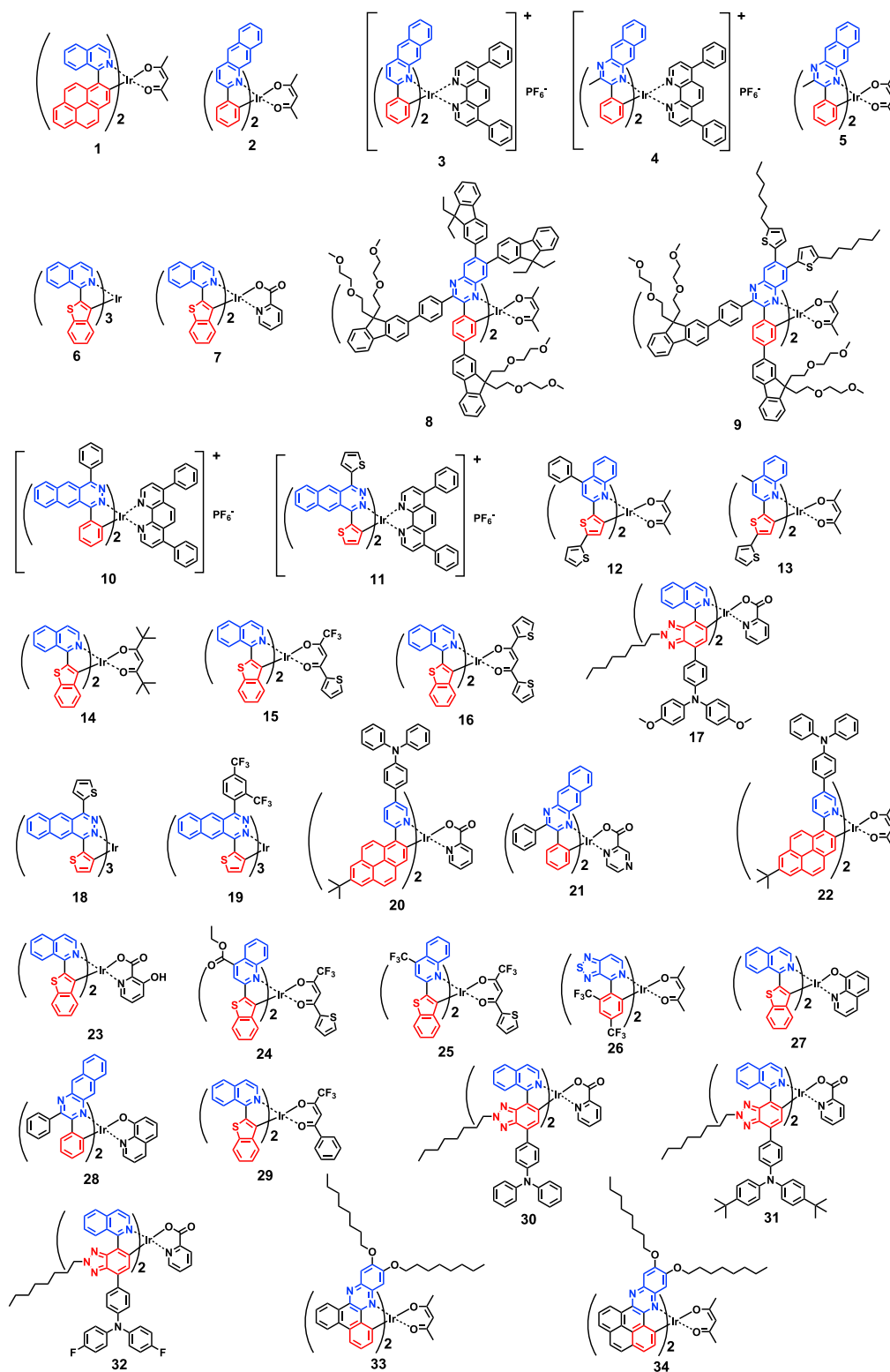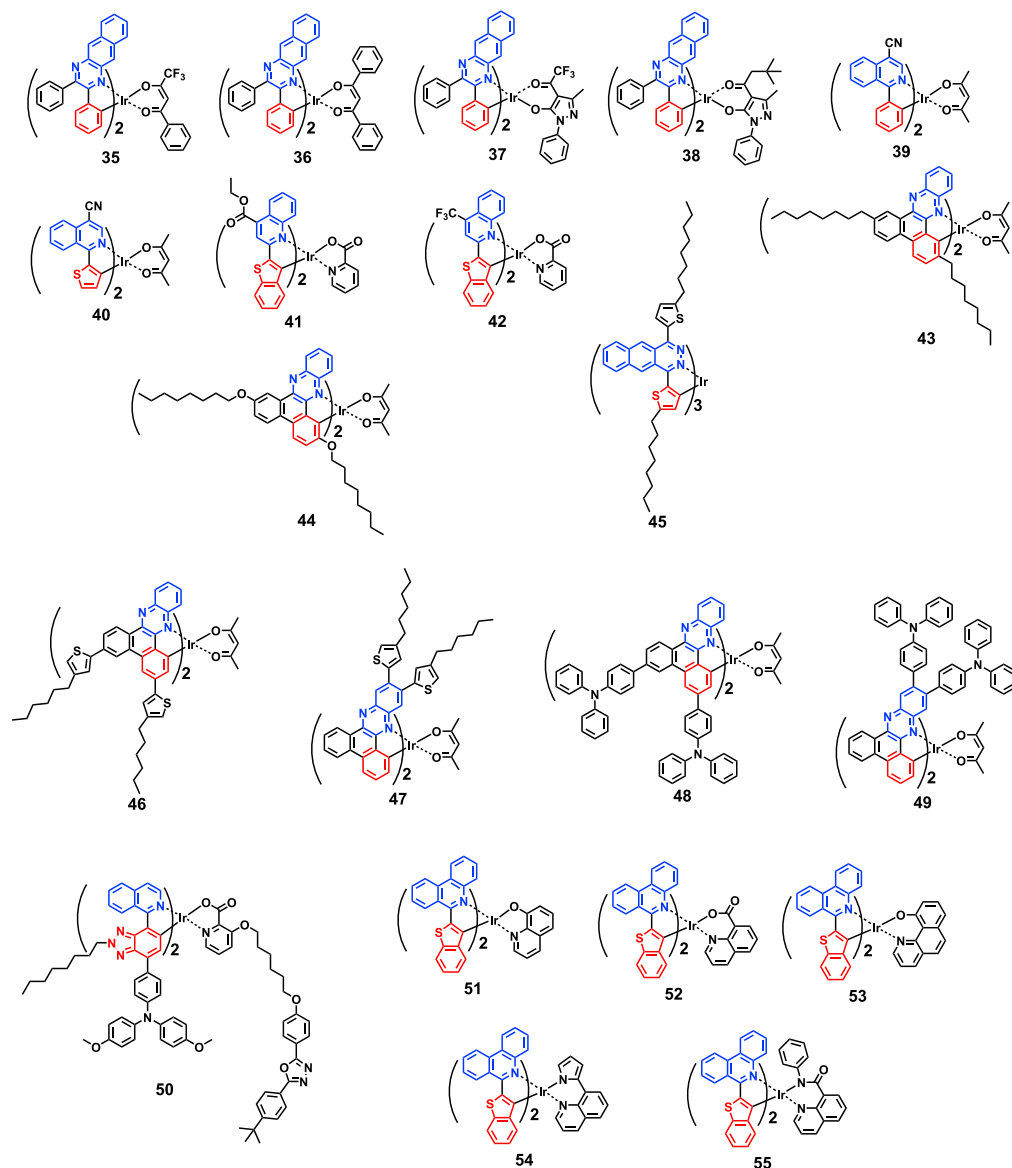
Figure 3. Chemical structures of NIR-emitting Ir(III) complexes.

With regard to all the modifications, the ligands can still be divided into three parts for the clarity of analysis: (1) the neutral coordination part—the N part, for which the coordination atom is usually nitrogen, marked with blue in Figure 3; (2) the anionic coordination part—the C part, for which the coordination atom is usually carbon, marked with red in Figure 3; (3) the peripheral substitution part—all the rest of the ligands, marked with black in Figure 3. The main difference among the three parts is their different contribution to the FMOs and resulting emissive triplet states. The quantum chemical calculations can help to provide insight on the structure-property relationship.

For the majority of NIR Ir(III) complexes covered here, which are either facial homoleptic or heteroleptic with non-chromophore ancillary ligands, their FMOs, i.e., the HOMOs and the LUMOs have similar regularity of distributions. In most cases, the HOMOs dominantly localize on the iridium core and the C part, with minor contributions from the N part and peripheral substitutions. The LUMOs dominantly localize on the N part, with minor contributions from the C part, the iridium core, and peripheral substitutions.

Table 1. Photophysical data of NIR-emitting Ir(III) complexes

No.	λ_{PL} (nm)[a]	τ_{obs} (µs)[b]	PLQY (%)[c]	k_r (× 10^5 s^{-1})	k_{nr} (× 10^5 s^{-1})	Reference
1						(Williams et al., 2006)
2	708,780(s)	0.57	2.5			(Qiao et al., 2009)
3	694,752(s)	1.86	3			(Tao et al., 2012)
4	755	0.35	0.2			(Tao et al., 2012)
5	777,850(s)	0.28[0.44]	1.5[3.6]	0.54[0.82]		(Tao et al., 2013)
6	690[694]	1.77	15[11]			(Ikawa et al., 2013)
7	698		12			(Li et al., 2014)
8	695	0.87	18.6[23.2]			(Cao et al., 2015)
9	713	0.68	14.9[11.9]			(Cao et al., 2015)
10	715,788[708,778]	0.79	3.1[6.1]			(Xin et al., 2015)
11	775[760]	0.33	2.9[4.1]			(Xin et al., 2015)
12	707	4.6	0.34			(Szafraniec-Gorol et al., 2015)
13	703	5.1	0.09			(Szafraniec-Gorol et al., 2015)
14	710	1.40	16	1.1	6.0	(Kesarkar et al., 2016)
15	704	0.72	7	0.97	13.0	(Kesarkar et al., 2016)
16	707	1.44	14	0.97	6.0	(Kesarkar et al., 2016)
17	718,790(s)		0.3			(Yu et al., 2016)
18	824	0.20	2.9[5.2]	1.5	48.6	(Xue et al., 2017)
19	765,820(s)	0.73	14.7[17.3]	2.0	11.7	(Xue et al., 2017)
20	698,792(s)	1.04	2.25	0.24	9.4	(Hao et al., 2018)
21	763[755,833(s)]		14			(Kim et al., 2018c)
22	697,792(s)	0.66	1.92	0.29	14.91	(Liu et al., 2018b)
23	700,760(s)	2.13	13	0.61	4.08	(Fu et al., 2018)
24	758[735]	0.05[0.22]	1.1[3.8]	0.22[0.17]	19.78[4.37]	(Kim et al., 2018a)
25	722[722]	0.94[1.12]	10.6[13.0]	0.11[0.12]	0.95[0.77]	(Kim et al., 2018a)
26	729	5.0				(Chen et al., 2018)
27	687,756(s)	0.73	16	2.19	1.15	(Guo et al., 2019)
28	786	0.47	5	1.06	2.02	(Guo et al., 2019)
29	698,768(s)	0.78	8	1.03	11.8	(Zhou et al., 2019a)
30	715,791(s)[716,791(s)]		0.2			(Yu et al., 2019)
31	716,792(s)[721,794(s)]		0.5			(Yu et al., 2019)
32	712,788(s)[715,791(s)]		0.3			(Yu et al., 2019)
33	685	0.41	27	6.58	17.8	(You et al., 2019)
34	732	0.60	13	2.17	14.5	(You et al., 2019)
35	774	0.35	1.3	0.37	28	(He et al., 2020b)
36	776	0.29	1.8	0.62	34	(He et al., 2020b)
37	772	0.32	1.9	0.59	31	(He et al., 2020b)
38	780	0.28	2.5	0.89	35	(He et al., 2020b)
39	696[699]	0.14[0.30]	16[45]	[15.0]	[18.3]	(Chen et al., 2020)
40	708[708]	0.15[0.83]	6[44]	[5.3]	[6.8]	(Chen et al., 2020)
41	749[729]	0.079[0.28]	1[3]	0.20[0.13]	14.09[3.57]	(Kim et al., 2020a)
42	716[715]	1.39[1.41]	12[14]	0.08[0.10]	0.63[1.26]	(Kim et al., 2020a)
43	732[721]	0.98	28	2.86	7.35	(You et al., 2020b)
44	775[774]	0.54	8	1.48	17.0	(You et al., 2020b)
45	839[854,942(s)]	0.16	1.5[1.9]	0.94	61.6	(Zhang et al., 2020)

(Continued on next page)

Table 1. *Continued*

No.	λ_{PL} (nm)[a]	τ_{obs} (μs)[b]	PLQY (%)[c]	k_r ($\times 10^5$ s^{-1})	k_{nr} ($\times 10^5$ s^{-1})	Reference
46	712[710(s),790]	0.90	18[33]	2.0	91	(You et al., 2020a)
47	741[742]	0.32	20[26]	6.3	25	(You et al., 2020a)
48	716[710(s),787]	0.77	25[32]	3.2	10	(You et al., 2020a)
49	728[727]	0.39	30[31]	7.7	18	(You et al., 2020a)
50	718,790(s)[721,791(s)]		0.47			(Yu et al., 2020)
51	711	2.0	36	1.8	3.2	(Lai et al., 2020)
52	724	1.7	30	1.8	4.1	(Lai et al., 2020)
53	723	1.5	28	1.9	4.8	(Lai et al., 2020)
54	729	1.0	4.2	0.42	9.6	(Lai et al., 2020)
55	716	1.6	34	2.1	4.1	(Lai et al., 2020)

[a]Peak emission wavelengths of photoluminescence in dilute solutions (thin solid films), the "s" in the parentheses means shoulder peak.
[b]Observed emission lifetime of photoluminescence in dilute solutions (thin solid films).
[c]Photoluminescence quantum yield in dilute solutions (thin solid films).

As discussed in section basic structure of phosphorescent Ir(III) complexes, a simple HOMO-LUMO excitation may not reflect the exact lowest triplet excited state for an Ir(III) complex with MLCT character. Hereby, a reasonable approximation of the HOMOs-LUMOs excitation helps to understand how the C^N ligands dominate the lowest triplet states. According to the contribution of C^N ligands to the FMOs, some valuable design strategies have been employed in the development of NIR Ir(III) emitters. In the following part, we took the ppy as the parent ligand to illustrate the evolution of structural derivation and molecular modifications.

The N part

Extending conjugation and/or replacing carbon atoms/rings with electron-deficient hetero-atoms/rings are usually used for the modification of the N part. Figure 4 shows representative N part modifications starting from ppy toward NIR emission. The main effect is lowering the energy of LUMOs and, as a result, lowering the energy of the emissive triplet state and leading to "redder" emission.

For the N part modification, there were already famous and successful examples in the development of red-emitting Ir(III) complexes. As shown in Figure 4, the conjugation for pyridine could be extended condensing benzene rings in different positions, which derived the 2-phenylquinoline (pq) and 1-phenylisoquinoline (piq). The emission of the corresponding complexes moved from green Ir(ppy)$_3$ at 514 nm (Baldo et al., 1999) to orange Ir(pq)$_2$acac at 597 nm (Lamansky et al., 2001a) and red Ir(piq)$_3$ at 620 nm (Tsuboyama et al., 2003). With the same strategy adopted in the NIR region, one more aromatic ring was condensed at the same direction of the benzene ring of the quinoline reported by our group. The emission peak of complex 2 stepped into the NIR region (708 nm) (Qiao et al., 2009). However, the aromatic ring condensation strategy is limited by commercially available reagents and available reactions. Instead, we introduced one more nitrogen atom into the pyridine ring, and the N part became benzo[g]quinoxaline. A further redshift was achieved by complex 5 (777 nm) (Tao et al., 2013).

In terms of the derivation of piq, the same strategy with one more nitrogen atom was first employed by Wang et al. (Ir(MPCPPZ)$_3$ in Figure 4) (Tong et al., 2008) and Huang et al. (Ir(BPPa)$_3$ in Figure 4) (Mi et al., 2009). The N part became phthalazine. Next, the aromatic ring condensation strategy was employed by our group to obtain a further redshift in complexes 18, 19, and 45 (Xue et al., 2017; Zhang et al., 2020). One important feature of the phthalazine N part is that the extra sp^2-hybrid N is adjacent to the chelating N atom, thus leading to decreased steric hindrance. These ligands enable simple one-pot synthesis of homoleptic Ir(III) complexes without any catalyst under mild conditions (1 equivalent IrCl$_3 \cdot$nH$_2$O, 3.6 equivalent C^N ligand, 2-Methoxyethanol:H$_2$O = 3:1(V:V) as solvent, heating temperature around 100°C) (Tong et al., 2008; Xue et al., 2017; Zhang et al., 2020).

The aromatic rings condensed on the pyridine ring were not limited to benzene rings. Wong and Chen et al. reported complex 26 (Figure 4) with a thiadiazole ring condensed on the pyridine ring (Chen et al., 2018).
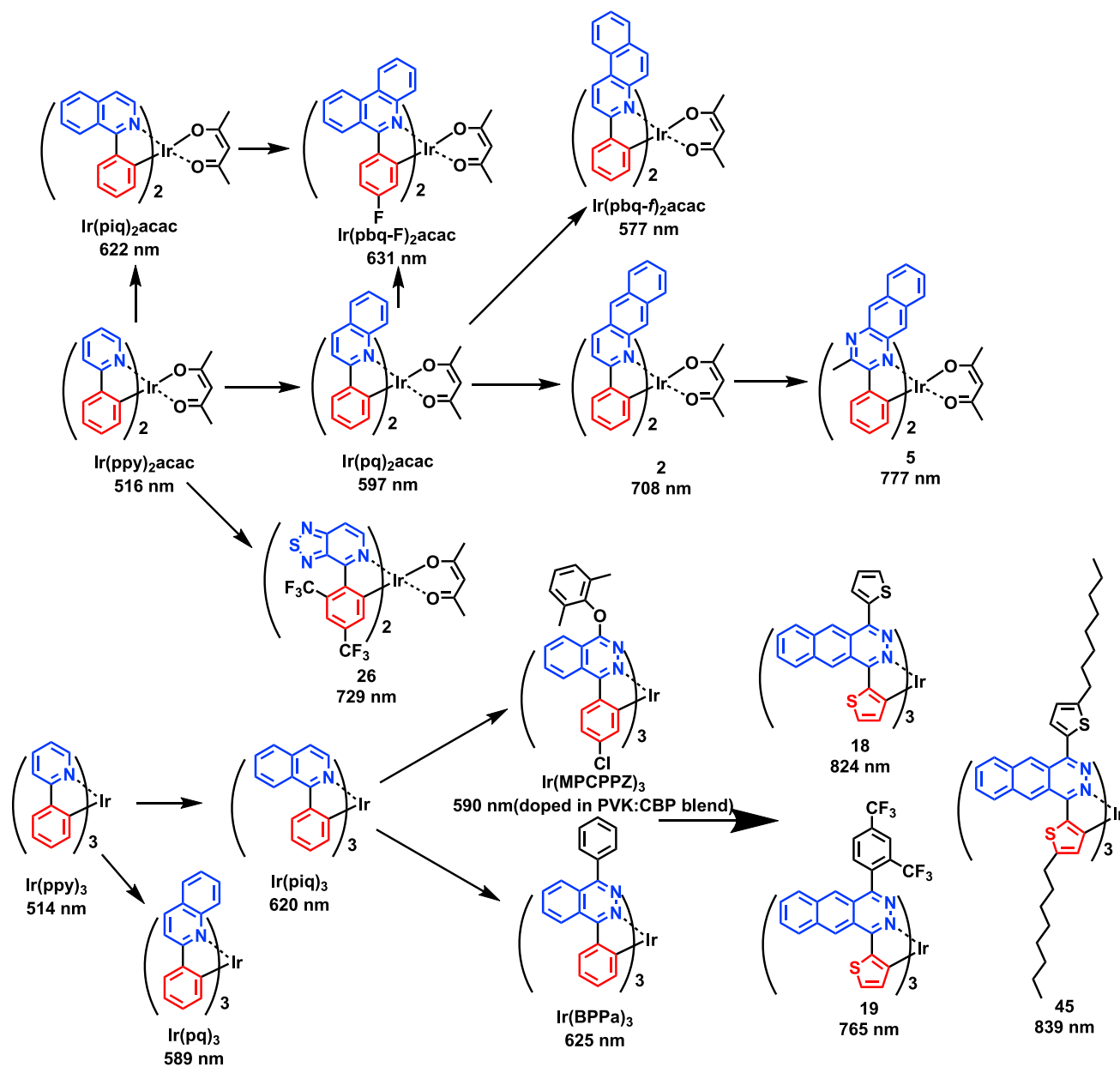
Figure 4. Representative Ir(III) complexes with N part modifications starting from ppy toward NIR emission
Their PL emission wavelengths in dilute solutions are also provided.

The thiadiazole ring is an interesting structure, as it has both electron-rich and electron-deficient features. The ring is a five-membered ring six-electron system; the sulfur atom provides two electrons for the π system. Meanwhile, the two sp²-hybrid nitrogen atoms are electron deficient than normal sp²-hybrid carbon atoms. Overall, this ring presented an electron-deficient feature and achieved a large redshift to 729 nm.

Moreover, the aromatic rings condensed on the pyridine ring could be in different positions. With two condensed benzene rings, the N part could became either phenanthridine as in complex Ir(pbq-F)₂acac (Su et al., 2003) or benzo[f]quinoline as in complex Ir(pbq-f)₂acac (Qiao et al., 2009) as shown in the upper part of Figure 4. However, these two complexes did not show the desired redshift as their counterpart complex 2 did. The reason is that the FMOs did not localize much on the newly extended ring; thus, it did not lower the LUMOs' energies by extending the conjugation length.

The C part

Extending conjugation and/or replacing the benzene ring with electron-rich hetero rings are widely used for the modification of the C part. The effects of the two approaches are much different from those in the N part because of the differences in the distribution of FMOs. On the N part, the condensed rings or hetero-atoms nearly only contribute to the LUMOs, whereas on the C part, they contribute to both HOMOs and LUMOs. Extending conjugation of the C part can lower the π and π^* energies of the ligands at the same time, with little influence to the energies of d-orbitals of iridium core, which leads to an overall reduction of emission energy and redder emission. In comparison, employing electron-rich hetero rings on C part can mainly lift up the energies of HOMOs, with a minor effect on the energies of LUMOs, which likewise leads to a reduction of emission energy and redder emission. Although the effects of the modification on the C part largely depends on the specific structures, one trend is clear that, with a similar degree of modification, the redshift effect is more remarkable on the N part than on the C part.

Extending the conjugation of the C part was used in complex 1 as depicted in Figure 5 (Williams et al., 2006). By replacing the benzene ring with a pyrene ring, a great redshift of about 100 nm was achieved. The pyrene ring was also used as the C part with a t-Butyl substitution in complex 22 (Liu et al., 2018b). The aromatic rings condensed on the C part were not limited to benzene rings. Yu and Zhu et al. reported a series of complexes with triazole rings condensed at the benzene ring of the C part of piq (Yu et al., 2016, 2019, 2020), such as complex 30. Generally, the triazole is an isoelectronic species with the thiadiazole ring. Although the nitrogen atom with an n-Octyl substitution may be more electron rich than a sulfur atom, it did not change the overall electron-deficient feature of the whole ring. Along with the electron-rich peripheral substitution of triphenylamine, the modifications on the C part became somehow self-contradictory to get redshift.

Other than extending conjugation, replacing the benzene ring with a thiophene ring has long been used (Figure 6). A thiophene ring replacement in ppy led to a 36 nm redshift (514 nm → 550 nm). A further benzene ring condensed on the thiophene ring gave another 46 nm redshift (550 nm → 596 nm). The same modification performed on piq led to a 24 nm redshift (620 nm → 644 nm) (Tsuboyama et al., 2003) and a 46 nm redshift (644 nm → 690 nm) (Ikawa et al., 2013), respectively. This method has attracted much attention in the construction of NIR emitters owing to the relatively large redshift brought by thiophene and benzothiophene. The 1-benzo[b]thien-2-yl-isoquinoline (btiq) is easy to synthesize and has been a frequently used cyclometalated ligand in NIR Ir(III) emitters, such as complexes 6 (Ikawa et al., 2013), 7 (Li et al., 2014), 14, 15, 16 (Kesarkar et al., 2016), 23 (Fu et al., 2018), 27 (Guo et al., 2019), and 29 (Zhou et al., 2019a). The resulting complexes are just enough to give emissions around 700 nm with moderate PLQYs. Similarly, 2-benzo[b]thien-2-yl-quinoline (btq), the isomer of btiq, was also reported to develop NIR-emitting complexes, in which some electron-deficient substitutions were employed to realize NIR emission, as in complexes 24, 25 (Kim et al., 2018a), 41, and 42 (Kim et al., 2020a).

The peripheral substitution part

The part other than the coordinated N part and C part is the peripheral substitution (PS) part, which is usually connected by a single bond to the N part and/or C part. So the PS part has less contribution to the FMOs than the N and C parts, which means the modification of the PS part is less effective on tuning emission energy. Meanwhile, the PS part plays an important role in adjusting solubility and processability of the materials. As the emission steps into the NIR region, with the modifications on the N and C parts, the cyclometalated ligands become rather bulky and rigid, which leads to reduced solubility and sublimation ability of the resulting Ir(III) complexes. Sometimes, the harmful molecular aggregations accompany as well. In this situation, the PS part can help with improving solubility and sublimation ability, and inhibiting molecular aggregations, which are crucial for the fabrication of high-performance OLED devices.

The flexible alkyl and alkoxy groups were often used to improve solubility (Figure 7). Besides, these groups are electron rich and bring extra emission redshift. The substitution position is important for adjusting emission wavelength. Attaching these groups on the HOMOs localized part (usually the C part) is more effective to get redshift (You et al., 2019, 2020b). Meanwhile, the flexible chains may bring extra vibration modes and lead to higher k_{nr} (Zhang et al., 2020). In some cases, the alkoxy groups are more detrimental to the PLQY than the alkyl groups, probably because the $n\pi^*$ state brought by the oxygen atom would quench the emissive excited state, as in complex 44 (You et al., 2020b). Similar side effect appeared in complexes with ethoxy acyl group, as in complexes 24 and 41 (Kim et al., 2018a, 2020a, 2020b).
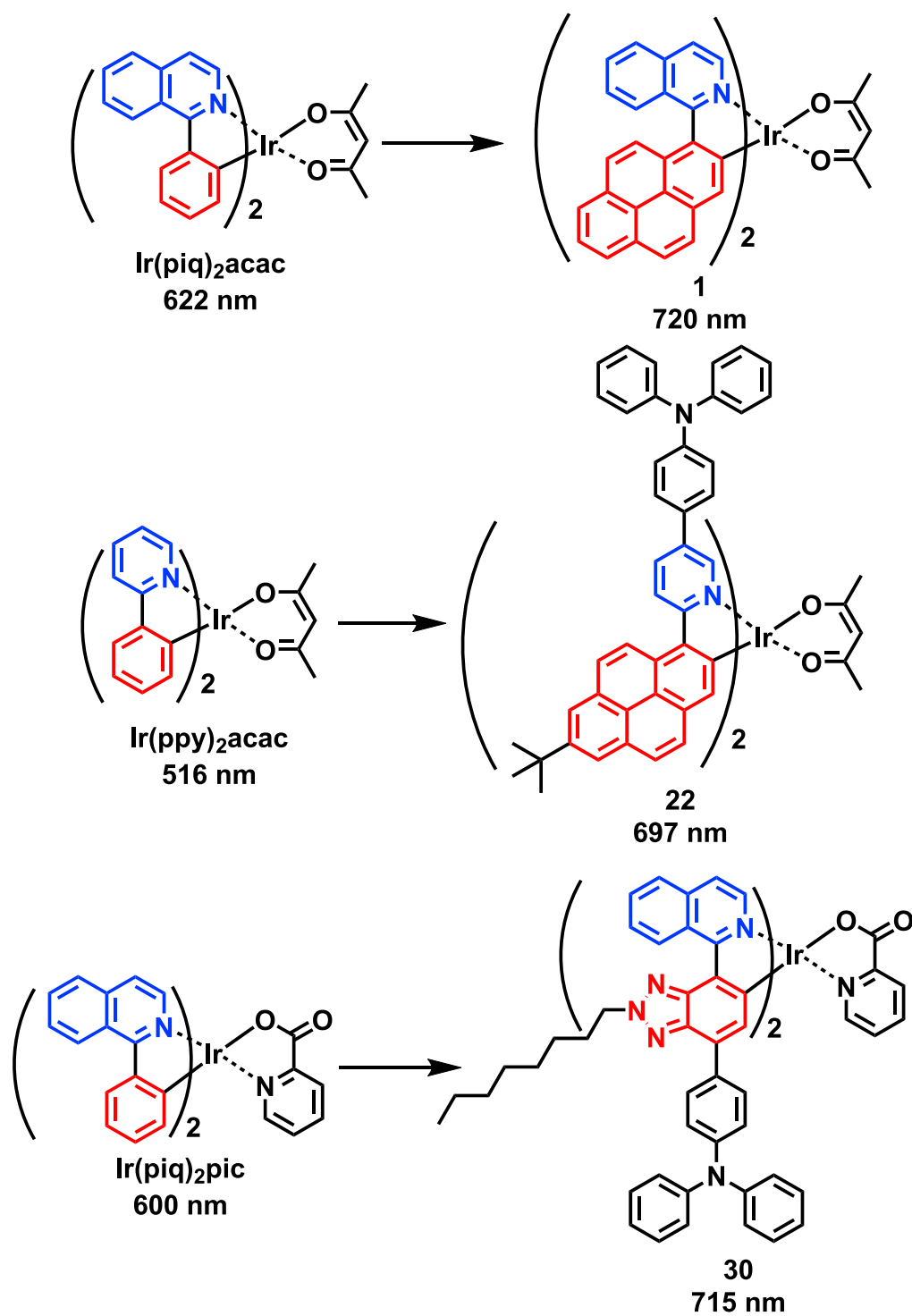
Figure 5. Representative Ir(III) complexes with C part modifications by ring condensations on the benzene toward NIR emission

Their PL emission wavelengths in dilute solutions are also provided.

In terms of improving the sublimation ability, the trifluoromethyl group was frequently used (Chen et al., 2018; Xue et al., 2017). Employing the CF_3 group could effectively lower the sublimation temperature of the Ir(III) complexes, like complex 19 (Xue et al., 2017). Besides, the CF_3 group is electron deficient and
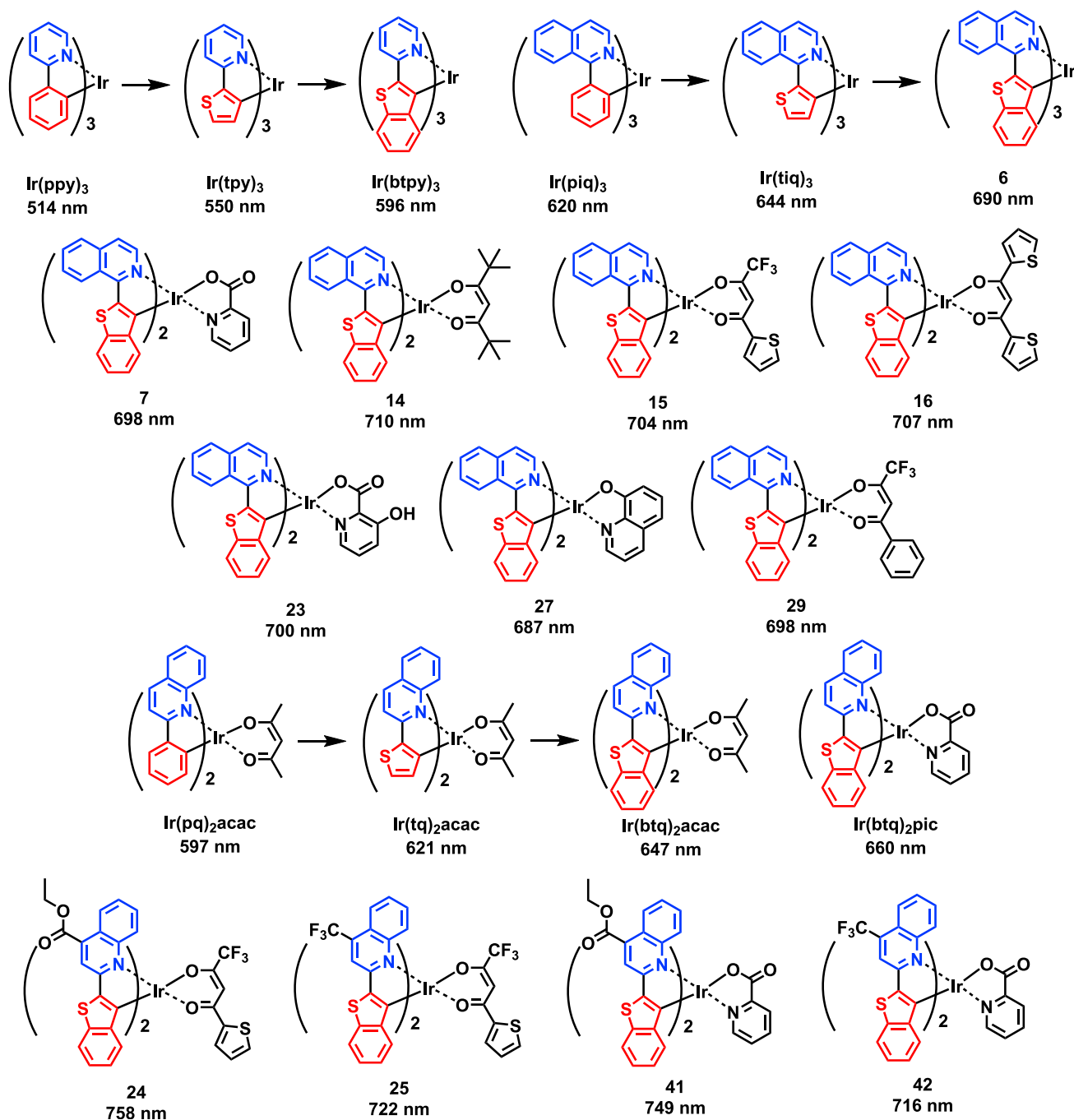
Figure 6. Representative Ir(III) complexes with C part modifications based on thiophene rings
Their PL emission wavelengths in dilute solutions are also provided.

can help with adjusting energy levels. Similar to the CF_3 group, the cyano (CN) group is a rather electron-deficient group. Chen et al. found a halide substrate with a cyano group and synthesized cyano-substituted piq and tiq ligands and resulting Ir(III) complexes 39 and 40 (Chen et al., 2020). The influence of CN on the LUMOs is much more significant than that on the HOMOs. Accordingly, the use of CN can significantly reduce the emission energy of phosphors, changing the red-emitting Ir(piq)$_2$(acac) to the NIR-emitting complexes 39 and 40. Besides, the CN group has a rigid structure, which would bring little extra vibration modes.
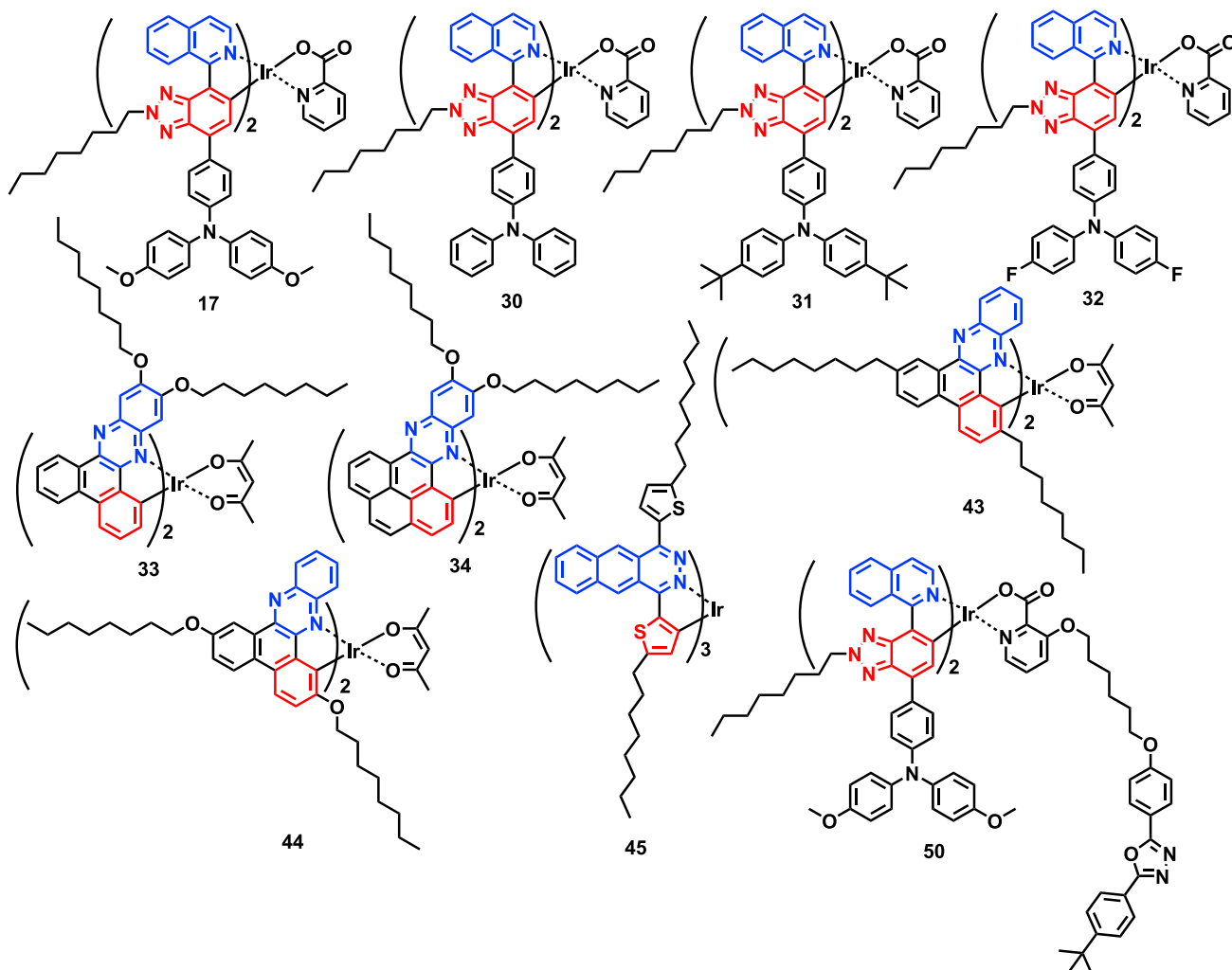
Figure 7. Representative NIR-emitting Ir(III) complexes with flexible chains linked directly on the core of ligands

Other than aliphatic substitutions, the bulkier aromatic ones were also often used, like the triphenyl-amine (TPA) group (Hao et al., 2018; Liu et al., 2018b; You et al., 2020a), fluorenyl (Cao et al., 2015), and thienyl (You et al., 2020a) as shown in Figure 8. The aromatic groups connecting by single bonds have less contribution to the FMOs and emission energies than those condensed on the conjugated parts. Of importance, incorporation of those sterically hindering dendrons at the periphery of an emitting core is a widely recognized method for achieving high solid-state PLQY (You and Park, 2009). Using the dendritic structures could suppress hazardous ground-state and excited-state interactions, such as ag-gregates and excimer formations. This shielding (or site-isolation) strategy is more important for the phosphorescent materials because their excited-state lifetime is generally much longer than those of fluorescent materials. Moreover, the aromatic substitutions were often combined with alkyl groups and alkoxy groups as in complexes 8, 9 (Cao et al., 2015), 46, and 47 (You et al., 2020a), acting as spacers between flexible chains and emitting cores. In addition to improving solubility, the side effect of flexible chains with the nonradiative loss is also suppressed. Moreover, the TPA group was frequently used to improve the hole transporting ability of complexes and their performances in OLED devices (Yu et al., 2016, 2019, 2020).

Notably, Zhu et al. reported a series of complexes based on dibenzo[*a,c*]phenazine ligands, in which the N part, C part, and part of PS part were conjugated (Figure 9) (You et al., 2019, 2020a, 2020b). The rather rigid structure resulted in low Huang-Rhys factors and small k_{nr}. The harmful aggregations between complexes
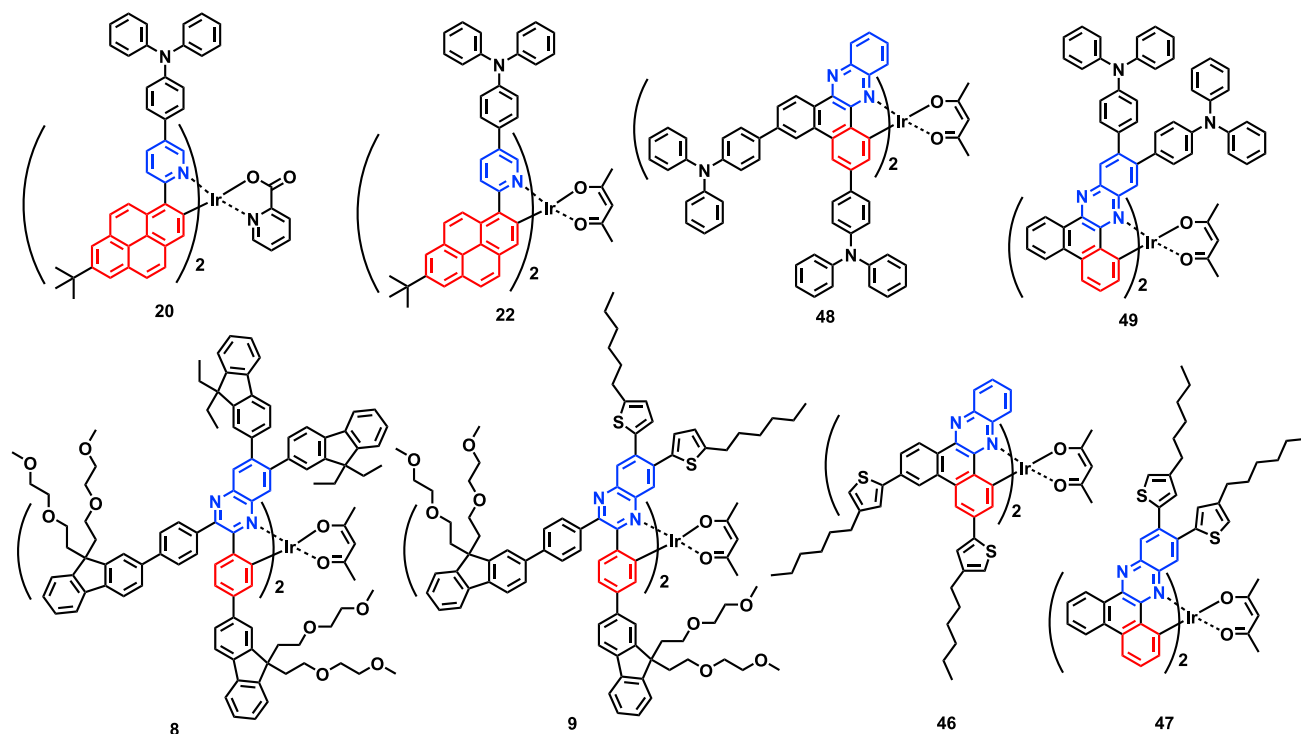
Figure 8. Representative NIR-emitting Ir(III) complexes with aromatic substitutions and aromatic substitutions combined with flexible chains

were effectively suppressed by the peripheral substitutions. Taking complex 48 as an example, its Huang-Rhys factor and k_{nr} were the smallest among complexes 46–49. The intermolecular aggregation of complex 48 was also suppressed successfully in 2.0 wt% doped OLED devices, which realized a maximum EQE of 13.72% at 708 nm, being the best efficiency among reported NIR OLEDs based on Ir(III) complexes (You et al., 2020a).

In a word, the PS part was originally used to improve the processability of the corresponding complexes. But it has some accompanying influences to the overall performance, which were the tricky part to deal with. Herein, some implications could be drawn for the PS part in the development of high-performance Ir(III) complexes:

1) To improve solubility, alkyl groups are preferred than alkoxy groups. Besides, placing the flexible alkyl chains away from the FMOs is helpful to decrease k_{nr}, unless it is desperately needed to redshift the emission. When directly connecting with the emitting cores, less flexible ones, such as *t*-butyl, are preferred.

2) To improve sublimation ability, keeping relatively low molecular mass is effective in most cases. Introducing CF_3 substitution can improve thermal stability and lower sublimation temperature.

3) Incorporation of sterically hindering dendrons is effective in inhibiting molecular aggregations. The combination of dendrons with alkyl or alkoxy chains can reduce the side effect of flexible chains on k_{nr}.

The ancillary ligand

Limited by coordination ability, the corresponding facial homoleptic complexes of some cyclometalated ligands are hard to be synthesized. As an alternative, the ancillary ligands are involved to coordinate with iridium and form heteroleptic complexes. According to their contribution to the FMOs of the complexes, ancillary ligands can be divided into two types: the non-chromophore and the chromophore. Acac is a typical non-chromophore one, which usually shows minor contribution to the FMOs, thus has little influence on photophysical properties. Since it is more frequently used than any other ancillary ligands
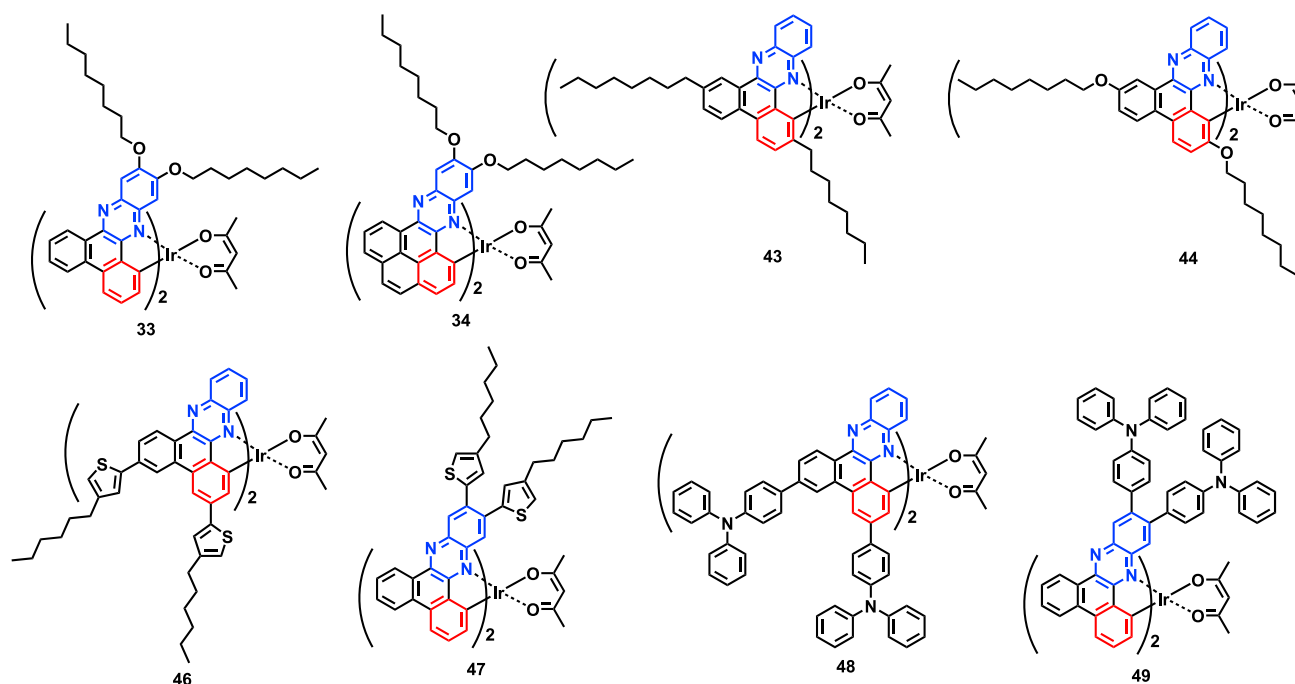
Figure 9. Representative NIR-emitting Ir(III) complexes based on dibenzo[*a,c*]phenazine ligands

(Figure 3), the heteroleptic complexes-based acac can be seen as preferences for cyclometalated ligands. Some bulkier acac derivatives were employed to suppress possible distortions in excited states, thus lowering the k_{nr} for red-emitting Ir(III) complexes as shown in Figure 10 (Baek et al., 2020). Besides, picolinic was also used as non-chromophore ancillary ligand in some cases.

The chromophore ancillary ligands, like amidinate and amide derivatives were often used in red-emitting Ir(III) complexes (Kabir et al., 2020; Lai and Teets, 2019; Lai et al., 2018; Liang et al., 2020; Su et al., 2020). Recently, Teets et al. reported several NIR Ir(III) complexes with the chromophore ancillary ligands as complexes 51–55 in Figure 3 (Lai et al., 2020). They found that electron-rich ancillary ligands can lift up the energy of d-orbitals and lower the MLCT state energy, thus reducing the energy separation between ^{3}MLCT and ^{3}LC (Figure 11). The incorporation of these chromophore ancillary ligands may reduce the contribution of "direct SOC" with respect to the non-chromophore ancillary ligand complexes, because the contribution of iridium to the HOMOs decreases. But it is beneficial for the efficiency of "indirect SOC" because of the reduced energy denominator of the CI matrix element as shown in Figure 11B. As a result, the emissive triplet states have a more MLCT character and higher k_r. In addition, one more thing to mention is that there is usually a balance point. If the ancillary ligands are excessively electron rich, they might dominate the HOMOs, with less contribution from iridium and cyclometalated ligands (Figure 11C), which would decrease the overall MLCT character and lead to low PLQY.

In most cases, one has no need to hesitate to synthesize which configuration in the actual synthesis process, since the product of the reaction to form the intermediate chloride-bridged binuclear Ir(III) dimer could largely reflect the coordination ability of the cyclometalated ligand. Usually the product is the dinuclear Ir(III) dimer, and in this situation, synthesizing the heteroleptic complexes is the favored choice. Sometimes, the product is a mixture of the binuclear Ir(III) dimer and facial homoleptic complexes, even the latter being the main product, which just reflect strong coordination ability of the ligands, and in this situation, synthesizing facial homoleptic complexes is the best choice (Xue et al., 2017; Zhang et al., 2020). In some cases, the binuclear Ir(III) dimer cannot be synthesized by the most commonly used $IrCl_3 \cdot nH_2O$, and in this situation, an iridium-containing starting material with higher activity than $IrCl_3 \cdot nH_2O$ is needed, such as the $[Ir(COD)]_2Cl_2$ (COD = 1,5-cyclo-octadiene) (You et al., 2019, 2020a, 2020b). Along with the improvement of reaction conditions, such as adding base, using different solvents, and adjusting the reaction temperature, the binuclear Ir(III) dimer might be successfully synthesized, then the synthesis of heteroleptic complexes is feasible, otherwise some modifications are needed to improve the coordination ability of ligands.
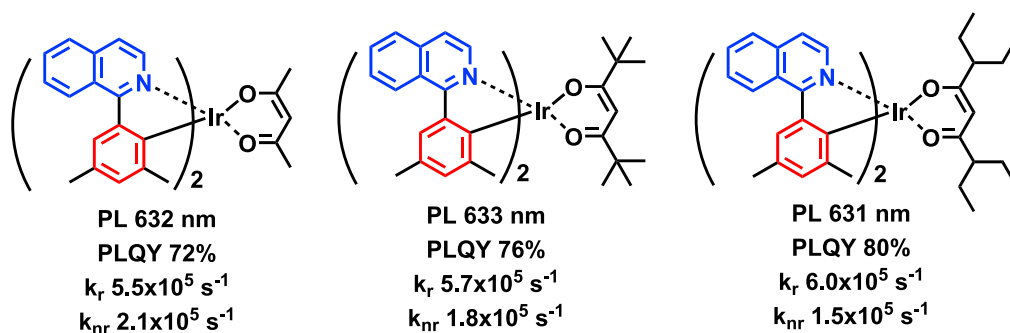
Figure 10. Examples of red-emitting Ir complexes with acac-based ancillary ligands

Below each structure:

PL 632 nm
PLQY 72%
k_r 5.5x10^5 s^{-1}
k_{nr} 2.1x10^5 s^{-1}

PL 633 nm
PLQY 76%
k_r 5.7x10^5 s^{-1}
k_{nr} 1.8x10^5 s^{-1}

PL 631 nm
PLQY 80%
k_r 6.0x10^5 s^{-1}
k_{nr} 1.5x10^5 s^{-1}

Other NIR-emitting Ir(III) complexes

Other than the typical mononuclear homoleptic and heteroleptic Ir(III) complexes as discussed above, there are some other NIR Ir(III) complexes such as binuclear complexes with tetradentate ligands and Ir(III) corroles as shown in Figure 12. We would only take a glance at some representative ones. Some of the binuclear ones exhibit similar photophysical properties (similar emission wavelength and comparable PLQY) to their mononuclear counterparts, such as complex 20 (PLQY 2.25% at 698 nm) compared with complexes 56 (PLQY 0.70% at 699 nm) and 57 (PLQY 1.22% at 700 nm) (Hao et al., 2018) and complex 29 (PLQY 8% at 698 nm) compared with complex 58 (PLQY 15% at 722 nm) (Zhou et al., 2019a). Although complex 59 does not have a specific mononuclear counterpart, its peak emission wavelength at 709 nm is similar to that of other mononuclear complexes based on btiq C^N ligands (He et al., 2020a). In most cases, these binuclear complexes have a specific non-chromophore ancillary ligand bridging two iridium cores, so that their photophysical properties mainly anchored by C^N ligands and Iridium core remain to a large extent. One special exception is complex 60, of which the bridge ligand is a chromophore double-bidentate C^N ligand, showing NIR phosphorescence (714 nm with a shoulder at 790 nm), which is accompanied by weak green fluorescence (537 nm with a shoulder at 571 nm) resulting from the strong LC character of the S_1 and T_1 excited states (Shafikov et al., 2020). The LC character led to poor PLQY of 3.5%. Likewise, Ir(III) corroles were proved to be LC emission with rather low PLQY, such as complex 61 with 1.2% PLQY at 792 nm (Palmer et al., 2010).

APPLICATIONS IN NIR-OLEDs

Device structures and performances

OLEDs possess a multilayered structure, consisting of emission layers (EMLs) and other functional layers to facilitate the injection, transportation, and confinement of charge carriers, including charge-injecting, charge-transporting, and charge-blocking layers sandwiched between the ITO anode and the low-work-function metal cathode. Figure 13 describes a simplified working mechanism of OLEDs (Ma et al., 2017). Under an applied bias, electrons and holes are injected from the cathode and anode into the electron-transporting layer (ETL) and hole-transporting layer (HTL), respectively, through a "hopping mechanism" between the localized π-electron states. Since the emission lifetime of a phosphorescent Ir(III) complex is relatively long, on the scale of a microsecond or submicrosecond, it is usually doped in host material at low concentration in EML to avoid efficiency loss caused by TTA. When charge carriers reach the EML, there are two mechanisms to generate excited Ir(III) phosphors (Li et al., 2018): (1) an excited host molecule passes the energy to a ground state guest emitter molecule and (2) the free charge carriers are directly trapped by an emitter molecule via a charge transfer process from the host molecule to the emissive guest molecule. Ideally, with an optimized host-guest system, obeying principles such as a higher triplet energy level of the host molecule than the guest, good charge mobility of both host and guest, and balanced charge injection in the EML, all the excitons could be harvested by the emitters. The Ir(III) phosphors with strong SOC are able to utilize the normally nonradiative triplet excitons (25% singlet and 75% triplet, according to spin statistics) and achieve rather higher IQE, theoretically approaching 100%.

With all the designs and modifications in molecular structures, some NIR iridium complexes have been employed to fabricate NIR-OLEDs. The EQEs of the corresponding NIR-OLEDs are shown as a function of emission peak maximum in Figure 14. The corresponding device structures and performances are

A Large ΔE(^{3}LC-^{3}MLCT), Weak CI   **B** Small ΔE(^{3}LC-^{3}MLCT), Strong CI   **C** ^{3}LLCT dominates
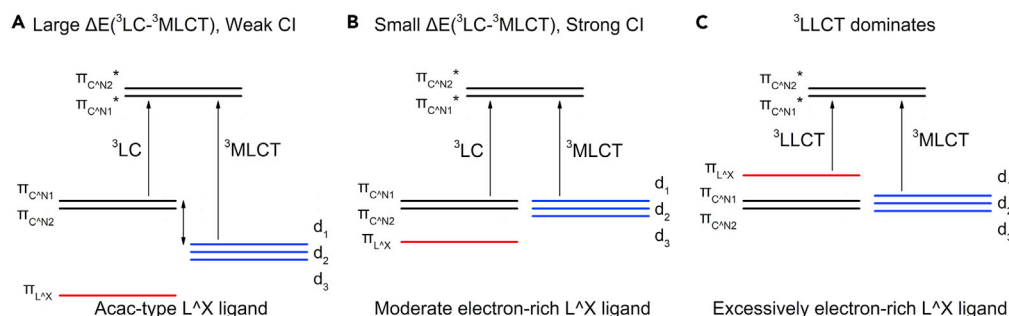
Figure 11. Qualitative diagram showing the possible effect on MLCT caused by incorporating electron-rich ancillary ligands
(A) The energy states of Ir complexes with common non-chromophore ancillary ligands.
(B) The energy states of Ir complexes with moderate electron-rich ancillary ligands.
(C) The energy states of Ir complexes with excessively electron-rich ancillary ligands.

summarized in Table 2. The molecular structures of other functional materials employed in NIR-OLEDs are shown in Figure 15. One can notice that, for the emission into the real invisible NIR region, the related reports are few and the EQEs are low.

As listed in Table 2, all the devices employed ITO as anode. As for cathode, except that our group was limited by equipment in early days (No. 2, 5, 18, 19), using Mg:Ag cathode, all the devices used vacuum-evaporated Al as cathode. Besides, thin layers of several nanometers of alkali metals salts (LiF, Liq, CsF, Cs_2CO_3) or alkaline earth metal (Ba) were deposited before Al to lower electron injection barriers and enhance electron injection. Apart from the electrodes, the material selection of HBL/ETL layers of these reported devices shared much in common. Except two early reports using Alq$_3$ and three reports using BCP/Bphen (similar in structures), all the devices employed either TPBi or TmPyPB as HBL/ETL. The two materials are frequently used in OLEDs to provide high electron mobility, favoring electron transport (Shahnawaz et al., 2019). The energies of triplet excitons from NIR-emitting Ir(III) complexes are far below those of TPBi and TmPyPB (>700 nm emissions, < 1.77 eV triplet energy versus 2.73 eV for TPBi, 2.78 eV for TmPyPB), resulting in efficient exciton confinement. The energies of HOMOs of TPBi and TmPyPB are also deep enough (−6.2 eV for TPBi and −6.68 eV for TmPyPB) for blocking holes. The electron mobility of TmPyPB (1.0×10^{-3} cm^{2}V^{-1}s^{-1}) is higher than that of TPBi (3.3×10^{-5} cm^{2}V^{-1}s^{-1}), making TmPyPB a preferred choice in more recent reports of NIR OLEDs.

The device fabrication processes for these NIR OLEDs are either thermal vacuum evaporation or spin-coating deposition. In the reports of NIR-OLEDs based on Ir(III) complexes, the two methods have their own advantages and disadvantages. Solution process has much higher material utilization ratio than vacuum evaporation and relatively simpler fabrication process. Technically, it is suitable for manufacturing large-area devices at low cost but still suffers from the limitation on the optimization of device structure and performance in most cases. Vacuum evaporation enables the formation of multiple layers, and precise control in thickness without significant interface erosion; thus it has much space to improve the device performance.

For those solution-processed NIR-OLEDs, PEDOT:PSS has been widely used as HIL because it has relatively high conductivity and is almost transparent with good stability. Moreover, PEDOT:PSS is a water-dispersed polyelectrolyte emulsion with great film-forming properties; hence, it can avoid the interface erosion with the emissive layer processed from the low polarity organic solvent (Zhong et al., 2011). In some cases, more materials were employed between PEDOT:PSS and EML as listed in Table 2, reported to act as (1) interfacial layer, such as TFB; (2) another HIL, such as PVK; and (3) HTL, including poly-TPD and TAPC. For the EML, combinations of PVK either with PBD or OXD-7 are more often used than other hosts. The HOMO/LUMO levels of NIR-emitting Ir(III) complexes usually can be well embedded between the HOMO level of PVK and the LUMO level of PBD/OXD-7, thus favoring efficient energy transfer. CBP is another common choice for host, which also can be used in vacuum evaporation process.

The reports of NIR-OLEDs fabricated with full thermal vacuum evaporation are far less than solution-processed ones. The major reason is that the emission redshifts of Ir(III) complexes were usually at the expense
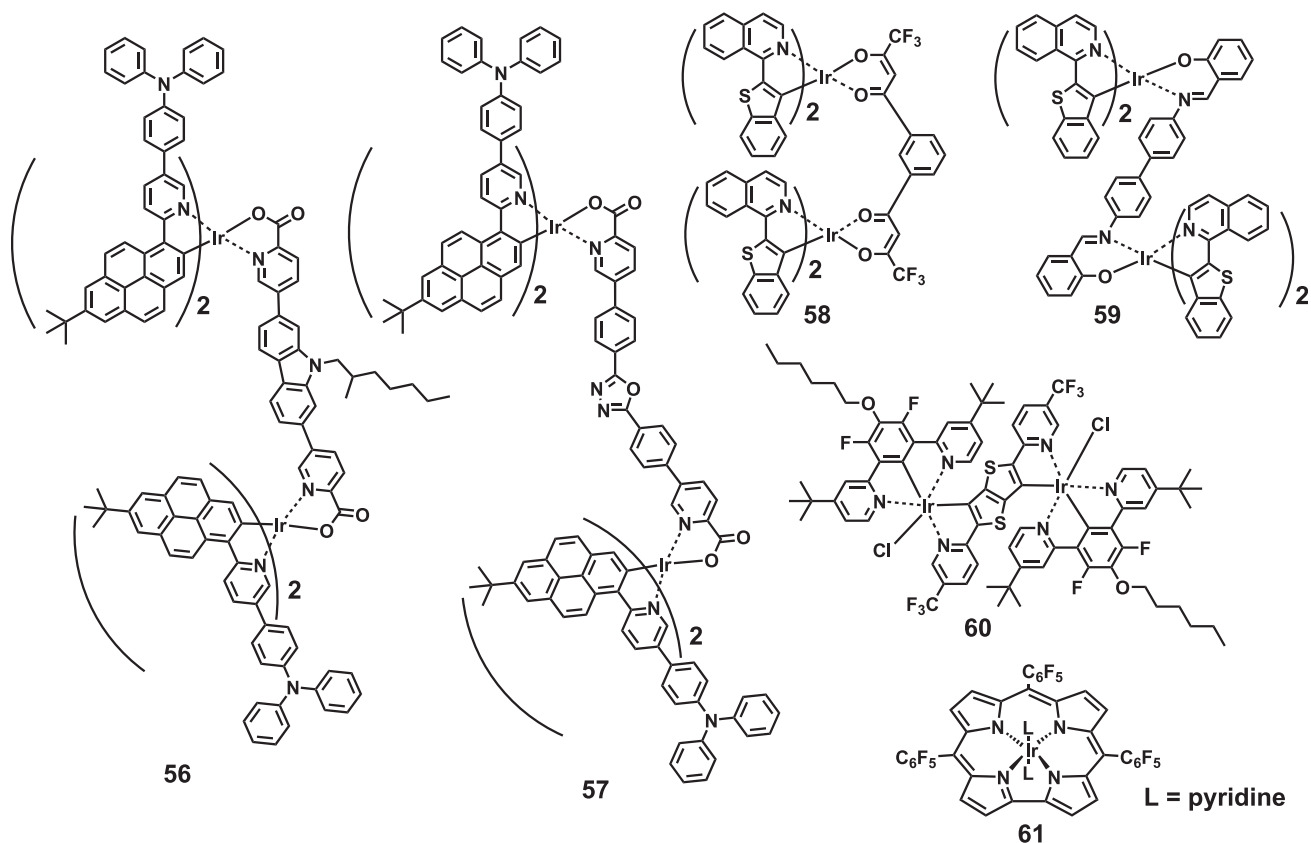
Figure 12. Examples of binuclear Ir(III) complexes and Ir(III) corroles complexes

of more complex structures, making them less sublimable. In the reports of our group (No. 2, 5, 18, 19), we employed NPB as HTL. Chen et al. employed HAT-CN as HIL and TAPC as HTL (No. 26, 39, 40). For devices of complexes 39 and 40, a 5-nm mCP layer was used as another hole conductive EBL. As for the EML, these reports employed different hosts, although complete energy transfer from host to guest was realized with optimized doping ratio except complex 18 being not stable in thermal vacuum evaporation.

When devices work under applied voltages, direct charge trapping was thought to be the main exciton formation mechanism occurring within the NIR-emitting Ir(III) complexes (Cao et al., 2015; Fu et al., 2018; Kesarkar et al., 2016; Kim et al., 2020a; Xue et al., 2017; You et al., 2020b). Besides, when employing suitable hosts, the efficient Förster energy transfer can also facilitate the exciton formation based on significant spectra overlap between the emission of host and the absorption of complexes (Fu et al., 2018; Xue et al., 2017). The EL spectra usually exhibit less dependence from driving voltages and correspond well with the PL spectra in similar emission band shape and wavelength. With the doping ratio increasing in the EML, the EL spectra usually redshift a small margin because of the weak intermolecular aggregation.

The efficiency roll-off with increasing current density is a big issue in phosphorescent OLEDs, which can be ascribed to multiple quenching mechanisms, including (1) TTA (Baldo et al., 2000; Reineke et al., 2007a, 2009; Song et al., 2010), (2) triplet-polaron quenching (TPQ) (Baldo et al., 2000; Reineke et al., 2007a, 2009; Song et al., 2010), and (3) electric field-induced exciton dissociation (Kalinowski et al., 2002, 2006). Among them, the first two can be facilitated by the long radiation lifetime of the triplet excitons and the aggregation formation of the emitter dopants. Usually for NIR-emitting Ir(III) complexes, the bulky aromatic cyclometalated ligands and octahedral configuration can intrinsically suppress the molecular aggregation, hence lowering efficiency roll-off. Besides, the typical short lifetimes of microseconds or submicroseconds as listed in Table 1 are also related with the octahedral configuration and mainly benefit from the larger MLCT character and more efficient SOC (Yersin et al., 2011). In addition to TTA and TPQ, device parameters such as a broad recombination zone and well-matched energy levels can also help reduce the efficiency
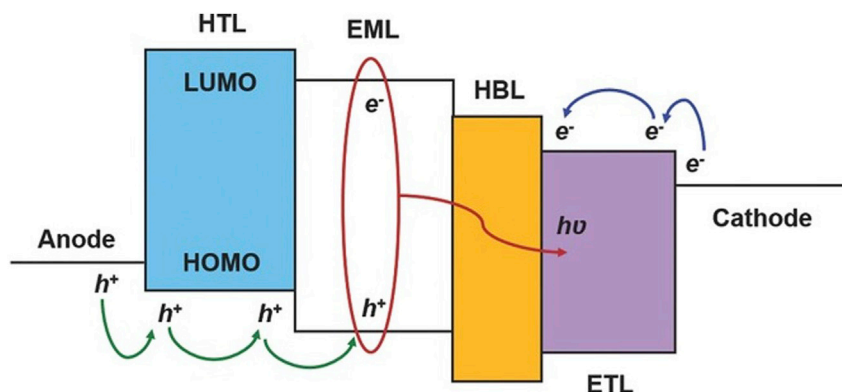
Figure 13. Schematic working mechanism of OLEDs
(Ma et al., 2017) Copyright 2017, Wiley-VCH.

roll-off in NIR OLEDs based on Ir(III) complexes. Well-balanced injection and transport of electrons and holes will consequently make the majority of electron-hole recombination events occur in the bulk emitting layer and not at the interface of HTL/EML or EML/ETL. In addition, the HOMO/LUMO levels of emitters located right between those of the host material can suppress the electric field-induced quenching and thus minimize the efficiency roll-off in devices.

Coordination geometry and outcoupling efficiency for OLEDs

For OLED devices, its EQE can be expressed as Equation 8 (Kim and Kim, 2018):

$$\eta_{EQE} = \gamma \times \eta_{S/T} \times q_{eff}(\varphi_{PL}, \Gamma) \times \eta_{out}(\Theta, \Gamma) \qquad \text{(Equation 8)}$$

where γ is the charge balance factor; most of device optimizations try to make the charge balance factor approaching unity. $\eta_{S/T}$ is the fraction of excitons that is allowed to decay radiatively by spin statistics ($\eta_{S/T}$ = 1 for phosphorescent emitters like Ir(III) complexes) and q_{eff} is the effective radiative quantum yield of the emitter in the cavity structure (Kim et al., 2013). It should be noted that q_{eff} is a function of the PLQY of the emitter in free space and the device structure influencing radiative decay rate via Purcell factor (Γ), including the position of the emission zone (Neyts, 1998; Nowy et al., 2008). η_{out} is the outcoupling efficiency, which depends on Γ and the emitting dipole orientation (EDO). The EDO can be represented as the fraction of the horizontal emitting dipole moment, $\Theta \equiv (p_\parallel /p_\parallel + p_\perp)$, where $p_\parallel$ and $p_\perp$ represent the horizontal and vertical components of the emitting dipole, respectively.

The dependence of η_{out} on EDO can be understood from the emission pattern of light from an oscillating dipole, as shown in Figure 16. The vertical emitting dipoles emit light largely propagating in a horizontal direction. In contrast, the horizontal emitting dipoles emit light largely propagating in a vertical direction, which is beneficial to improve η_{out}(Kim and Kim, 2018).

In Equation 8, there are two factors mostly determined by the molecular structures of emitters: PLQY and EDO. In the above two sections, we have explored the structure-efficiency relationship and summarized the effective strategies to improve the PLQY for NIR-emitting Ir(III) complexes. Nevertheless, high-efficiency NIR-OLEDs are still rare. Herein, we explore the effect of coordination geometry and EDO on η_{out} and EQE for NIR-OLEDs based on Ir(III) complexes.

For Ir(III) complexes, the triplet transition dipole moment (TDM) is an oscillating dipole, and it roughly aligns along the Ir-N bonds (Figure 17). For the facial homoleptic complexes, i.e., the *fac*-Ir(ppy)$_3$ type, the three TDMs are nearly orthogonal to each other and thus are triply degenerate. In comparison, for the heteroleptic complexes, i.e., the Ir(ppy)$_2$acac type, the two TDMs are parallel. The inherent asymmetry of the Ir(ppy)$_2$acac-type complexes can benefit alignment of aliphatic ligand toward the vacuum side, and thus facilitate the horizontal emitting dipoles and improve η_{out}. In addition, on the surface of organic layer, the π-π interactions between the dopant and host molecules can likewise result in alignment of the aliphatic ligands on the vacuum side and improve η_{out}(Kim and Kim, 2018).
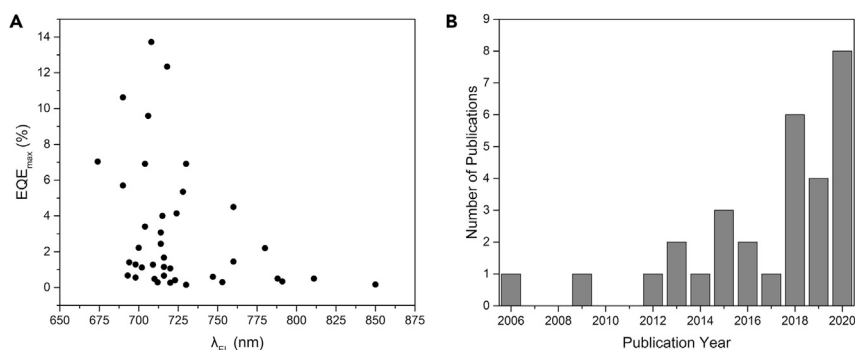
Figure 14. NIR-OLEDs based on Ir(III) complexes

(A) Peak emission wavelengths and maximum external quantum efficiencies of NIR-OLEDs based on Ir(III) complexes reported so far.

(B) Number of publications about NIR-OLEDs based on Ir(III) complexes reported so far.

Notably, for *fac*-Ir(ppy)$_3$-type complexes, the η_{out} can also be improved, which has been reported in blue-emitting facial homoleptic Ir(III) complexes (Kim et al., 2020b). An electron-withdrawing CN group was introduced to the phenyl ring on the C part, which made the TDMs shift toward the Ir-C bond and nearly perpendicular to the C$_3$-axis and thus enhanced EDO. Kim et al. gave a more universal description of the relation between EDO and molecular orientation of facial homoleptic Ir(III) complexes (Huh et al., 2020). They found that the degree of change in EDO is correlated with the directions of the TDMs against the C$_3$ axis (a line connecting Ir atom and the center of gravity of three Ir-bonded N atoms) and the orientations of the C$_3$ axis in films. Two angles are defined (Figures 18A and 18B): ϕ is the angle between the TDM and the C$_3$ axis and θ is the average polar angle of the C$_3$ axis with respect to the plane-normal z axis in films. The EDO value of facial homoleptic Ir(III) complexes is related to both angles and can be described as Equation 9:

$$EDO = 1 - \frac{\sin^2\phi\sin^2\theta + 2\cos^2\phi\cos^2\theta}{2} \qquad \text{(Equation 9)}$$

The contour plot in Figure 18F graphs EDO as a function of ϕ and θ. If either the ϕ or θ value is 54.7°, EDO becomes 2/3 (dot-dash lines), corresponding to an isotropic orientation. This is intuitive because the three TDMs are orthogonal to each other when ϕ = 54.7°. Similarly, the sum of the horizontal components of the three TDMs is twice the sum of the vertical components when θ = 54.7°, irrespective of the ϕ value. A preferred horizontal orientation with EDO >0.67 is obtained when θ < 54.7° and ϕ > 54.7°, or when θ > 54.7° and ϕ < 54.7°. Perfect horizontal orientation is achieved when θ = 0° and ϕ = 90°, or when θ = 90° and ϕ = 0°. The ϕ is determined by the molecular structures and can be adjusted to some extent via ligands modification. For three typical Ir(III) complexes in the visible region, Ir(ppy)$_3$, Ir(pq)$_3$, and Ir(piq)$_3$ (Figures 18C–18E), their ϕ angles are 85.5°, 66.1°, and 79.0°, respectively. The larger the ϕ angle, the larger the variation range of EDO is with the same variation of the θ angle, as shown in Figure 18G. In comparison, the influence factors of the θ angle are more complex. The interactions between emitters and hosts is crucial. The dipole-dipole (or dipole-induced dipole) interactions will become dominant when the permanent dipole moments of both emitter and host are large. The π-π interactions may be responsible for the preferred orientation when increasing the size of the carbazole-based hosts. Another report claimed the shape of molecules will also influence the orientation of molecules when they are deposited (Schmid et al., 2020). In their opinion, a compressed molecular shape (look along the C$_3$ axis) will bring a higher chance of deposition with the C$_3$ axis perpendicular to the substrate in a completely random deposition process, resulting in a higher EDO.

Although η_{out} has not attracted attention in improving the EQE of NIR-OLEDs based on Ir(III) complexes, some reports based on heteroleptic Ir(III) complexes might have already enjoyed the bonus of this effect, just without noticing it (Chen et al., 2018, 2020; Qiao et al., 2009; Tao et al., 2013). For the future development of NIR-OLEDs, this effect would provide another promising approach to improve EQE other than improving PLQY.

Table 2. Reported device structures and performances of NIR OLEDs (with ITO as the anode)

No.[a]	HIL/HTL	EML(doping ratio)	HBL/ETL	EIL/Cathode	λ_{EL} (nm)[b]	EQE (%)[c]	Radiance (mW·cm^{-2}/ W·sr^{-1}·m^{-2})	CIE
1	PEDOT:PSS	PVK:PBD:1(65:30:5)	BCP/Alq$_3$	LiF/Al	720	0.266	0.238/-	
2	NPB	Alq$_3$:2(90:10)	Alq$_3$	Mg:Ag	720	1.07	4.6/-	(0.64, 0.26)
3	PEDOT:PSS	PVK:PBD:3(50:30:20)	TPBi	Cs$_2$CO$_3$/Al	693	0.67	0.181/-	
4	PEDOT:PSS	PVK:PBD:4(50:30:20)	TPBi	Cs$_2$CO$_3$/Al	753	0.30	0.095/-	
5	NPB	Ga$_2$(saph)$_2$q$_2$:5(80:20)	Bphen	Mg:Ag	780,850(s)	2.2	1.8/-	
6	PEDOT:PSS	PVK:PBD:6(100:30:4)		CsF/Al	694	1.41		(0.65, 0.26)
8	PEDOT:PSS	PVK:PBD:8(59:40:1)	TPBi	CsF/Al	690	5.7	0.566/-	
9	PEDOT:PSS	PVK:PBD:9(59:40:1)	TPBi	CsF/Al	704	3.4	0.444/-	
10	PEDOT:PSS	PVK:PBD:10(50:30:20)	TPBi	Cs$_2$CO$_3$/Al	715(s), 788	0.50	0.1112/-	
11	PEDOT:PSS	PVK:PBD:11(50:30:20)	TPBi	Cs$_2$CO$_3$/Al	791	0.34	0.0572/-	
14	PEDOT:PSS	PVK:OXD-7:14(65:30:5)		Ba/Al	714	3.07	-/1.43	
15	PEDOT:PSS	PVK:OXD-7:15(65:30:5)		Ba/Al	709	1.28	-/3.1	
16	PEDOT:PSS	PVK:OXD-7:16(65:30:5)		Ba/Al	714	2.44	-/4.9	
17	PEDOT:PSS	PVK:OXD-7:17(61.6:26.4:12)	TPBi	Ba/Al	723,780(s)	0.41	0.0741/-	
18	NPB	DIC-TRZ:18(94:6)	TPBi	Mg:Ag	811	0.5	0.0945/-	
19	NPB	DIC-TRZ:19(88:12)	TPBi	Mg:Ag	760	4.5	4.1818/-	
20	PEDOT:PSS/TFB	CBP:PBD:20(60:30:10)	TmPyPB	Liq/Al	698,762(s)	1.29	-/0.0059	
22	PEDOT:PSS	PVK:OXD-7:22(66:30:4)	TPBi	Ba/Al	698,763(s)	0.56	0.0543/-	
23	PEDOT:PSS	PVK:OXD-7:23(63.3:31.7:5)	TmPyPB	LiF/Al	700,760(s)	2.22	-/0.11	
24	PEDOT:PSS	mCP:TCTA:24(10 wt%)	TPBi	Liq/Al	747	0.15		(0.53, 0.42)
25	PEDOT:PSS	mCP:TCTA:25(10 wt%)	TPBi	Liq/Al	730	0.6		(0.59, 0.37)
26	HAT-CN/TAPC	mCP:26(90:10)	TmPyPB	LiF/Al	715	4.0		
29	PEDOT:PSS	PVK:OXD-7:29(65:30:5)	TmPyPB	LiF/Al	702,772(s)	1.12	-/0.047	
30	PEDOT:PSS/PVK	CBP:30(91:9)	TPBi	Ba/Al	712,780(s)	0.29	0.79/-	
31	PEDOT:PSS/PVK	CBP:31(91:9)	TPBi	Ba/Al	716,780(s)	0.66	1.23/-	
32	PEDOT:PSS/PVK	CBP:32(88:12)	TPBi	Ba/Al	710,780(s)	0.48	0.85/-	
33	PEDOT:PSS/poly-TPD	PVK:OXD-7:33(69.3:29.7:1)	TmPyPB	LiF/Al	674	7.04	-/33.671	
34	PEDOT:PSS/poly-TPD	PVK:OXD-7:34(69.3:29.7:1)	TmPyPB	LiF/Al	724	4.14	-/20.981	
39	HAT-CN/TAPC/mCP	CBP:39(85:15)	TPBi	LiF/Al	690	10.62		(0.713,0.274)
40	HAT-CN/TAPC/mCP	CBP:39(85:15)	TPBi	LiF/Al	706	9.59		(0.707, 0.277)
42	PEDOT:PSS/PVK	TCTA:PO-T2T:42(45:45:10)	TPBi	LiF/Al	716	1.674		(0.72,0.28)
43	PEDOT:PSS/poly-TPD	CBP:43(99.0:1.0)	TmPyPB	CsF/Al	730	6.91	-/26.100	
44	PEDOT:PSS/poly-TPD	PVK:OXD-7:44(69.44:29.76:0.8)	TmPyPB	CsF/Al	760	1.45	-/11.518	
45	PEDOT:PSS	CzTPA-m-Trz:45(90:10)	Bphen	LiF/Al	850,948(s)	0.17	0.0525/-	
46	PEDOT:PSS/poly-TPD	PVK:OXD-7:46(69.44:29.76:0.8)	TmPyPB	CsF/Al	704	6.91	-/53.611	
47	PEDOT:PSS/poly-TPD	PVK:OXD-7:47(69.44:29.76:0.8)	TmPyPB	CsF/Al	728	5.35	-/38.165	
48	PEDOT:PSS/TAPC	CBP:48(98.0:2.0)	TmPyPB	CsF/Al	708	13.72	-/26.996	
49	PEDOT:PSS/TAPC	CBP:49(98.0:2.0)	TmPyPB	CsF/Al	718	12.34	-/24.647	
50	PEDOT:PSS/poly-TPD	PVK:OXD-7:50(53.2:22.8:24)	TmPyPB	Liq/Al	716	1.15	-/28.827	

[a]The number corresponds to the molecular structure with the same number, which is consistent with Table 1.
[b]Peak emission wavelengths of electroluminescence in OLED devices, the "s" in the parentheses means shoulder peak.
[c]Maximum external quantum efficiencies of corresponding OLED devices.

HIL/HTL

Host

HBL/ETL
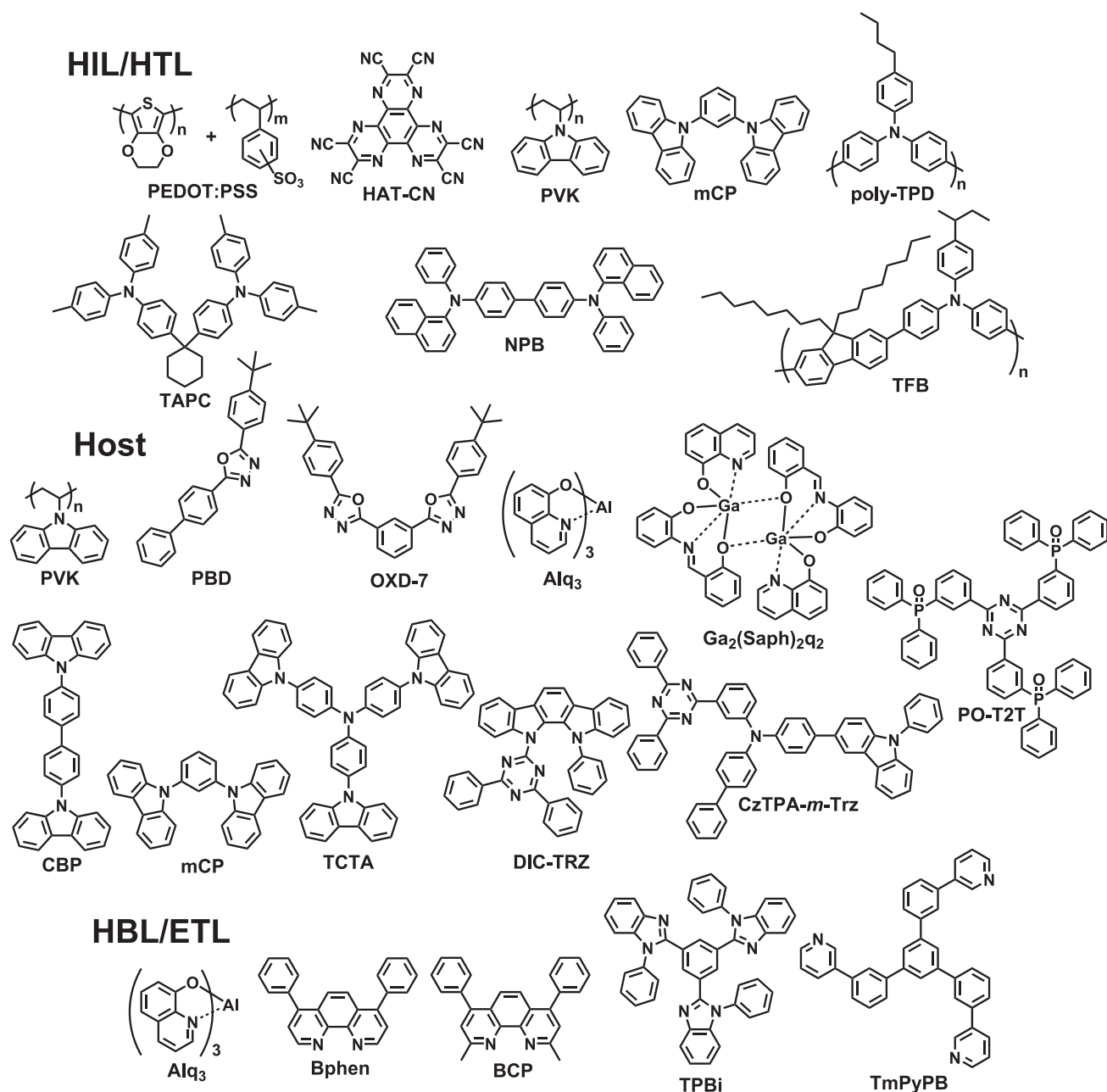
Figure 15. The molecular structures of functional materials employed in reported NIR OLED devices

APPLICATIONS IN BIOLOGICAL IMAGING

Optical imaging is a non-invasive technique for biological applications involving sensing, diagnosis, and therapy (Huang et al., 2020; Zhou et al., 2019b). NIR dyes have attracted growing attention for their great potential to *in vivo* applications (Escobedo et al., 2010; Yuan et al., 2012). There are three NIR biological windows according to optical property: NIR-I (650–950 nm), NIR-II (1,000–1,350 nm), and NIR-III (1,500–1,850 nm) (Hemmer et al., 2013, 2016; Smith et al., 2009; Weissleder, 2001). In particular, the NIR-I range is the diagnostic window that surpasses the visible region and allows for bio-imaging with minimal interference from tissue autofluorescence, reduced light scattering, and high tissue penetration in *in vivo* applications (Kobayashi et al., 2010; Zhou et al., 2012).
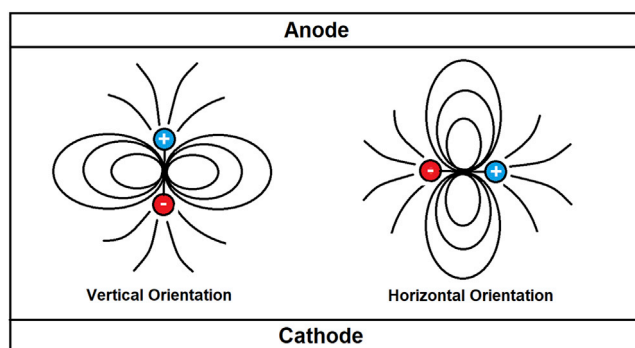
Figure 16. Electromagnetic wave propagation in a weak microcavity structure according to the oscillating dipole orientation
Adapted from (Kim and Kim, 2018).

To date, there are several NIR dyes under development for biological applications, mainly including organic small molecules, QDs, lanthanide complexes, and transition-metal complexes. Among those NIR dyes, various organic compounds are available as NIR fluorophores for bio-imaging applications, but many of them suffer from severe photobleaching, small Stokes shift, low detection sensitivity, etc. The NIR QDs possess a relatively larger size (10–20 nm) than organic small molecules owing to their core/shell structure, but they usually contain toxic elements such as Cd and Te. NIR lanthanide complexes (Er, Nd, Yb, etc.) have unique atom spectral characteristics and very long luminescence lifetimes (ms) but usually show relatively low quantum efficiencies owing to the parity-forbidden f-f transition (Bao et al., 2021; Zhang et al., 2018a).

In comparison, transition metal (Ir, Pt, etc.) complexes have demonstrated many desired properties for bio-imaging in terms of large Stokes shift, relatively long luminescence lifetime (μs), and high photostability. The large Stokes shift makes it easy to distinguish excitation and emission light to reduce the self-absorption process; meanwhile, the long lifetime allows the use of time-resolved techniques to eliminate background autofluorescence and even realize wash-free live cell imaging. It is worthy to note that mono-cationic iridium(III) complexes show superior permeability of cell membranes to the neutral counterparts because of their good solubility in aqueous solution and the potential-driven preferential uptake of cations (Ho et al., 2020; Lo, 2015; Zhen et al., 2021).

In the reported literatures, the NIR probes based on Ir(III) complexes were developed since 2014 (Zhang et al., 2014). At the primary stage, certain cyclometalated ligands were employed to anchor the emission in the NIR region and provide appropriate emission efficiency. Besides, neutral ancillary ligands were used to form cationic-type complexes, which could ensure the essential solubility in aqueous solution and permeability of cell membranes. The bio-imaging experiments were performed based on distinct optical properties of the probes, such as emission wavelength and intensity (Jin et al., 2017; Liu et al., 2017; Zhang et al., 2014), emission quenching by oxygen (Wang et al., 2017b; Yoshihara et al., 2015; Zheng et al., 2015), exclusive staining in the cytoplasm (Wang et al., 2017b; Zhang et al., 2014), and enriching in mitochondria (Jin et al., 2017; Liu et al., 2017; Yoshihara et al., 2015). At the current stage, the peripheral substitutions were introduced to monitor a specific biochemical reaction process. Before and after the reactions, the emission properties of the probes changed by a wide margin, in terms of emission wavelength, emission intensity or emission lifetime. With the help of these changes, not limited to bio-imaging, qualitative or even semi-quantitative analyses have been realized to detect certain species of particles or structural units, such as proton (H^+) (Zheng et al., 2017), cysteine (Cys) and homocysteine (Hcy) (Li et al., 2020; Wu et al., 2017), peroxynitrite ($ONOO^-$) (Li et al., 2019; Wu et al., 2020), l-azidohomoalanine (Wang et al., 2017a), human carboxylesterase 2 (hCE2) (Yan et al., 2018), and phase-separated biomolecular condensates (Yan et al., 2021).

In this section, we mainly described some representative NIR probes based on Ir(III) complexes reported over the last 5 years, highlighting peripheral substitutions and the resulting response to specific substances or reactions. Similar with the development of NIR Ir(III) complexes used in OLEDs, it is all about the
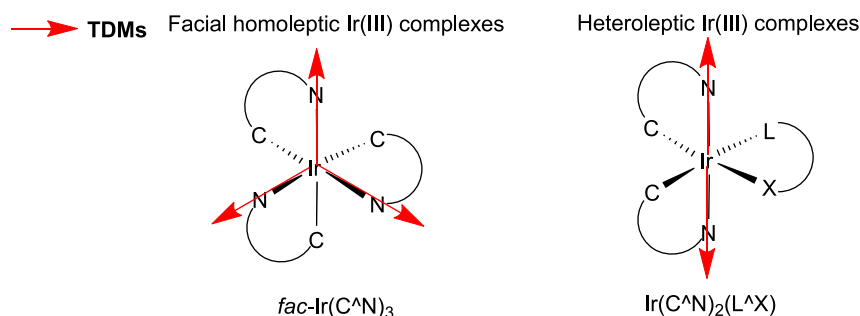
Figure 17. Schematic illustration of facial homoleptic Ir complexes and heteroleptic Ir complexes along with triplet transition dipole moments

relationship between structure and property. We still focused on the molecular construction and photophysical properties of these probes.

Examples of Ir(III) complexes for intensity-based NIR probes

In 2017, Jiang et al. reported a neutral Ir(III) complex with an acid-responsive imine group denoted as the precursor in Figure 19A (Zheng et al., 2017). The PEG chain is used to provide water solubility for the neutral complex. The 2-Benzo[*b*]thien-2-yl-pyridine (btp) is the dominate ligand for the red/NIR emission, because it provides lower π* and higher π than ppy. With the decrease of pH value, the moderate electron-deficient imine group in the precursor is hydrolyzed and converted to more electron-deficient aldehyde group in the reporter with stabilized LUMO energy. Consequently, the red emission at 610 nm from the precursor decreases gradually, and the NIR emission at 705 nm from the reporter emerges concomitantly. When excited at 450 nm, the ratio between the emission intensities of the precursor at 610 nm and the reporter at 705 nm decreased sharply as pH decreased in the range of 7.4–6.8 (Figure 19B), and the conversion was completed within ~6 min (Figure 19C), suggesting an efficient and fast conversion of the precursor into the reporter taking place under mildly acidic pH. In addition, when excited at 580 nm and at pH 6.8, only the 705-nm emission peak can be detected (Figure 19D). In contrast, when excited at 580 nm at pH 7.4, no emission at 705 nm can be measured. This suggests that the reporter signal can be "switched on" by acidic conditions. In hypoxia environment, with little oxygen as triplet exciton quencher, the NIR emission was significantly enhanced. Once switched on at 705 nm, the emission intensity of the reporter was highly sensitive to changes in oxygen level, especially within the physiological range 0%–20% O_2 (Figure 19E). The signal intensity under the extremely hypoxic condition of 0% O_2 was about an order of magnitude higher than that under the normal condition of 20% O_2 (Figure 19F). As shown in Figure 19A, when extravasating from a blood vessel in the acidic tumor microenvironment, the precursor gets converted to the reporter, with a concomitant peak emission wavelength shift to the NIR range. When subsequently exposed to hypoxia, the NIR emission of the reporter is switched "ON," which leads to enhanced signal intensity, i.e., signal amplification. Under hypoxic yet not acidic conditions, the probe remains in its primary form (precursor), with an enhanced emission peak at 610 nm (Figure 19G). Hence, the precursor should remain "silent" (no emission at 705 nm) in blood and in normal tissues yet become activated (with NIR emission at 705 nm switching on) under the acidic conditions of tumors by converting to the reporter. Of importance, the intensity of the emission signal at 705 nm is inversely proportional to tissue oxygenation.

In 2017, Fan et al. reported another Ir(III) complex (NIR-Ir) with an aldehyde group on the main C^N ligands btq as a Cys/Hcy chemosensor (Figure 20A) (Wu et al., 2017). The aldehyde groups on btp are quenchers for phosphorescent emission. After a cyclization reaction with aminoalkyl thiol groups like acetal reaction, the aldehyde groups converted to aliphatic rings and thus significantly enhanced the emission band from 625 to 800 nm (Excitation: 495 nm, Figure 20B). The emission intensities of NIR-Ir (5 mM) with different concentrations of Cys/Hcy show a linear correlation in the range of 10–90 equiv. of Cys/Hcy (Figure 20C). The linear regression equation is $I = 1.37C_{Cys} + 124.52$ (unit of C is mM, R = 0.984) for Cys and $I = 1.94C_{Hcy} + 147.66$ (unit of C is mM, R = 0.985) for Hcy, respectively. The detection limit is calculated to be 13.7 mM for Cys and 9.7 mM for Hcy (S/N = 3), respectively. All interference amino acids did not produce detectable spectral changes (Figure 20D, black bars), indicating that the formation of thiazolidine and thiazinane was a key for the selective recognition of Cys and Hcy. After the addition of 80 equiv. of Cys/Hcy to the above mixture,
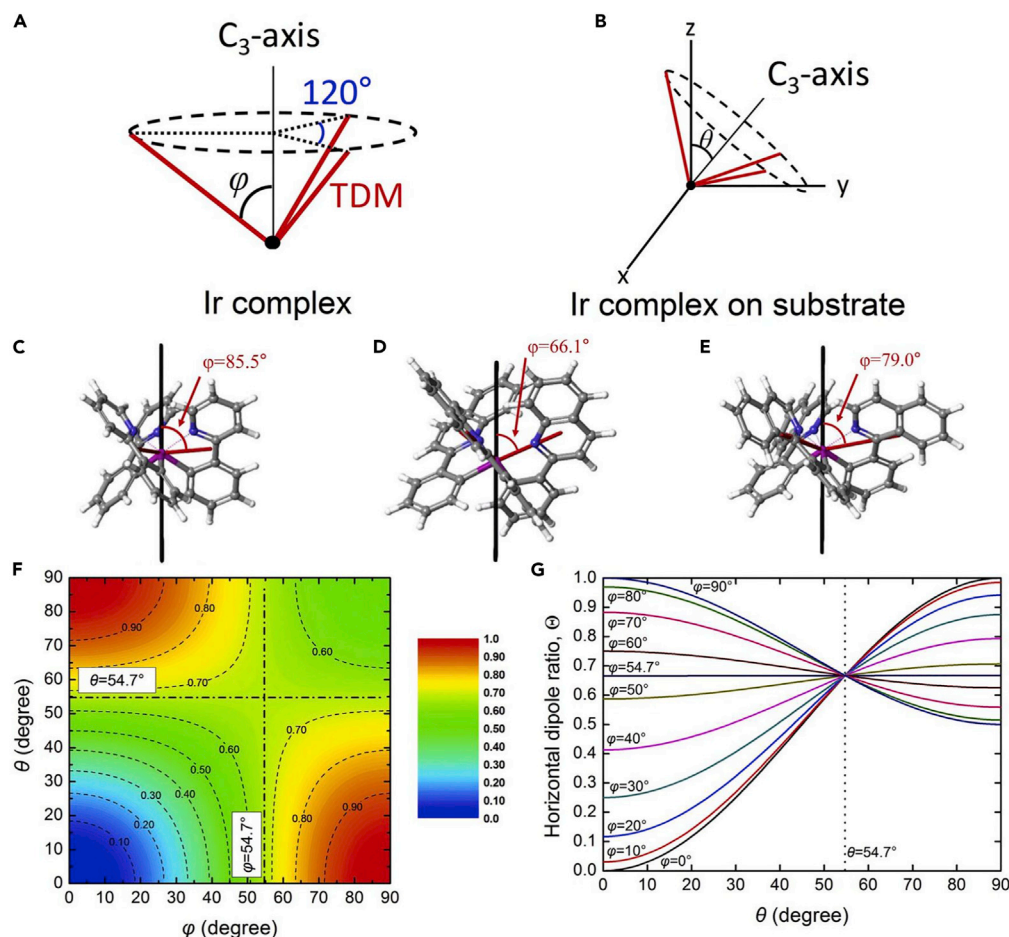
Figure 18. Emitting dipole orientation and molecular orientation of homoleptic Ir(III) complexes
(A) ϕ is the angle between the TDM and the C_3 axis.
(B) θ is the polar angle of the C_3 axis.
(C) Optimized geometries of Ir(ppy)$_3$ and its ϕ angle.
(D) Optimized geometries of Ir(pq)$_3$ and its ϕ angle.
(E) Optimized geometries of Ir(piq)$_3$ and its ϕ angle.
(F) Contour plot of the horizontal dipole ratio of the homoleptic Ir(III) complexes as a function of ϕ and θ.
(G) Theoretical plot of the horizontal dipole ratio as a function of θ, with ϕ as a parameter.
(Huh et al., 2020) Copyright 2020 Elsevier B.V.

the phosphorescence intensity significantly increased (Figure 20D, blue and red bars). This competition experiment demonstrated that other elementary amino acids do not interfere with NIR-Ir phosphorescent detection of Cys/Hcy.

Later in 2020, Fan et al. reported another complex FNO1 with two α,β-unsaturated ketone groups attached to the ancillary ligand ppy as shown in Figure 21A (Li et al., 2020). Although being separated in space by double bonds, the carbonyl groups still conjugated with the ancillary ligand and served as quenchers for phosphorescent emission. After nucleophilic addition reaction like Michael addition reaction with aminothiols, the conjugation was broken, so the intensity of NIR emission band from 640 to 800 nm was increased significantly (Excitation: 500 nm, Figure 21B). After Cys/Hcy was added, the emission intensity increased to 44/52 fold, and two main emission peaks appeared at 683 and 748 nm. The PLQY of FNO1 increased from 0.005 to 0.109/0.122, indicating the off-on property. The emission intensity shows a linear correlation with both Cys and Hcy concentrations ranging from 0 to 80 µM (Figure 21C). The Cys- and Hcy-detection limits of FNO1 were as low as 0.228 and 0.134 µM. As illustrated in Figure 21D, all interference molecules at concentrations as high as 20 equivalents did not cause observable changes, suggesting that FNO1 is highly
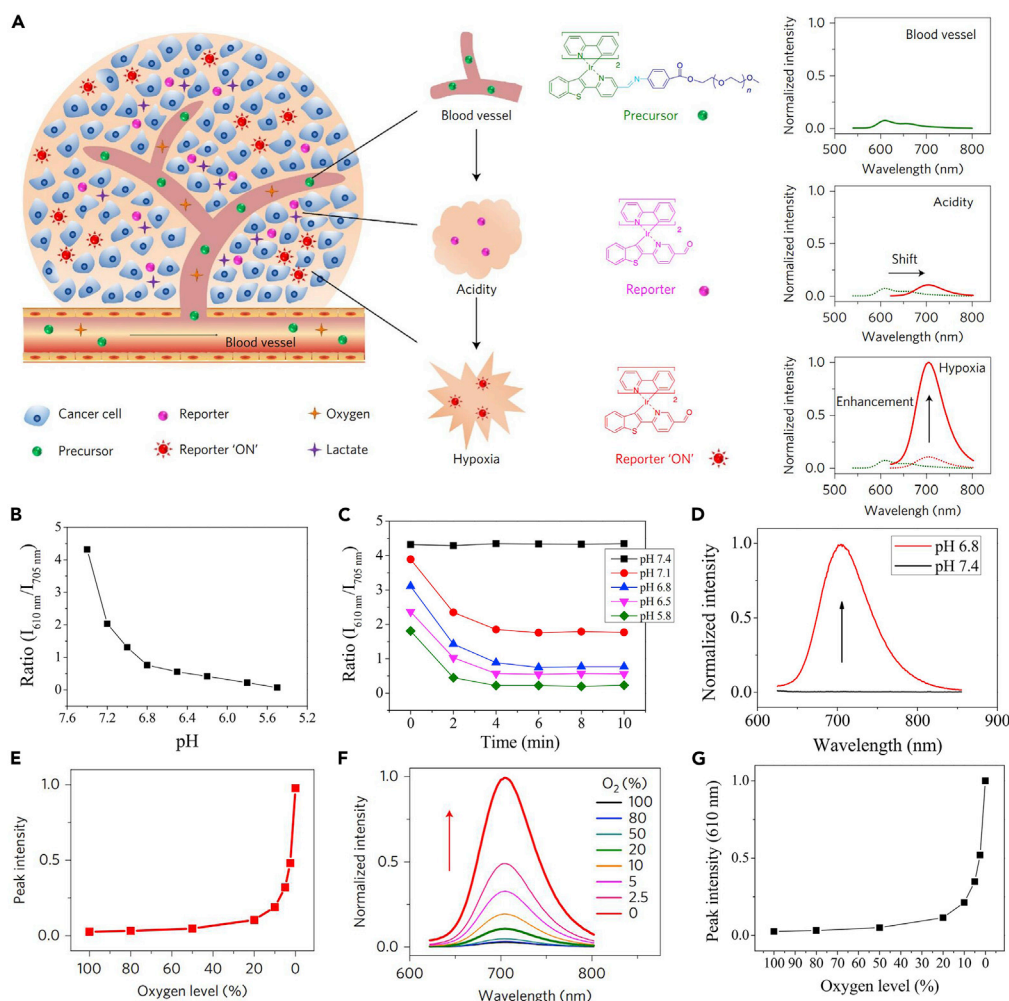
Figure 19. NIR probes based on Ir(III) complexes imaging acidity and hypoxia

(A) Chemical structures and their emission spectra of the precursor and reporter detecting acidity and hypoxia.

(B) The ratio between the emission intensities of the probe at 610 nm and 705 nm at different pH conditions. λ_{ex} = 450 nm.

(C) The kinetics of the conversion from the precursor to the reporter under different pH conditions. λ_{ex} = 450 nm.

(D) The emission spectra of the probe at pH 7.4 and 6.8. λ_{ex} = 580 nm.

(E) Emission intensities of the reporter at 705 nm at various oxygen levels. λ_{ex} = 580 nm.

(F) Emission spectra of the reporter at several oxygen levels. λ_{ex} = 580 nm.

(G) The increase of emission intensity of the precursor at the 610 nm peak with the decrease of oxygen level. λ_{ex} = 410 nm. The intensity of the 610 nm peak at 0% O_2 is about 8.7-fold higher than that at 20% O_2.

(Zheng et al., 2017). Copyright 2017, Macmillan Publishers Limited, part of Springer Nature.

selective to thiol-containing amino acids. Of note, the FNO1 probe showed enhanced sensitivity with respect to the above NIR-Ir probe.

In 2019, Fan et al. reported a cationic Ir(III) complex FNO2 based on btq as the cyclometalated ligands for specific peroxynitrite (ONOO⁻) detection (Figure 22A) (Li et al., 2019). The nitro groups on the 2,4-dinitroaniline of the ancillary ligand are quenchers for phosphorescent emission. After the reaction with ONOO⁻, the amide was hydrolyzed; thus, the intensity of emission band between 600 and 850 nm (Excitation: 500 nm) of the probe was increased (Figure 22B); hence, it acted as an off-on switch in response to ONOO⁻. After ONOO⁻ was added, the emission intensity was increased by up to 12-fold, and two main emission peaks appeared at 660 and 710 nm (Figure 22B). Besides, the PLQY of FNO2 was largely increased from 0.012 to 0.131. The titration experiments revealed that the intensity became saturated at 110 mM ONOO⁻ and a linear correlation between the emission intensity and ONOO⁻ concentration was obtained from 0 to
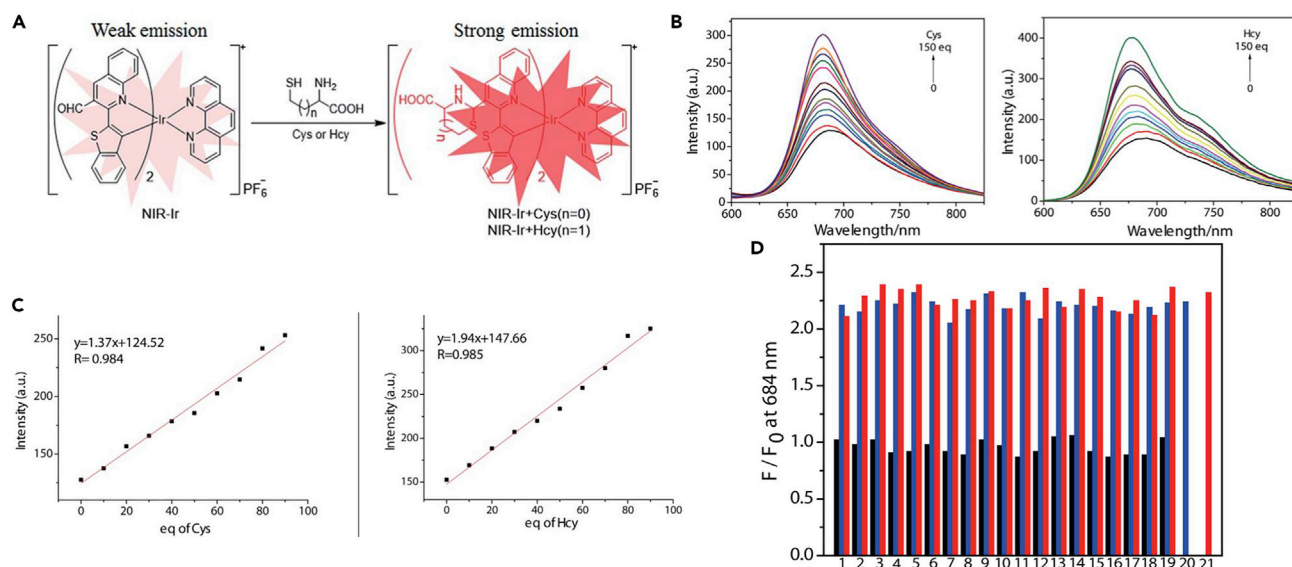
Figure 20. NIR probe NIR-Ir detecting Cys and Hcy

(A) Chemical structure of NIR-Ir probe and its reactions with Cys and Hcy.

(B) Changes in emission spectra of NIR-Ir probe upon addition of various amounts of Cys or Hcy.

(C) Plots of emission intensity versus various amounts of Cys/Hcy (0–90 equiv), λ_{ex} = 495 nm, λ_{em} = 684 nm.

(D) Luminescent responses of NIR-Ir (10 mM) in DMSO-HEPES (4:1 v/v) to various amino acids (80 equiv.) at 37°C. Bars represent the ratio F/F_0 of luminescence intensity at 670 nm, λ_{ex} = 495 nm. Black bars represent the addition of 80-fold various amino acids to a 10 mM solution of NIR-Ir. Blue and red bars represent the addition of Cys and Hcy (80 equiv.) to the above solution, respectively. (1) Gly; (2) Glu; (3) Gln; (4) GSH; (5) Met; (6) Arg; (7) Tyr; (8) Ala; (9) Lys; (10) Leu; (11) Pro; (12) Try; (13) Ser; (14) Thr; (15) Asp; (16) Asn; (17) Val; (18) Ile; (19) His; (20) Cys; (21) Hcy. (Wu et al., 2017), Copyright 2017 The Royal Society of Chemistry.

80 mM (Figure 22C). The detection limit of FNO2 was as low as 0.663 mM. The selective response of FNO2 toward ONOO⁻ was investigated using interference molecules, including reactive oxygen species and reactive nitrogen species. All competing molecules at the concentration of as high as 20 equivalents did not promote observable changes (Figure 22D).

Later in 2020, Chao et al. reported another cationic Ir(III) complex Ir-NIR for specific ONOO⁻ detection, which uses diphenylquinoxaline derivatives as cyclometalated ligands as shown in Figure 23A (Wu et al., 2020). The secondary amine substituted on the ancillary ligand is quencher for phosphorescent emission. Similarly, after the reaction with ONOO⁻, the amine was hydrolyzed, thus the intensity of the emission band between 600 and 850 nm (Excitation: 405 nm) increased (Figure 23B). Upon reaction with increasing concentration (0–1.5 equiv) of ONOO⁻, the emission intensity at 702 nm of Ir-NIR gradually increased approximately 100-fold. The emission intensity reached a saturation level at 5 μM peroxynitrite concentration (Figure 23C). The PLQY increased from 0.009 to 0.128. A linear phosphorescence intensity response toward ONOO⁻ was observed with concentrations ranging from 0 to 5 μM (Figure 23C). The limit of detection for ONOO⁻ was calculated to be around 49.8 nM. Ir-NIR did not exhibit an observable phosphorescence enhancement in the presence of any analyte other than ONOO⁻ (Figure 23D).

Although binuclear Ir(III) complexes were mediocre for pursuing emission efficiency, they might have remarkable performance as probes for bio-imaging. In 2018, Liu et al. reported a binuclear Ir(III) complex C10 as shown in Figure 24A (Liu et al., 2018a), which was designed as a ratiometric probe to monitor the intracellular viscosity change. The complex employed two different C^N ligands. The part with 2-(2,4-difluorophenyl) pyridine ligand for green emission (around 521 nm) and the part with benzothiophene-phenanthridine (btph) ligand for NIR emission (around 708 nm) were connected through a flexible saturated alkyl chain (Excitation: 450 nm). This kind of connection did not bring much influence to the independent emission of each core but could guarantee the ratio of the two was equal, making it a dual-emission ratiometric probe featuring high sensitivity and selectivity for viscosity changes (Figures 24B and 24C). The viscosity was increased from 1.1 (water) to 950 cP (99% glycerol), and the luminescence intensity of C10 was increased 16.9-fold at 521 nm, and 2.5-fold at 711 nm, indicating the 521-nm emission peak is
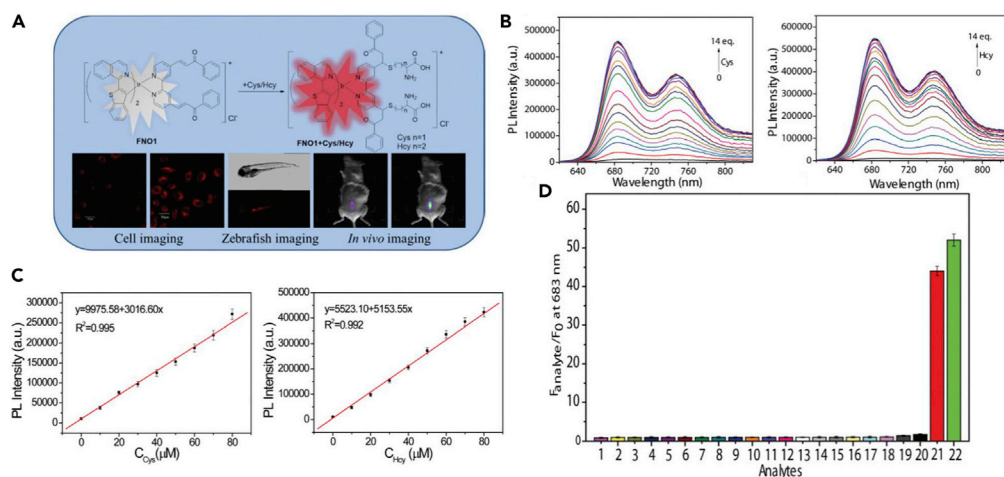
Figure 21. NIR probe FNO1 detecting Cys and Hcy

(A) Chemical structure of FNO1 probe and its sensing mechanism in response to Cys and Hcy.

(B) Changes in emission spectra of FNO1 probe upon addition of various amounts of Cys or Hcy.

(C) Linearity between the luminescence intensity with Cys/Hcy concentration in the range of 0–80 μM, λ_{ex} = 500 nm, λ_{em} = 683 nm.

(D) Responses of FNO1 (10 μM) in DMSO/PBS (pH = 7.4, 1:4 v/v) to 20 eq. of various amino acid analytes at room temperature after 10 min: (1) blank, (2) Ala, (3) Gly, (4) Arg, (5) Phe, (6) Thr, (7) Trp, (8) Gln, (9) Ser, (10) Asn, (11) Leu, (12) Lys, (13) Ile, (14) Pro, (15) Tyr, (16) Glu, (17) Met, (18) Val, (19) His, (20) Asp, (21) Cys, and (22) Hcy. Bars represent the $F_{analyte}/F_0$ ratio of the luminescence intensity at 683 nm, λ_{ex} = 500 nm.

(Li et al., 2020), Copyright 2020 The Royal Society of Chemistry.

more sensitive to viscosity changes of the mixture solvent. The logarithm of the ratiometric emission intensity increase ($\Delta I_{718\ nm}/\Delta I_{521\ nm}$) has a linear fitting relationship (R^2 = 0.967) with the logarithm of the viscosity value (Figure 24C). The interference experiments showed that HSA, calf thymus DNA, and 18 amino acids had less interferences in emission intensity (Figures 24D–24F).

Examples of Ir(III) complexes for lifetime-based NIR probes

Cells are highly complex and organized entities, which consist of various biological events. It is a continual challenge to design ideal probes for real-time imaging of dynamic processes in living cells. Compared with fluorescence intensity imaging mentioned above, fluorescence lifetime imaging (FLIM) is highly sensitive to the molecular structure and the real-time microenvironment of the fluorophore. Currently, FLIM has been widely used as a nondestructive imaging technique for the dynamic detection of the microenvironment in living cells (Berezin and Achilefu, 2010). It has a strong ability to distinguish the reacted and unreacted probes with lifetime shifts. But the lifetimes of commonly used organic dyes may overlap with autofluorescence in cells, so it is imperative to develop bio-orthogonal probes with long lifetimes to eliminate the auto-interference.

We designed and synthesized a novel NIR bioorthogonal probe based on an Iridium-alkyne complex (Figure 25) (Wang et al., 2017a). It shows deep-red to NIR emission covering 600 to 800 nm with maximum emission at 640 nm and a long lifetime of up to 530 ns in Dulbecco's phosphate buffered saline (dPBS) solution, which is beneficial to eliminate autofluorescence interference in biological systems compared with that of traditional organic fluorescent dyes. With a terminal alkyne group, this probe is applicable to the click reaction of copper(I)-catalyzed azide-alkyne cycloaddition (CuAAC). It was found that the lifetime decreased from 530 to 116 ns upon triazole formation by a click reaction with L-azidohomoalanine (AHA) in dPBS buffer (Figure 25A). On gradually changing the ratio of Ir-alkyne and AHA from 1:0 to 1:1, the lifetimes gradually decreased (Figure 25B). The measured decays were fitted, and there was a linear correlation (R^2 = 0.99) between the mean lifetimes and the ratios of Ir-alkyne and AHA (Figure 25C). Such a large lifetime change could provide an effective way to discriminate the reacted iridium-alkyne from the unreacted probes within living cells (Figure 25D). Based on this probe, we exploited photoluminescence lifetime imaging (PLIM) and realized wash-free and dynamic imaging of the newly synthesized proteins in living cells. This probe also
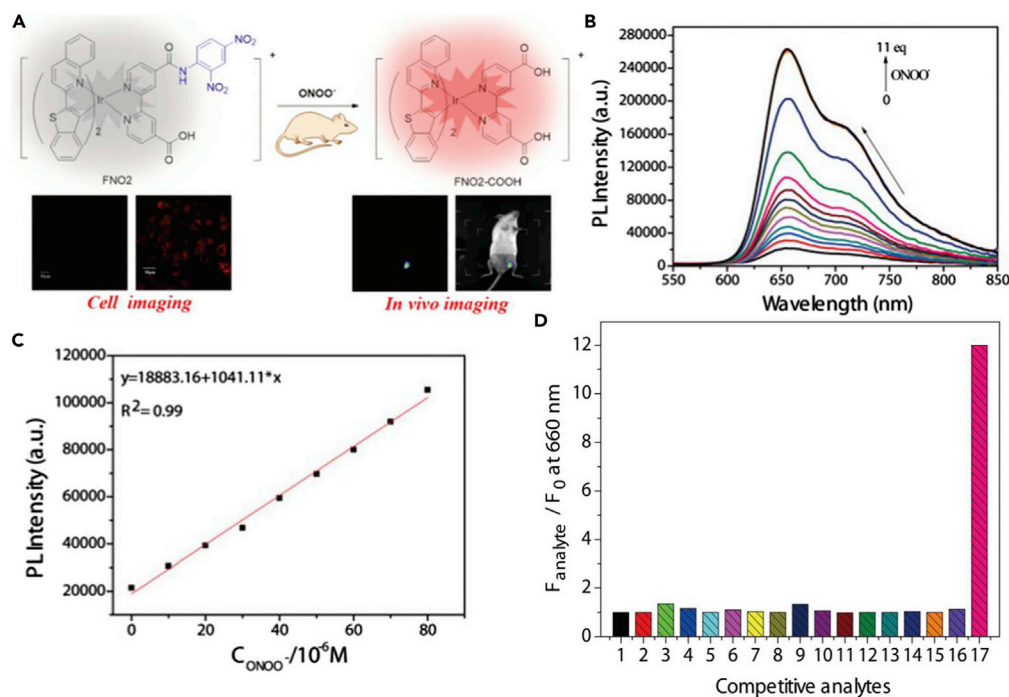
Figure 22. NIR probe FNO2 detecting peroxynitrite

(A) Chemical structure and reaction of the FNO2 probe detecting peroxynitrite *in vitro* and *in vivo*.

(B) Emission spectra of the FNO2 probe (10 μM) upon addition of increasing concentrations of $ONOO^-$ (0–11 equiv., 1 equiv. increased gradually) in DMSO/PBS (pH = 7.4, 1:19 v/v).

(C) Linearity between the luminescence intensity and $ONOO^-$ concentration in the range of 0–80 mM, λ_{ex} = 500 nm, λ_{em} = 660 nm.

(D) Responses of the probe FNO2 (10 mM) in DMSO/PBS (pH = 7.4,1:19 v/v) to 20 equiv. of various competitive analytes at room temperature after 5 min (1) Blank; (2) AIBA; (3) BuOOH; (4) ClO^-; (5) CO; (6) Cys; (7) GSH; (8) H^+; (9) Hcy; (10) H_2O_2; (11) HSO_3^-; (12) NO; (13) NO_2^-; (14) ·OH; (15) OH^-; (16) O_2^-; (17) $ONOO^-$. Bars represent the ratio $F_{analyte}/F_0$ of luminescence intensity at 660 nm, λ_{ex} = 500 nm.

(Li et al., 2019). Copyright 2019 The Royal Society of Chemistry.

offers the benefits of a long Stokes shift, excellent cell penetration, low cytotoxicity, and good resistance to photobleaching. Based on the unique properties of the probe, it is anticipated to have applications for imaging other biological processes within living cells in the near future.

Enzymes are vital to life and are closely related to metabolic activities. Abnormal activities of metabolic enzymes have been correlated with various diseases and even cancer. To date, most fluorescent probes for enzymes can be categorized into two modes, "turn-on" probes and ratiometric probes, both of which are essentially intensity-based probes. Compared with intensity-based probes, the PLIM based on long-lifetime probes has demonstrated the possibility to eliminate the undesirable short-lifetime background autofluorescence in the complicated biological environment. Taking human carboxylesterase 2 (hCE2) as an example, we reported another iridium complex as the first PLIM probe for the detection of metabolic enzymes in living cells (Yan et al., 2018). The probe named Ir-TB (Figure 26A) was designed, synthesized, and systematically studied for selective and quantitative detection of hCE2 both *in vitro* and in living cells. This probe displays deep-red to NIR emission centered at 639 nm. After the hCE2 hydrolysis reaction (Figure 26B), the lifetime of probe increased from 338 to 625 ns. The lifetimes increased as the concentrations of hCE2 increased (Figure 26B). The lifetime enhancement is proportional to the hCE2 concentration and exhibited a good linearity in the range of 0–10 mg mL^{-1} (Figure 26C). With the large lifetime change, the hCE2-hydrolyzed probes can be easily distinguished from those non-hydrolyzed ones via PLIM without washing steps. The selectivity experiments showed that only when treated with hCE2 was the distinct lifetime difference observed (Figure 26D). Inhibitor assays confirmed that the lifetime change was the consequence of the cleavage reaction with hCE2. As shown in Figure 26E, both BNPP (an effective inhibitor for
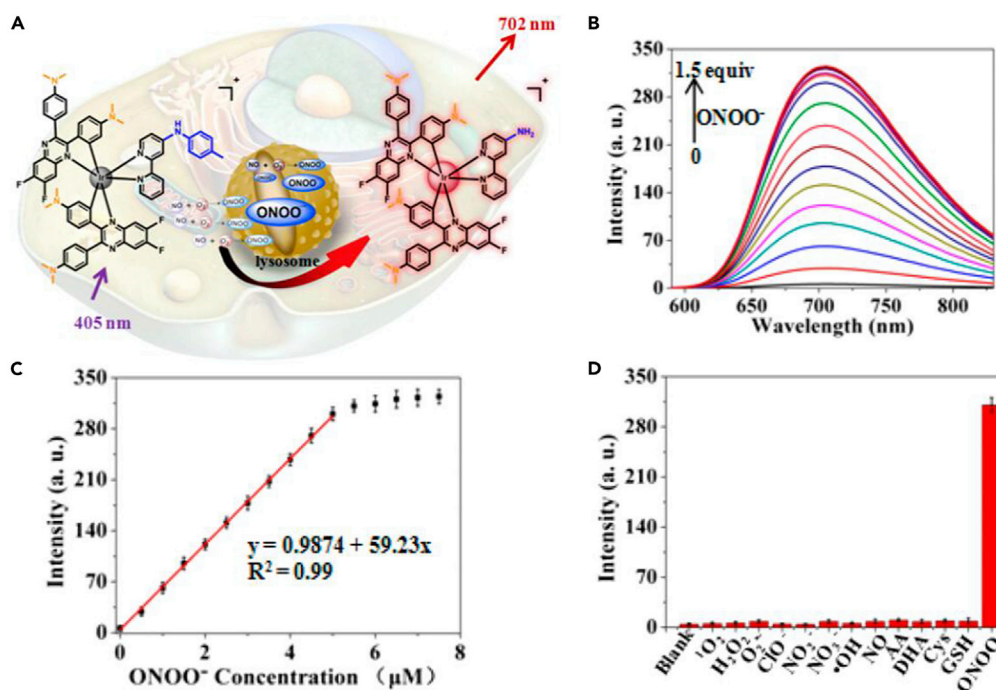
Figure 23. NIR probe Ir-NIR detecting peroxynitrite

(A) Chemical structure and reaction of the Ir-NIR probe detecting peroxynitrite.

(B) Phosphorescence response of Ir-NIR (5 μM) to increasing amounts (0–1.5 equiv) of ONOO$^-$ in PBS (containing 10% DMSO) solution.

(C) The change in the phosphorescent and linear response of Ir-NIR (5 μM) toward ONOO$^-$.

(D) Phosphorescence intensity at 702 nm of Ir-NIR (5 μM) toward 10 equiv various species (blank, $^1O_2$, H_2O_2, $O_2\cdot^-$, ClO$^-$, NO$_2^-$, NO$_3^-$, ·OH, NO, AA (ascorbic acid), DHA (dehydroascorbate), L-Cys (L-cysteine), GSH (glutathione), and ONOO$^-$) for 600 s in PBS solution (λ_{ex} = 405 nm; slits:5/5 nm).

(Wu et al., 2020). Copyright 2020 American Chemical Society.

hCEs) and LPA (a common inhibitor for hCE2) have a significant inhibitory effect on the activity of hCE2, whereas EDTA and HA, inhibitors of other enzymes, show little influence on the activities of hCE2. In addition, small molecules (amino acids and bio-molecules) (Figure 26F) and metal ions (Figure 26G) had little influence on the lifetime change of Ir-TB. Besides, there is minimum interference of pH and viscosity for the detection of hCE2 using Ir-TB. The PLIM images demonstrated Ir-TB realized the detection and imaging of hCE2 activities in living cells (Figure 26H).

The PL lifetime changes of these probes are the basis for PLIM. In the case of Ir-alkyne, the lifetime reduced from 530 to 116 ns upon triazole formation by click reaction with AHA in dPBS buffer. Sharp change of 414 ns for the measured lifetime is mainly due to the structural change after click reaction. Theoretical studies show that the MLCT percentage of the reacted probes (40.3%) was slightly higher than that of the unreacted ones (39.5%), which would accelerate k_r. The more delocalized LUMO of the reacted probes could increase its interaction with surrounding molecules and increase the risk of quenching, thus accelerating k_{nr}. Consequently, the shortened decay lifetime of the probe upon triazole formation could be anticipated (Wang et al., 2017a). As for the case of Ir-TB, the shortened substitute of the iridium complex after hydrolysis would help to decrease non-radiative decay pathways arising from the intramolecular large motion of vibrational, torsional, and librational modes. Therefore, the prolonged decay lifetime of the probe upon hCE2 hydrolysis could be anticipated (Yan et al., 2018).

Membraneless organelles are assembled by proteins and nucleic acids through a process termed liquid-liquid phase separation (LLPS). Monitoring the formation of biomolecular condensates driven by LLPS is very challenging. Cationic iridium complexes as bioimaging probes for PLIM have shown advantages of red emission, large Stokes shift, and excellent cell permeability. Its nearly microsecond scale lifetime helps to avoid the cell autofluorescence. Most recently, we designed and synthesized an iridium complex-based
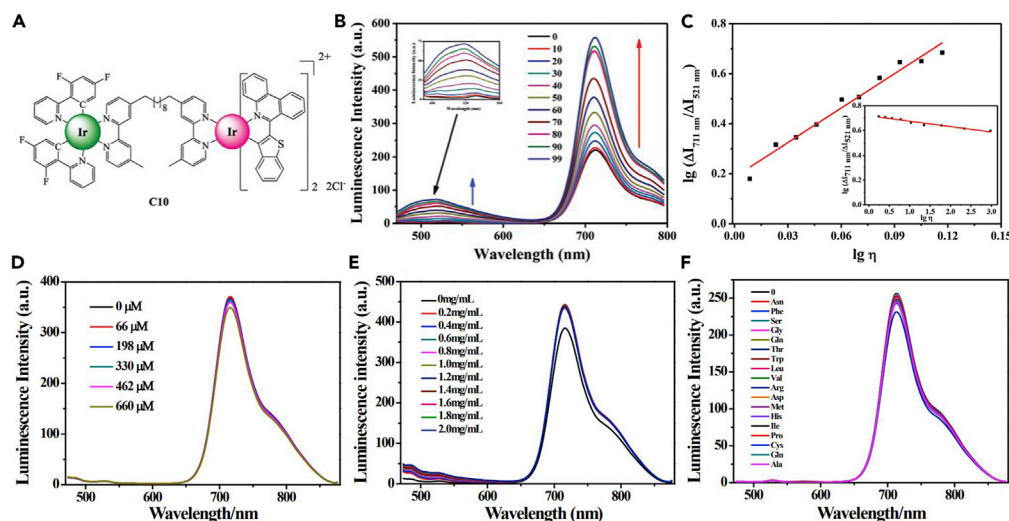
Figure 24. NIR ratiometric probe C10 based on binuclear Ir(III) complex
(A) Structure of probe C10.
(B) Emission spectra of C10 (10 μM) in mixed glycerol-water solvents, λ_{ex} = 450 nm.
(C) The linearity of $lg(\Delta I_{718\ nm}/\Delta I_{521\ nm})$ versus $lg\eta$ plot.
(D–F) (D), (E), and (F) Emission spectra of probe C10 (10 μM) in PBS buffer (0.1 M, pH = 7.40) upon titration of ct-DNA solution (D), upon titration of HSA solution (E), and with addition of 18 kinds of amino acids (100 μM) (F). λ_{ex} = 450 nm (Liu et al., 2018a). Copyright 2018 The Royal Society of Chemistry.

probe (Ir-OMe, Figure 27A) for PLIM by incorporating a free-rotating methoxy group (OMe), which may lead to lifetime changes according to different environmental viscosity (Yan et al., 2021). The probe shows moderate emission from 550 to 800 nm as depicted in Figure 27B. The photoluminescence lifetime shows a proportional increase with the increased ratio of glycerol. When the proportion of glycerol is 0% (1.45 cP), the lifetime of Ir-OMe is 163.39 ns. Then, the lifetime of Ir-OMe gradually increases with the rise of the proportion of glycerol, as demonstrated by the lifetime decay curves in Figure 27C. When the proportion of glycerol reaches 85% (165.47 cP), the lifetime is 1,023.90 ns. The 6.3-fold increase of the Ir-OMe lifetime and the good linearity (Figure 27D) make it ideal for a high-sensitivity detection of viscosity, thus benefiting the monitoring inside phase separation condensates. The radiative rate of Ir-OMe remains stable as the viscosity of solution increases, while the nonradiative rate decreases significantly, which means it is sensitive to viscosity. The reason is that the increase of viscosity would limit the free rotation of the methoxyl group in the molecule and decrease the possibilities of collision and quenching among molecules, which could reduce the non-radiation rate, thus increasing the lifetime. Taking Ir-OMe as probe, we used PLIM to achieve in situ and dynamic monitoring of phase-separated biomolecular condensates in living cells (Figure 27E). The high throughput of PLIM makes it possible to analyze hundreds of phase-separated condensates at the same time, and high spatiotemporal resolution makes it easy to differentiate 1-μm-diameter area of a single condensate in less than 1 min.

PERSPECTIVE AND OUTLOOK

Since 2006, the research on NIR-emitting Ir(III) complexes has gone through a journey of 15 years, from being little noticed with very few reports in early years to being lively growing, especially in the past three years. Nevertheless, the potential of NIR Ir(III) complexes was not yet fully paid back compared with their great success in the visible region for commercialized OLEDs products. Although one cannot say what an "all-round player" these are, their relatively comprehensive properties are very attracting and highly desirable for practical applications in various fields.

The expression of "NIR-emitting Ir(III) complex" emphasizes its NIR emission, but first of all it is a kind of Ir(III) complex. The golden age of phosphorescent Ir(III) complexes in the visible region left us with a lot of fortune, especially the robust red emitters, which have been proved to be the perfect starting point of new derivations for NIR-emitting ones. The fundamental theories are always valuable to evaluate new
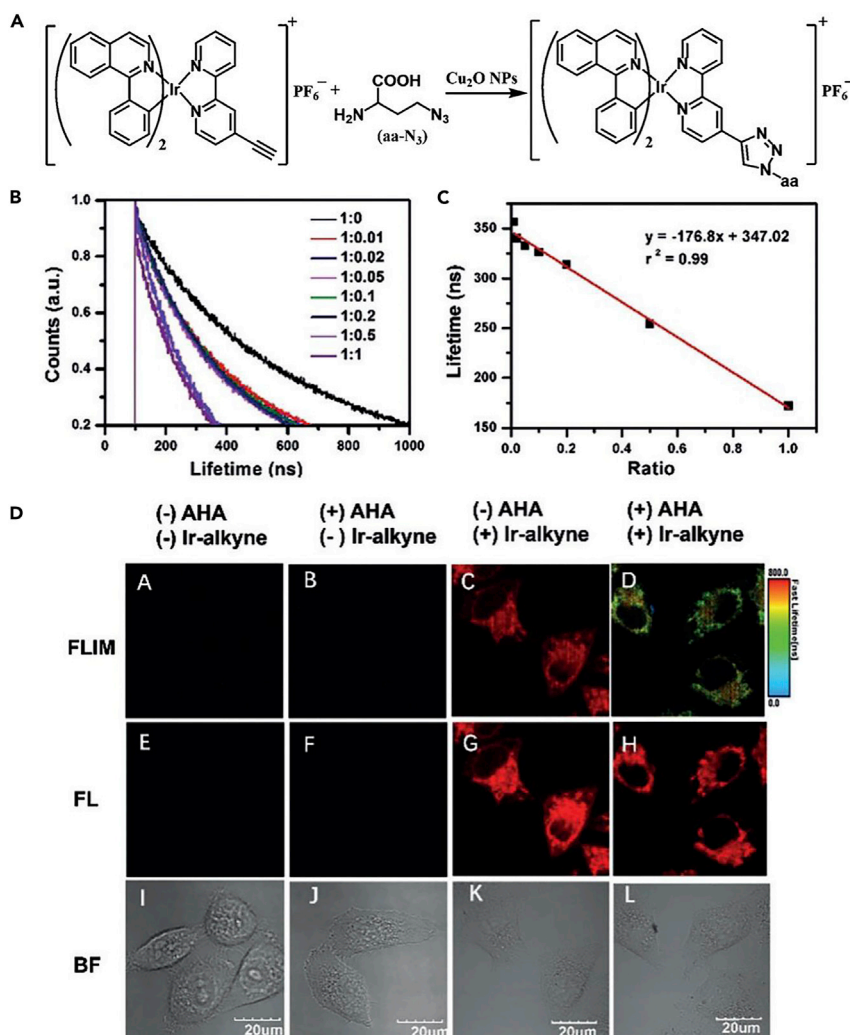
Figure 25. Lifetime-based NIR probes Ir-alkyne

(A) The chemical structure and click reaction of Ir-alkyne probe.

(B) The lifetime decay curve of Ir-alkyne reacted with different ratios of AHA from 1:0 to 1:1.

(C) The fitted curve of the lifetimes versus Ir-alkyne and AHA ratio.

(D) Cell labeling with Ir-alkyne probes. The FLIM images were collected from the emission through a λ = 561 nm long-pass filter upon excitation at λ = 441 nm.

(Wang et al., 2017a) Copyright 2017, Wiley-VCH.

molecular designs before synthesis and provide feasible strategies to squeeze out every drop of potential efficiency. The current success of red-emitting Ir(III) complexes has been made by overall reform on all the parts of the ligands including the C^N ligands, ancillary ligands, and peripheral substitutions, which is of great referential significance for the development of NIR-emitting Ir(III) complexes. For red-emitting Ir(III) complexes, the C^N ligands have been almost fully investigated and the typical ones are usually based on three aromatic rings and one heteroatom, such as piq and pq. But it is totally different for NIR-emitting Ir(III) complexes, which usually require more aromatic rings and heteroatoms for enough redshift into NIR emission. Meanwhile, the bulkier C^N ligands with a higher degree of conjugation might bring more problems, such as poor solubility, poor sublimation ability, and harmful intermolecular aggregation. These problems in turn provide much more room for structure modifications to solve them, making the construction of an appropriate C^N ligand more complicated for NIR emissions.

When things becoming more complicated with more variables, it would be very slow to make progress empirically. Fortunately, the quantum chemical calculation has made great progress on providing high-
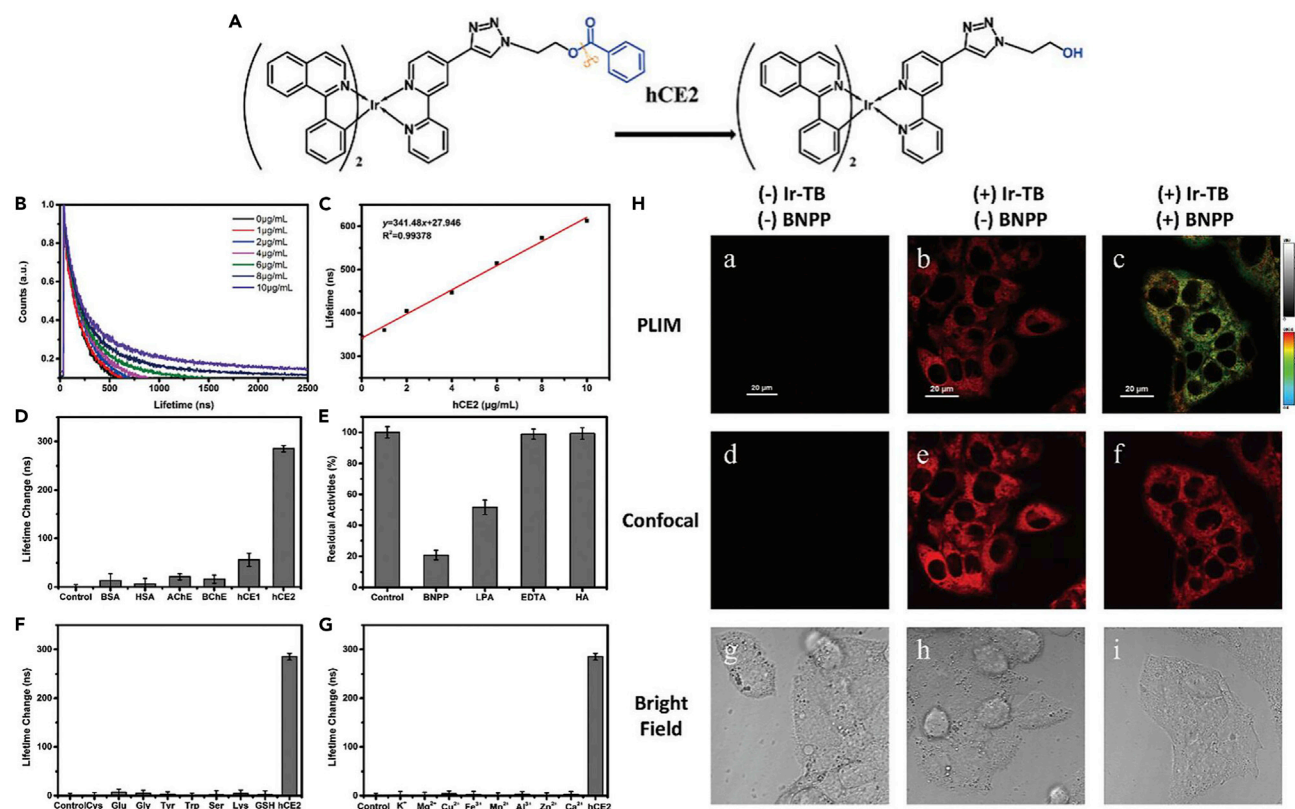
Figure 26. Lifetime-based NIR probes Ir-TB

(A) The chemical structure and hCE2 hydrolysis reaction of Ir-TB probe.

(B) The lifetime decay curves of Ir-TB upon reaction with different concentrations of hCE2.

(C) The fitted curve of lifetime to different concentrations of hCE2.

(D) The photoluminescence lifetime response of Ir-TB (10 μM) toward various species of enzymes.

(E) Inhibitory effects of various specific inhibitors of human esterases on Ir-TB (10 μM).

(F) The photoluminescence lifetime response of Ir-TB (10 μM) toward various species of amino acids and bio-molecules.

(G) The photoluminescence lifetime response of Ir-TB (10 μM) toward various species of metal ions.

(H) Confocal images and photoluminescence lifetime images of HepG2 cells. The PLIM images were collected from the emission through a 561-nm long-pass filter upon excitation at 441 nm.

(Yan et al., 2018) Copyright 2018, The Royal Society of Chemistry.

throughput screening and reference value for the development of new emitters. In most cases, quantum chemical calculations are workable in predicting exciton energies and localizations of FMOs. The difficulty is to establish clear and solid correlation between calculation results and photophysical properties from experiments, which requires more reliable parameters. The ultimate target is the reliable prediction of k_r and k_{nr}, and one more step further is the determinate relationship between structure modifications and their influences to PLQY. There have been some calculation reports trying to predict k_r and k_{nr} and analyze the relationship between structure and property. But for NIR-emitting Ir(III) complexes, there is still a long way to go.

Once the promising molecules are screened out by calculations, the next possible difficulty is the efficient synthesis of the corresponding ligands and final complexes. It does not mean that the synthesis itself is as hard as a total synthesis of a natural organic molecule. But considering the time consumption of the whole workflow of developing a new NIR Ir(III) emitter, the synthesis is often asked to be the minor part. So the reactions of ligand/complex synthesis are expected to be in one or two steps to minimize the time consumption. This condition will limit the further development of more varied ligands and complexes. Based on this point, two suggestions are given here. One is seeking more available starting reagents and reactions. Better starting reagents and better reactions can greatly improve the efficiency of synthesis and
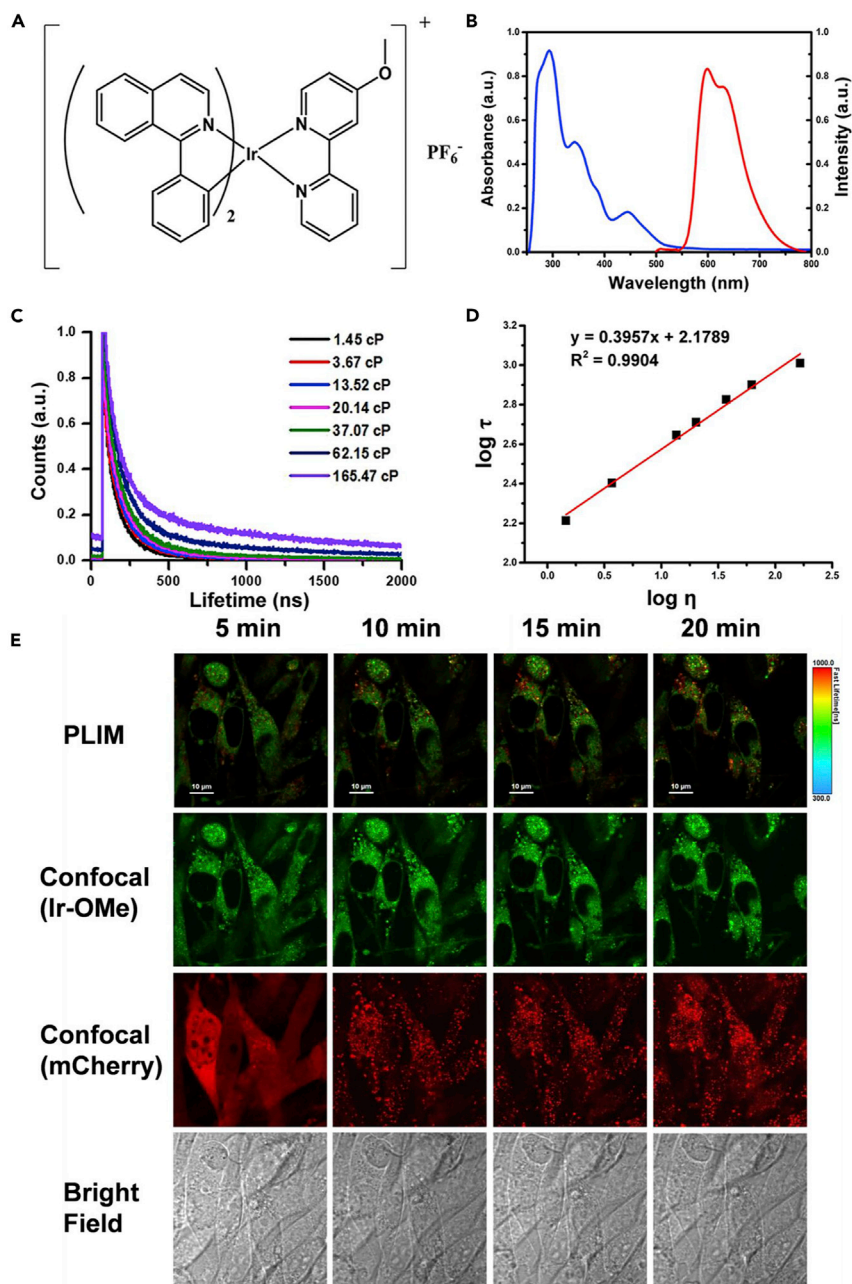
Figure 27. Lifetime-based NIR probe Ir-OMe

(A) Molecular structure of Ir-OMe.

(B) Absorption and emission spectra of Ir-OMe.

(C) Photoluminescence lifetime decay curves of Ir-OMe in glycerol/PBS solution; the proportions of glycerol are 0%, 30%, 45%, 60%, 70%, 75%, and 85%, respectively.

(D) Fitted curve of the lifetime (log τ) to viscosity (log η).

(E) Confocal and PLIM images of light-induced opto-FUS phase separation process from the start to 20 min.

(Yan et al., 2021) Copyright 2021 American Chemical Society.

shorten the workflow of synthesis. The golden age of synthesis of heterocycles and visible-emitting Ir(III) complexes has given birth to many valuable reactions, which could be employed for the synthesis of NIR Ir(III) emitter. The other one is seeking possible cooperation with other researchers. It is not only limited to the synthesis.

When the desired NIR material is successfully obtained, the application is not necessarily limited to OLEDs. It does not have to be a total substitute for a certain material. It can be a supplement and even open up new applications, which require close multidisciplinary collaborations. For example, collaborating with the experts in organic photovoltaic devices (OPVs), we studied the voltage losses in OPVs based on NIR Ir complexes and $PC_{71}BM$ (Jin et al., 2019a) and summarized limitations and perspectives on triplet-material-based OPVs (Jin et al., 2019b). Most importantly, the intrinsic flexibility makes NIR organic materials adapt different substrates, in particular for flexible and wearable devices, such as wearable/implantable NIR light biomedical tools that involve conformal contact with human skin (Zhang and Rogers, 2019), softer skin-like electronics in a space-limited device (Ma et al., 2020). It is anticipated that novel NIR-emitting iridium complexes will inject new vitality into NIR organic materials for diverse advanced applications in flexible and wearable organic optoelectronic devices, biological imaging, and other fields.

AUTHOR CONTRIBUTIONS

Framework, Y. Z. and J. Q.; writing - original draft, Y. Z.; writing - review & editing, Y. Z. and J. Q.; supervision, J. Q.

DECLARATION OF INTERESTS

The authors declare no competing interests.

REFERENCES

Ai, X., Evans, E.W., Dong, S., Gillett, A.J., Guo, H., Chen, Y., Hele, T.J.H., Friend, R.H., and Li, F. (2018). Efficient radical-based light-emitting diodes with doublet emission. Nature *563*, 536–540. https://doi.org/10.1038/s41586-018-0695-9.

Antaris, A.L., Chen, H., Cheng, K., Sun, Y., Hong, G., Qu, C., Diao, S., Deng, Z., Hu, X., Zhang, B., et al. (2016). A small-molecule dye for NIR-II imaging. Nat. Mater. *15*, 235–242. https://doi.org/10.1038/nmat4476.

Azumi, T., and Miki, H. (1997). Spectroscopy of the spin sublevels of transition metal complexes. In Electronic and Vibronic Spectra of Transition Metal Complexes II, H. Yersin, ed. (Springer Berlin Heidelberg), pp. 1–40. https://doi.org/10.1007/BFb0119209.

Baek, S., Kwak, S.-Y., Kim, S.-T., Hwang, K.Y., Koo, H., Son, W.-J., Choi, B., Kim, S., Choi, H., and Baik, M.-H. (2020). Ancillary ligand increases the efficiency of heteroleptic Ir-based triplet emitters in OLED devices. Nat. Commun. *11*, 2292. https://doi.org/10.1038/s41467-020-16091-1.

Baldo, M.A., Lamansky, S., Burrows, P.E., Thompson, M.E., and Forrest, S.R. (1999). Very high-efficiency green organic light-emitting devices based on electrophosphorescence. Appl. Phys. Lett. *75*, 4–6. https://doi.org/10.1063/1.124258.

Baldo, M.A., Adachi, C., and Forrest, S.R. (2000). Transient analysis of organic electrophosphorescence. II. Transient analysis of triplet-triplet annihilation. Phys. Rev. B *62*, 10967–10977. https://doi.org/10.1103/PhysRevB.62.10967.

Bao, G., Wen, S., Lin, G., Yuan, J., Lin, J., Wong, K.-L., Bünzli, J.-C.G., and Jin, D. (2021). Learning

from lanthanide complexes: the development of dye-lanthanide nanoparticles and their biomedical applications. Coord. Chem. Rev. *429*, 213642. https://doi.org/10.1016/j.ccr.2020.213642.

Berezin, M.Y., and Achilefu, S. (2010). Fluorescence lifetime measurements and biological imaging. Chem. Rev. *110*, 2641–2684. https://doi.org/10.1021/cr900343z.

Cao, X., Miao, J., Zhu, M., Zhong, C., Yang, C., Wu, H., Qin, J., and Cao, Y. (2015). Near-infrared polymer light-emitting diodes with high efficiency and low efficiency roll-off by using solution-processed iridium(III) phosphors. Chem. Mater. *27*, 96–104. https://doi.org/10.1021/cm503361j.

Cao, Y., Wang, N., Tian, H., Guo, J., Wei, Y., Chen, H., Miao, Y., Zou, W., Pan, K., He, Y., et al. (2018). Perovskite light-emitting diodes based on spontaneously formed submicrometre-scale structures. Nature *562*, 249–253. https://doi.org/10.1038/s41586-018-0576-2.

Di Censo, D., Fantacci, S., De Angelis, F., Klein, C., Evans, N., Kalyanasundaram, K., Bolink, H.J., Grätzel, M., and Nazeeruddin, M.K. (2008). Synthesis, characterization, and DFT/TD-DFT calculations of highly phosphorescent blue light-emitting anionic iridium complexes. Inorg. Chem. *47*, 980–989. https://doi.org/10.1021/ic701814h.

Chen, Z., Wang, L., Ho, C.-L., Chen, S., Suramitr, S., Plucksacholatarn, A., Zhu, N., Hannongbua, S., and Wong, W.-Y. (2018). Smart design on the cyclometalated ligands of iridium(III) complexes for facile tuning of phosphorescence color spanning from deep-blue to near-infrared. Adv. Opt. Mater. *6*, 1800824. https://doi.org/10.1002/adom.201800824.

Chen, Z., Zhang, H., Wen, D., Wu, W., Zeng, Q., Chen, S., and Wong, W.-Y. (2020). A simple and efficient approach toward deep-red to near-infrared-emitting iridium(III) complexes for organic light-emitting diodes with external quantum efficiencies of over 10%. Chem. Sci. *11*, 2342–2349. https://doi.org/10.1039/C9SC05492H.

Demas, J.N., Harris, E.W., and McBride, R.P. (1977). Energy transfer from luminescent transition metal complexes to oxygen. J. Am. Chem. Soc. *99*, 3547–3551. https://doi.org/10.1021/ja00453a001.

Djurovich, P.I., Murphy, D., Thompson, M.E., Hernandez, B., Gao, R., Hunt, P.L., and Selke, M. (2007). Cyclometalated iridium and platinum complexes as singlet oxygen photosensitizers: quantum yields, quenching rates and correlation with electronic structures. Dalton Trans. *34*, 3763–3770. https://doi.org/10.1039/B704595F.

Dumur, F., Yuskevitch, Y., Wantz, G., Mayer, C.R., Bertin, D., and Gigmes, D. (2013). Light-emitting electrochemical cells based on a solution-processed multilayered device and an anionic iridium (III) complex. Synth. Met. *177*, 100–104. https://doi.org/10.1016/j.synthmet.2013.06.017.

Englman, R., and Jortner, J. (1970). The energy gap law for radiationless transitions in large molecules. Mol. Phys. *18*, 145–164. https://doi.org/10.1080/00268977000100171.

Escobedo, J.O., Rusin, O., Lim, S., and Strongin, R.M. (2010). NIR dyes for bioimaging applications. Curr. Opin. Chem. Biol. *14*, 64–70. https://doi.org/10.1016/j.cbpa.2009.10.022.

Frangioni, J. (2003). In vivo near-infrared fluorescence imaging. Curr. Opin. Chem. Biol. *7*,

626–634. https://doi.org/10.1016/j.cbpa.2003.08.007.

Freed, K.F., and Jortner, J. (1970). Multiphonon processes in the nonradiative decay of large molecules. J. Chem. Phys. *52*, 6272–6291. https://doi.org/10.1063/1.1672938.

Fu, G., Zheng, H., He, Y., Li, W., Lü, X., and He, H. (2018). Efficient near-infrared (NIR) polymer light-emitting diodes (PLEDs) based on heteroleptic iridium(III) complexes with post-modification effects of intramolecular hydrogen bonding or BF2-chelation. J. Mater. Chem. C *6*, 10589–10596. https://doi.org/10.1039/C8TC03432J.

Giebink, N.C., and Forrest, S.R. (2008). Quantum efficiency roll-off at high brightness in fluorescent and phosphorescent organic light emitting diodes. Phys. Rev. B *77*, 235215. https://doi.org/10.1103/PhysRevB.77.235215.

Guo, J., Zhou, J., Fu, G., He, Y., Li, W., and Lü, X. (2019). Two efficient near-infrared (NIR) luminescent [Ir(C^N)2(N^O)]-characteristic complexes with 8-hydroxyquinoline (8-Hq) as the ancillary ligand. Inorg. Chem. Commun. *101*, 69–73. https://doi.org/10.1016/j.inoche.2019.01.019.

Halcrow, M.A. (2013). Jahn–Teller distortions in transition metal compounds, and their importance in functional molecular and inorganic materials. Chem. Soc. Rev. *42*, 1784–1795. https://doi.org/10.1039/C2CS35253B.

Hao, Z., Li, M., Liu, Y., Wang, Y., Xie, G., and Liu, Y. (2018). Near-infrared emission of dinuclear iridium complexes with hole/electron transporting bridging and their monomer in solution-processed organic light-emitting diodes. Dyes Pigm. *149*, 315–322. https://doi.org/10.1016/j.dyepig.2017.09.061.

He, Y., Fu, G., Li, W., Wang, B., Miao, T., Tan, M., Feng, W., and Lü, X. (2020a). Efficient near-infrared (NIR) polymer light-emitting diode (PLED) based on the binuclear [(C^N)2Ir-(bis-N^O)-Ir(C^N)2] complex with aggregation-induced phosphorescent enhancement (AIPE) character. J. Lumin. *218*, 116847. https://doi.org/10.1016/j.jlumin.2019.116847.

He, Y., Li, W., Fu, G., Wang, B., Miao, T., Tan, M., Feng, W., Lü, X., and He, H. (2020b). Efficient and exclusively NIR-emitting (λem = 780 nm) [Ir(C^N)2(O^O)]-heteroleptic complexes with β-diketonate- or pyrazolonate-typed O^O-chelate ancillary. J. Lumin. *220*, 116983. https://doi.org/10.1016/j.jlumin.2019.116983.

Hemmer, E., Venkatachalam, N., Hyodo, H., Hattori, A., Ebina, Y., Kishimoto, H., and Soga, K. (2013). Upconverting and NIR emitting rare earth based nanostructures for NIR-bioimaging. Nanoscale *5*, 11339–11361. https://doi.org/10.1039/C3NR02286B.

Hemmer, E., Benayas, A., Légaré, F., and Vetrone, F. (2016). Exploiting the biological windows: current perspectives on fluorescent bioprobes emitting above 1000 nm. Nanoscale Horizon. *1*, 168–184. https://doi.org/10.1039/C5NH00073D.

Hilderbrand, S.A., and Weissleder, R. (2010). Near-infrared fluorescence: application to in vivo molecular imaging. Curr. Opin. Chem. Biol. *14*, 71–79. https://doi.org/10.1016/j.cbpa.2009.09.029.

Ho, P.-Y., Ho, C.-L., and Wong, W.-Y. (2020). Recent advances of iridium(III) metallophosphors for health-related applications. Coord. Chem. Rev. *413*, 213267. https://doi.org/10.1016/j.ccr.2020.213267.

Huang, W.-T., Yoon, S.-Y., Wu, B.-H., Lu, K.-M., Lin, C.-M., Yang, H., and Liu, R.-S. (2020). Ultra-broadband near-infrared emission CuInS2/ZnS quantum dots with high power efficiency and stability for the theranostic applications of mini light-emitting diodes. Chem. Commun. *56*, 8285–8288. https://doi.org/10.1039/D0CC03030A.

Huh, J.-S., Kim, K.-H., and Kim, J.-J. (2020). Emitting dipole orientation and molecular orientation of homoleptic Ir(III) complexes. Org. Electronics *82*, 105715. https://doi.org/10.1016/j.orgel.2020.105715.

Ikawa, S., Yagi, S., Maeda, T., Nakazumi, H., Fujiwara, H., Koseki, S., and Sakurai, Y. (2013). Photo- and electroluminescence from deep-red and near-infrared-phosphorescent tris-cyclometalated iridium(III) complexes bearing largely π-extended ligands. Inorg. Chem. Commun. *38*, 14–19. https://doi.org/10.1016/j.inoche.2013.09.075.

Jahn, H.A., and Teller, E. (1937). Stability of polyatomic molecules in degenerate electronic states - I—Orbital degeneracy. Proc. R. Soc. Lond. A *161*, 220–235. https://doi.org/10.1098/rspa.1937.0142.

Jin, C., Guan, R., Wu, J., Yuan, B., Wang, L., Huang, J., Wang, H., Ji, L., and Chao, H. (2017). Rational design of NIR-emitting iridium(iii) complexes for multimodal phosphorescence imaging of mitochondria under two-photon excitation. Chem. Commun. *53*, 10374–10377. https://doi.org/10.1039/C7CC05193J.

Jin, Y., Xue, J., Qiao, J., and Zhang, F. (2019a). Investigation on voltage loss in organic triplet photovoltaic devices based on Ir complexes. J. Mater. Chem. C *7*, 15049–15056. https://doi.org/10.1039/C9TC04914B.

Jin, Y., Zhang, Y., Liu, Y., Xue, J., Li, W., Qiao, J., and Zhang, F. (2019b). Limitations and perspectives on triplet-material-based organic photovoltaic devices. Adv. Mater. *31*, 1900690. https://doi.org/10.1002/adma.201900690.

Kabir, E., Wu, Y., Sittel, S., Nguyen, B.-L., and Teets, T.S. (2020). Improved deep-red phosphorescence in cyclometalated iridium complexes via ancillary ligand modification. Inorg. Chem. Front. *7*, 1362–1373. https://doi.org/10.1039/C9QI01584A.

Kalinowski, J., Stampor, W., Mężyk, J., Cocchi, M., Virgili, D., Fattori, V., and Di Marco, P. (2002). Quenching effects in organic electrophosphorescence. Phys. Rev. B *66*, 235321. https://doi.org/10.1103/PhysRevB.66.235321.

Kalinowski, J., Stampor, W., Szymtkowski, J., Virgili, D., Cocchi, M., Fattori, V., and Sabatini, C. (2006). Coexistence of dissociation and annihilation of excitons on charge carriers in organic phosphorescent emitters. Phys. Rev. B *74*, 085316. https://doi.org/10.1103/PhysRevB.74.085316.

Kesarkar, S., Mróz, W., Penconi, M., Pasini, M., Destri, S., Cazzaniga, M., Ceresoli, D., Mussini,

P.R., Baldoli, C., Giovanella, U., and Bossi, A. (2016). Near-IR emitting iridium(III) complexes with heteroaromatic β-diketonate ancillary ligands for efficient solution-processed OLEDs: structure–property correlations. Angew. Chem. Int. Ed. *55*, 2714–2718. https://doi.org/10.1002/anie.201509798.

Kim, K.-H., and Kim, J.-J. (2018). Origin and control of orientation of phosphorescent and TADF dyes for high-efficiency OLEDs. Adv. Mater. *30*, 1705600. https://doi.org/10.1002/adma.201705600.

Kim, S.-Y., Jeong, W.-I., Mayr, C., Park, Y.-S., Kim, K.-H., Lee, J.-H., Moon, C.-K., Brütting, W., and Kim, J.-J. (2013). Organic light-emitting diodes with 30% external quantum efficiency based on a horizontally oriented emitter. Adv. Funct. Mater. *23*, 3896–3900. https://doi.org/10.1002/adfm.201300104.

Kim, H.U., Sohn, S., Choi, W., Kim, M., Ryu, S.U., Park, T., Jung, S., and Bejoymohandas, K.S. (2018a). Substituents engineered deep-red to near-infrared phosphorescence from tris-heteroleptic iridium(iii) complexes for solution processable red-NIR organic light-emitting diodes. J. Mater. Chem. C *6*, 10640–10658. https://doi.org/10.1039/C8TC04321C.

Kim, J.H., Yun, J.H., and Lee, J.Y. (2018b). Recent progress of highly efficient red and near-infrared thermally activated delayed fluorescent emitters. Adv. Opt. Mater. *6*, 1800255. https://doi.org/10.1002/adom.201800255.

Kim, Y.-I., Yun, S.-J., Kim, D., and Kang, S.K. (2018c). Structural and photoluminescent properties of near-infrared emissive bis(2,3-Diphenylbenzoquinoxalinato)(2-Pyrazinecarboxylato)ridium(III). Bull. Korean Chem. Soc. *39*, 133–136. https://doi.org/10.1002/bkcs.11357.

Kim, H.U., Jang, H.J., Choi, W., Park, S., Park, T., Lee, J.Y., and Bejoymohandas, K.S. (2020a). Aggregation-induced phosphorescence enhancement in deep-red and near-infrared emissive iridium(III) complexes for solution-processable OLEDs. J. Mater. Chem. C *8*, 4789–4800. https://doi.org/10.1039/C9TC06813A.

Kim, J.S., Jeong, D., Bae, H.J., Jung, Y., Nam, S., Kim, J.W., Ihn, S., Kim, J., Son, W., Choi, H., and Kim, S. (2020b). Improved efficiency and stability of blue phosphorescent organic light emitting diodes by enhanced orientation of homoleptic cyclometalated Ir(III) complexes. Adv. Opt. Mater. *8*, 2001103. https://doi.org/10.1002/adom.202001103.

Kimachi, S., Satomi, R., Miki, H., Maeda, K., Azumi, T., and Onishi, M. (1997). Excited-state properties of the ligand-localized 3ππ* state of cyclometalated Ruthenium(II) complexes. J. Phys. Chem. A *101*, 345–349. https://doi.org/10.1021/jp961018s.

Kobayashi, H., Ogawa, M., Alford, R., Choyke, P.L., and Urano, Y. (2010). New strategies for fluorescent probe design in medical diagnostic imaging. Chem. Rev. *110*, 2620–2640. https://doi.org/10.1021/cr900263j.

Kober, E.M., Caspar, J.V., Lumpkin, R.S., and Meyer, T.J. (1986). Application of the energy gap law to excited-state decay of osmium(II)-polypyridine complexes: calculation of relative

nonradiative decay rates from emission spectral profiles. J. Phys. Chem. 90, 3722–3734. https://doi.org/10.1021/j100407a046.

Lai, P., and Teets, T.S. (2019). Ancillary ligand effects on red-emitting cyclometalated iridium complexes. Chem. A Eur. J. 25, 6026–6037. https://doi.org/10.1002/chem.201900829.

Lai, P.-N., Brysacz, C.H., Alam, M.K., Ayoub, N.A., Gray, T.G., Bao, J., and Teets, T.S. (2018). Highly efficient red-emitting bis-cyclometalated iridium complexes. J. Am. Chem. Soc. 140, 10198–10207. https://doi.org/10.1021/jacs.8b04841.

Lai, P.-N., Yoon, S., and Teets, T.S. (2020). Efficient near-infrared luminescence from bis-cyclometalated iridium(iii) complexes with rigid quinoline-derived ancillary ligands. Chem. Commun. 56, 8754–8757. https://doi.org/10.1039/D0CC02745F.

Lamansky, S., Djurovich, P., Murphy, D., Abdel-Razzaq, F., Kwong, R., Tsyba, I., Bortz, M., Mui, B., Bau, R., and Thompson, M.E. (2001a). Synthesis and characterization of phosphorescent cyclometalated iridium complexes. Inorg. Chem. 40, 1704–1711. https://doi.org/10.1021/ic0008969.

Lamansky, S., Djurovich, P., Murphy, D., Abdel-Razzaq, F., Lee, H.-E., Adachi, C., Burrows, P.E., Forrest, S.R., and Thompson, M.E. (2001b). Highly phosphorescent bis-cyclometalated iridium complexes: synthesis, photophysical characterization, and use in organic light emitting diodes. J. Am. Chem. Soc. 123, 4304–4312. https://doi.org/10.1021/ja003693s.

Li, G.-N., Zou, Y., Yang, Y.-D., Liang, J., Cui, F., Zheng, T., Xie, H., and Niu, Z.-G. (2014). Deep-red phosphorescent iridium(III) complexes containing 1-(Benzo[b] thiophen-2-yl) isoquinoline ligand: synthesis, photophysical and electrochemical properties and DFT calculations. J. Fluorescence 24, 1545–1552. https://doi.org/10.1007/s10895-014-1443-7.

Li, T.-Y., Wu, J., Wu, Z.-G., Zheng, Y.-X., Zuo, J.-L., and Pan, Y. (2018). Rational design of phosphorescent iridium(III) complexes for emission color tunability and their applications in OLEDs. Coord. Chem. Rev. 374, 55–92. https://doi.org/10.1016/j.ccr.2018.06.014.

Li, Y., Wu, Y., Chen, L., Zeng, H., Chen, X., Lun, W., Fan, X., and Wong, W.-Y. (2019). A time-resolved near-infrared phosphorescent iridium(iii) complex for fast and highly specific peroxynitrite detection and bioimaging applications. J. Mater. Chem. B 7, 7612–7618. https://doi.org/10.1039/C9TB01673B.

Li, Y., Wu, Y., Wu, J., Lun, W., Zeng, H., and Fan, X. (2020). A near-infrared phosphorescent iridium(iii) complex for fast and time-resolved detection of cysteine and homocysteine. Analyst 145, 2238–2244. https://doi.org/10.1039/C9AN02469G.

Liang, B., Yu, Z., Zhuang, X., Wang, J., Wei, J., Ye, K., Zhang, Z., Liu, Y., and Wang, Y. (2020). Achieving high-performance pure-red electrophosphorescent iridium(III) complexes based on optimizing ancillary ligands. Chem. A Eur. J. 26, 4410–4418. https://doi.org/10.1002/chem.201905690.

Liu, Y., Zhang, P., Fang, X., Wu, G., Chen, S., Zhang, Z., Chao, H., Tan, W., and Xu, L. (2017).

Near-infrared emitting iridium(iii) complexes for mitochondrial imaging in living cells. Dalton Trans. 46, 4777–4785. https://doi.org/10.1039/C7DT00255F.

Liu, F., Wen, J., Chen, S.-S., and Sun, S. (2018a). A luminescent bimetallic iridium(iii) complex for ratiometric tracking intracellular viscosity. Chem. Commun. 54, 1371–1374. https://doi.org/10.1039/C7CC09723A.

Liu, Y., Hao, Z., Meng, F., Wang, P., Yang, L., Wang, Y., Pei, Y., and Su, S. (2018b). Efficient near-infrared emission of π-extended cyclometalated iridium complexes based on pyrene in solution-processed polymer light-emitting diode. Chem. Phys. Lett. 699, 99–106. https://doi.org/10.1016/j.cplett.2018.03.046.

Lo, K.K.-W. (2015). Luminescent rhenium(I) and iridium(III) polypyridine complexes as biological probes, imaging reagents, and photocytotoxic agents. Acc. Chem. Res. 48, 2985–2995. https://doi.org/10.1021/acs.accounts.5b00211.

Lo, S.-C., Shipley, C.P., Bera, R.N., Harding, R.E., Cowley, A.R., Burn, P.L., and Samuel, I.D.W. (2006). Blue phosphorescence from iridium(III) complexes at room temperature. Chem. Mater. 18, 5119–5129. https://doi.org/10.1021/cm061173b.

Ma, D., Tsuboi, T., Qiu, Y., and Duan, L. (2017). Recent progress in ionic iridium(III) complexes for organic electronic devices. Adv. Mater. 29, 1603253. https://doi.org/10.1002/adma.201603253.

Ma, Y., Zhang, Y., Cai, S., Han, Z., Liu, X., Wang, F., Cao, Y., Wang, Z., Li, H., Chen, Y., and Feng, X. (2020). Flexible hybrid electronics for digital healthcare. Adv. Mater. 32, 1902062. https://doi.org/10.1002/adma.201902062.

Mi, B.X., Wang, P.F., Gao, Z.Q., Lee, C.S., Lee, S.T., Hong, H.L., Chen, X.M., Wong, M.S., Xia, P.F., Cheah, K.W., et al. (2009). Strong luminescent iridium complexes with C^N=N structure in ligands and their potential in efficient and thermally stable phosphorescent OLEDs. Adv. Mater. 21, 339–343. https://doi.org/10.1002/adma.200801604.

Miki, H., Shimada, M., Azumi, T., Brozik, J.A., and Crosby, G.A. (1993). Effect of the ligand-field strength on the radiative properties of the ligand-localized 3.pi..pi.* state of rhodium complexes with 1,10-phenanthroline: proposed role of dd states. J. Phys. Chem. 97, 11175–11179. https://doi.org/10.1021/j100145a010.

Neyts, K.A. (1998). Simulation of light emission from thin-film microcavities. J. Opt. Soc. Am A 15, 962–971. https://doi.org/10.1364/JOSAA.15.000962.

Nowy, S., Krummacher, B.C., Frischeisen, J., Reinke, N.A., and Brütting, W. (2008). Light extraction and optical loss mechanisms in organic light-emitting diodes: influence of the emitter quantum efficiency. J. Appl. Phys. 104, 123109. https://doi.org/10.1063/1.3043800.

Obara, S., Itabashi, M., Okuda, F., Tamaki, S., Tanabe, Y., Ishii, Y., Nozaki, K., and Haga, M. (2006). Highly phosphorescent iridium complexes containing both Tridentate bis(benzimidazolyl)-benzene or -pyridine and bidentate phenylpyridine: synthesis, photophysical

properties, and theoretical study of Ir-Bis(benzimidazolyl)benzene complex. Inorg. Chem. 45, 8907–8921. https://doi.org/10.1021/ic060796o.

Palmer, J.H., Durrell, A.C., Gross, Z., Winkler, J.R., and Gray, H.B. (2010). Near-IR phosphorescence of iridium(III) corroles at ambient temperature. J. Am. Chem. Soc. 132, 9230–9231. https://doi.org/10.1021/ja101647t.

Pradhan, S., Di Stasio, F., Bi, Y., Gupta, S., Christodoulou, S., Stavrinadis, A., and Konstantatos, G. (2019). High-efficiency colloidal quantum dot infrared light-emitting diodes via engineering at the supra-nanocrystalline level. Nat. Nanotechnol. 14, 72–79. https://doi.org/10.1038/s41565-018-0312-y.

Qian, G., and Wang, Z.Y. (2010). Near-infrared organic compounds and emerging applications. Chem. Asian J. 5, 1006–1029. https://doi.org/10.1002/asia.200900596.

Qiao, J., Duan, L., Tang, L., He, L., Wang, L., and Qiu, Y. (2009). High-efficiency orange to near-infrared emissions from bis-cyclometalated iridium complexes with phenyl-benzoquinoline isomers as ligands. J. Mater. Chem. 19, 6573. https://doi.org/10.1039/b906675f.

Rausch A.F., Homeier H., Djurovich P.I., Thompson M.E., Yersin H. (2007). Spin-orbit coupling routes and OLED performance: studies of blue-light emitting Ir(III) and Pt (II) complexes, Proc. SPIE 6655, Organic Light Emitting Materials and Devices XI, 66550F. https://doi.org/10.1117/12.731225.

Rausch, A.F., Homeier, H.H.H., and Yersin, H. (2010). Organometallic Pt(II) and Ir(III) triplet emitters for OLED applications and the role of spin–orbit coupling: a study based on high-resolution optical spectroscopy. In Photophysics of Organometallics, A.J. Lees, ed. (Berlin, Heidelberg: Springer Berlin Heidelberg), pp. 193–235.

Reineke, S., Schwartz, G., Walzer, K., and Leo, K. (2007a). Reduced efficiency roll-off in phosphorescent organic light emitting diodes by suppression of triplet-triplet annihilation. Appl. Phys. Lett. 91, 123508. https://doi.org/10.1063/1.2786840.

Reineke, S., Walzer, K., and Leo, K. (2007b). Triplet-exciton quenching in organic phosphorescent light-emitting diodes with Ir-based emitters. Phys. Rev. B 75, 125328. https://doi.org/10.1103/PhysRevB.75.125328.

Reineke, S., Schwartz, G., Walzer, K., Falke, M., and Leo, K. (2009). Highly phosphorescent organic mixed films: the effect of aggregation on triplet-triplet annihilation. Appl. Phys. Lett. 94, 163305. https://doi.org/10.1063/1.3123815.

Robinson, G.W., and Frosch, R.P. (1963). Electronic excitation transfer and relaxation. J. Chem. Phys. 38, 1187–1203. https://doi.org/10.1063/1.1733823.

Sajoto, T., Djurovich, P.I., Tamayo, A.B., Oxgaard, J., Goddard, W.A., and Thompson, M.E. (2009). Temperature dependence of blue phosphorescent cyclometalated Ir(III) complexes. J. Am. Chem. Soc. 131, 9813–9822. https://doi.org/10.1021/ja903317w.

Schmid, M., Harms, K., Degitz, C., Morgenstern, T., Hofmann, A., Friederich, P., Johannes, H.-H., Wenzel, W., Kowalsky, W., and Brütting, W. (2020). Optical and electrical measurements reveal the orientation mechanism of homoleptic iridium-carbene complexes. ACS Appl. Mater. Interfaces 12, 51709–51718. https://doi.org/10.1021/acsami.0c14613.

Schweitzer, C., and Schmidt, R. (2003). Physical mechanisms of generation and deactivation of singlet oxygen. Chem. Rev. 103, 1685–1758. https://doi.org/10.1021/cr010371d.

Shafikov, M.Z., Zaytsev, A.V., and Kozhevnikov, V.N. (2021). Halide-enhanced spin–orbit coupling and the phosphorescence rate in Ir(III) complexes. Inorg. Chem. 60, 642–650. https://doi.org/10.1021/acs.inorgchem.0c02469.

Shafikov, M.Z., Zaytsev, A.V., Suleymanova, A.F., Brandl, F., Kowalczyk, A., Gapińska, M., Kowalski, K., Kozhevnikov, V.N., and Czerwieniec, R. (2020). Near infrared phosphorescent dinuclear Ir(III) complex exhibiting unusually slow intersystem crossing and dual emissive behavior. J. Phys. Chem. Lett. 11, 5849–5855. https://doi.org/10.1021/acs.jpclett.0c01276.

Shahnawaz, Swayamprabha, S.S., Nagar, M.R., Yadav, R.A.K., Gull, S., Dubey, D.K., and Jou, J.-H. (2019). Hole-transporting materials for organic light-emitting diodes: an overview. J. Mater. Chem. C 7, 7144–7158. https://doi.org/10.1039/C9TC01712G.

Siebrand, W. (1967). Radiationless transitions in polyatomic molecules. I. Calculation of Franck—Condon factors. J. Chem. Phys. 46, 440–447. https://doi.org/10.1063/1.1840685.

Smith, A.M., Mancini, M.C., and Nie, S. (2009). Second window for in vivo imaging. Nat. Nanotechnol. 4, 710–711. https://doi.org/10.1038/nnano.2009.326.

Song, D., Zhao, S., Luo, Y., and Aziz, H. (2010). Causes of efficiency roll-off in phosphorescent organic light emitting devices: triplet-triplet annihilation versus triplet-polaron quenching. Appl. Phys. Lett. 97, 243304. https://doi.org/10.1063/1.3527085.

Stufkens, D.J., and Vlček, A. (1998). Ligand-dependent excited state behaviour of Re(I) and Ru(II) carbonyl–diimine complexes. Coord. Chem. Rev. 177, 127–179. https://doi.org/10.1016/S0010-8545(98)00132-5.

Su, Y.-J., Huang, H.-L., Li, C.-L., Chien, C.-H., Tao, Y.-T., Chou, P.-T., Datta, S., and Liu, R.-S. (2003). Highly efficient red electrophosphorescent devices based on iridium isoquinoline complexes: remarkable external quantum efficiency over a wide range of current. Adv. Mater. 15, 884–888. https://doi.org/10.1002/adma.200304630.

Su, N., Li, F.-L., and Zheng, Y.-X. (2020). Four-membered red iridium(iii) complexes with Ir–S–C–S structures for efficient organic light-emitting diodes. J. Mater. Chem. C 8, 7411–7416. https://doi.org/10.1039/D0TC01312A.

Szafraniec-Gorol, G., Słodek, A., Filapek, M., Boharewicz, B., Iwan, A., Jaworska, M., Żur, L., Sołtys, M., Pisarska, J., Grudzka-Flak, I., et al. (2015). Novel iridium(III) complexes based on 2-(2,2'-bithien-5-yl)-quinoline. Synthesis,

photophysical, photochemical and DFT studies. Mater. Chem. Phys. 162, 498–508. https://doi.org/10.1016/j.matchemphys.2015.06.020.

Tamayo, A.B., Alleyne, B.D., Djurovich, P.I., Lamansky, S., Tsyba, I., Ho, N.N., Bau, R., and Thompson, M.E. (2003). Synthesis and characterization of facial and meridional tris-cyclometalated iridium(III) complexes. J. Am. Chem. Soc. 125, 7377–7387. https://doi.org/10.1021/ja034537z.

Tao, R., Qiao, J., Zhang, G., Duan, L., Wang, L., and Qiu, Y. (2012). Efficient near-infrared-emitting cationic iridium complexes as dopants for OLEDs with small efficiency roll-off. J. Phys. Chem. C 116, 11658–11664. https://doi.org/10.1021/jp301740c.

Tao, R., Qiao, J., Zhang, G., Duan, L., Chen, C., Wang, L., and Qiu, Y. (2013). High-efficiency near-infrared organic light-emitting devices based on an iridium complex with negligible efficiency roll-off. J. Mater. Chem. C 1, 6446–6454. https://doi.org/10.1039/C3TC30866A.

Tong, B., Mei, Q., Wang, S., Fang, Y., Meng, Y., and Wang, B. (2008). Nearly 100% internal phosphorescence efficiency in a polymer light-emitting diode using a new iridium complex phosphor. J. Mater. Chem. 18, 1636–1639.

Treadway, J.A., Loeb, B., Lopez, R., Anderson, P.A., Keene, F.R., and Meyer, T.J. (1996). Effect of delocalization and rigidity in the acceptor ligand on MLCT excited-state decay. Inorg. Chem. 35, 2242–2246. https://doi.org/10.1021/ic950961s.

Tsuboyama, A., Iwawaki, H., Furugori, M., Mukaide, T., Kamatani, J., Igawa, S., Moriyama, T., Miura, S., Takiguchi, T., Okada, S., et al. (2003). Homoleptic cyclometalated iridium complexes with highly efficient red phosphorescence and application to organic light-emitting diode. J. Am. Chem. Soc. 125, 12971–12979. https://doi.org/10.1021/ja034732d.

Tuong Ly, K., Chen-Cheng, R.-W., Lin, H.-W., Shiau, Y.-J., Liu, S.-H., Chou, P.-T., Tsao, C.-S., Huang, Y.-C., and Chi, Y. (2017). Near-infrared organic light-emitting diodes with very high external quantum efficiency and radiance. Nat. Photon. 11, 63–68. https://doi.org/10.1038/nphoton.2016.230.

Vasilopoulou, M., Kim, H.P., Kim, B.S., Papadakis, M., Ximim Gavim, A.E., Macedo, A.G., Jose da Silva, W., Schneider, F.K., Mat Teridi, M.A., Coutsolelos, A.G., and bin Mohd Yusoff, Abd, R. (2020). Efficient colloidal quantum dot light-emitting diodes operating in the second near-infrared biological window. Nat. Photon. 14, 50–56. https://doi.org/10.1038/s41566-019-0526-z.

Wang, J., Xue, J., Yan, Z., Zhang, S., Qiao, J., and Zhang, X. (2017a). Photoluminescence lifetime imaging of synthesized proteins in living cells using an iridium-alkyne probe. Angew. Chem. Int. Ed. 56, 14928–14932. https://doi.org/10.1002/anie.201708566.

Wang, L., Yin, H., Cui, P., Hetu, M., Wang, C., Monro, S., Schaller, R.D., Cameron, C.G., Liu, B., Kilina, S., et al. (2017b). Near-infrared-emitting heteroleptic cationic iridium complexes derived from 2,3-diphenylbenzo[g]quinoxaline as in vitro theranostic photodynamic therapy agents. Dalton Trans. 46, 8091–8103. https://doi.org/10.1039/C7DT00913E.

Wang, S.F., Yuan, Y., Wei, Y., Chan, W., Fu, L., Su, B., Chen, I., Chou, K., Chen, P., Hsu, H., et al. (2020). Highly efficient near-infrared electroluminescence up to 800 nm using platinum(II) phosphors. Adv. Funct. Mater. 30, 2002173. https://doi.org/10.1002/adfm.202002173.

Wei, Y.-C., Wang, S.F., Hu, Y., Liao, L.-S., Chen, D.-G., Chang, K.-H., Wang, C.-W., Liu, S.-H., Chan, W.-H., Liao, J.-L., et al. (2020). Overcoming the energy gap law in near-infrared OLEDs by exciton–vibration decoupling. Nat. Photon. 14, 570–577. https://doi.org/10.1038/s41566-020-0653-6.

Weissleder, R. (2001). A clearer vision for in vivo imaging. Nat. Biotechnol. 19, 316–317. https://doi.org/10.1038/86684.

Whittle, C.E., Weinstein, J.A., George, M.W., and Schanze, K.S. (2001). Photophysics of diimine platinum(II) bis-acetylide complexes. Inorg. Chem. 40, 4053–4062. https://doi.org/10.1021/ic0102182.

Williams, E.L., Li, J., and Jabbour, G.E. (2006). Organic light-emitting diodes having exclusive near-infrared electrophosphorescence. Appl. Phys. Lett. 89, 083506. https://doi.org/10.1063/1.2335275.

Wu, Y., Wu, R., Li, H., Zeng, H., Li, Y., Wang, Q., Shi, M., and Fan, X. (2017). A near-infrared phosphorescent iridium(iii) complex for imaging of cysteine and homocysteine in living cells and in vivo. RSC Adv. 7, 52621–52625. https://doi.org/10.1039/C7RA09798K.

Wu, W., Zhang, C., Rees, T.W., Liao, X., Yan, X., Chen, Y., Ji, L., and Chao, H. (2020). Lysosome-targeting iridium(III) probe with near-infrared emission for the visualization of NO/O2●-crosstalk via in vivo peroxynitrite imaging. Anal. Chem. 92, 6003–6009. https://doi.org/10.1021/acs.analchem.0c00259.

Xiang, H., Cheng, J., Ma, X., Zhou, X., and Chruma, J.J. (2013). Near-infrared phosphorescence: materials and applications. Chem. Soc. Rev. 42, 6128. https://doi.org/10.1039/c3cs60029g.

Xin, L., Xue, J., Lei, G., and Qiao, J. (2015). Efficient near-infrared-emitting cationic iridium complexes based on highly conjugated cyclometalated benzo[g]phthalazine derivatives. RSC Adv. 5, 42354–42361. https://doi.org/10.1039/C5RA04511H.

Xu, W., Hu, Q., Bai, S., Bao, C., Miao, Y., Yuan, Z., Borzda, T., Barker, A.J., Tyukalova, E., Hu, Z., et al. (2019). Rational molecular passivation for high-performance perovskite light-emitting diodes. Nat. Photon. 13, 418–424. https://doi.org/10.1038/s41566-019-0390-x.

Xue, J., Xin, L., Hou, J., Duan, L., Wang, R., Wei, Y., and Qiao, J. (2017). Homoleptic facial Ir(III) complexes via facile synthesis for high-efficiency and low-roll-off near-infrared organic light-emitting diodes over 750 nm. Chem. Mater. 29, 4775–4782. https://doi.org/10.1021/acs.chemmater.7b00518.

Yan, Z., Wang, J., Zhang, Y., Zhang, S., Qiao, J., and Zhang, X. (2018). An iridium complex-based probe for photoluminescence lifetime imaging of human carboxylesterase 2 in living cells. Chem.

Commun. *54*, 9027–9030. https://doi.org/10.1039/C8CC04481C.

Yan, Z., Xue, J., Zhou, M., Wang, J., Zhang, Y., Wang, Y., Qiao, J., He, Y., Li, P., Zhang, S., and Zhang, X. (2021). Dynamic monitoring of phase-separated biomolecular condensates by photoluminescence lifetime imaging. Anal. Chem. https://doi.org/10.1021/acs.analchem.0c05011.

Yersin, H., Rausch, A.F., Czerwieniec, R., Hofbeck, T., and Fischer, T. (2011). The triplet state of organo-transition metal compounds. Triplet harvesting and singlet harvesting for efficient OLEDs. Coord. Chem. Rev. *255*, 2622–2652. https://doi.org/10.1016/j.ccr.2011.01.042.

Yoshihara, T., Murayama, S., Masuda, T., Kikuchi, T., Yoshida, K., Hosaka, M., and Tobita, S. (2015). Mitochondria-targeted oxygen probes based on cationic iridium complexes with a 5-amino-1, 10-phenanthroline ligand. J. Photochem. Photobiol. A Chem. *299*, 172–182. https://doi.org/10.1016/j.jphotochem.2014.11.004.

You, Y., and Park, S.Y. (2009). Phosphorescent iridium(iii) complexes: toward high phosphorescence quantum efficiency through ligand control. Dalton Trans. *8*, 1267–1282. https://doi.org/10.1039/B812281D.

You, C., Liu, D., Meng, F., Wang, Y., Yu, J., Wang, S., Su, S., and Zhu, W. (2019). Iridium(III) phosphors with rigid fused-heterocyclic chelating architectures for efficient deep-red/near-infrared emissions in polymer light-emitting diodes. J. Mater. Chem. C *7*, 10961–10971. https://doi.org/10.1039/C9TC03645H.

You, C., Liu, D., Yu, J., Tan, H., Zhu, M., Zhang, B., Liu, Y., Wang, Y., and Zhu, W. (2020a). Boosting efficiency of near-infrared emitting iridium(III) phosphors by Administrating their π–π conjugation effect of core–shell structure in solution-processed OLEDs. Adv. Opt. Mater. *8*, 2000154. https://doi.org/10.1002/adom.202000154.

You, C., Liu, D., Zhu, M., Yu, J., Zhang, B., Liu, Y., Wang, Y., and Zhu, W. (2020b). σ–π and p–π conjugation induced NIR-emitting iridium(III) complexes anchored by flexible side chains in a rigid dibenzo[a,c]phenazine moiety and their application in highly efficient solution-processable NIR-emitting devices. J. Mater. Chem. C *8*, 7079–7088. https://doi.org/10.1039/D0TC00479K.

Yu, J., Tan, H., Meng, F., Lv, K., Zhu, W., and Su, S. (2016). Benzotriazole-containing donor–acceptor–acceptor type cyclometalated iridium(III) complex for solution-processed near-infrared polymer light emitting diodes. Dyes Pigm. *131*, 231–238. https://doi.org/10.1016/j.dyepig.2016.04.021.

Yu, J., Xu, C., Meng, F., Tan, H., Li, M., and Zhu, W. (2019). Triphenylamine-functionalized iridium(III) complexes for near-infrared phosphorescent organic light emitting diodes. Dyes Pigm. *166*, 307–313. https://doi.org/10.1016/j.dyepig.2019.03.047.

Yu, J., Li, M., Xu, C., Meng, F., Cao, J., Tan, H., and Zhu, W. (2020). Near-infrared cyclometalated iridium(III) complexes with bipolar features for efficient OLEDs via solution-processing. Dalton Trans. *49*, 8785–8790. https://doi.org/10.1039/D0DT01415J.

Yuan, L., Lin, W., Zheng, K., He, L., and Huang, W. (2012). Far-red to near infrared analyte-responsive fluorescent probes based on organic fluorophore platforms for fluorescence imaging. Chem. Soc. Rev. *42*, 622–661. https://doi.org/10.1039/C2CS35313J.

Zampetti, A., Minotto, A., and Cacialli, F. (2019). Near-infrared (NIR) organic light-emitting diodes (OLEDs): challenges and opportunities. Adv. Funct. Mater. *29*, 1807623. https://doi.org/10.1002/adfm.201807623.

Zhang, H., and Rogers, J.A. (2019). Recent advances in flexible inorganic light emitting diodes: from materials design to Integrated optoelectronic platforms. Adv. Opt. Mater. *7*, 1800936. https://doi.org/10.1002/adom.201800936.

Zhang, G., Zhang, H., Gao, Y., Tao, R., Xin, L., Yi, J., Li, F., Liu, W., and Qiao, J. (2014). Near-infrared-emitting iridium(III) complexes as phosphorescent dyes for live cell imaging. Organometallics *33*, 61–68. https://doi.org/10.1021/om400676h.

Zhang, K.Y., Yu, Q., Wei, H., Liu, S., Zhao, Q., and Huang, W. (2018a). Long-lived emissive probes for time-resolved photoluminescence bioimaging and biosensing. Chem. Rev. *118*, 1770–1839. https://doi.org/10.1021/acs.chemrev.7b00425.

Zhang, Y., Wang, Y., Song, J., Qu, J., Li, B., Zhu, W., and Wong, W.-Y. (2018b). Near-infrared emitting materials via harvesting triplet excitons: molecular design, properties, and application in organic light emitting diodes. Adv. Opt. Mater. *6*, 1800466. https://doi.org/10.1002/adom.201800466.

Zhang, Y., Li, Q., Cai, M., Xue, J., and Qiao, J. (2020). An 850 nm pure near-infrared emitting iridium complex for solution-processed organic light-emitting diodes. J. Mater. Chem. C *8*, 8484–8492. https://doi.org/10.1039/D0TC01614D.

Zhen, X., Qu, R., Chen, W., Wu, W., and Jiang, X. (2021). The development of phosphorescent probes for *in vitro* and *in vivo* bioimaging. Biomater. Sci. *9*, 285–300. https://doi.org/10.1039/D0BM00819B.

Zheng, X., Wang, X., Mao, H., Wu, W., Liu, B., and Jiang, X. (2015). Hypoxia-specific ultrasensitive detection of tumours and cancer cells in vivo. Nat. Commun. *6*, 5834. https://doi.org/10.1038/ncomms6834.

Zheng, X., Mao, H., Huo, D., Wu, W., Liu, B., and Jiang, X. (2017). Successively activatable ultrasensitive probe for imaging tumour acidity and hypoxia. Nat. Biomed. Eng. *1*, 0057. https://doi.org/10.1038/s41551-017-0057.

Zhong, C., Duan, C., Huang, F., Wu, H., and Cao, Y. (2011). Materials and devices toward fully solution processable organic light-emitting diodes. Chem. Mater. *23*, 326–340. https://doi.org/10.1021/cm101937p.

Zhou, J., Liu, Z., and Li, F. (2012). Upconversion nanophosphors for small-animal imaging. Chem. Soc. Rev. *41*, 1323–1349. https://doi.org/10.1039/C1CS15187H.

Zhou, X., Burn, P.L., and Powell, B.J. (2016). Bond fission and non-radiative decay in iridium(III) complexes. Inorg. Chem. *55*, 5266–5273. https://doi.org/10.1021/acs.inorgchem.6b00219.

Zhou, J., Fu, G., He, Y., Ma, L., Li, W., Feng, W., and Lü, X. (2019a). Efficient and low-efficiency-roll-off near-infrared (NIR) polymer light-emitting diodes (PLEDs) based on an asymmetric binuclear iridium(III)-complex. J. Lumin. *209*, 427–434. https://doi.org/10.1016/j.jlumin.2019.02.045.

Zhou, R., Lu, X., Yang, Q., and Wu, P. (2019b). Nanocrystals for large Stokes shift-based optosensing. Chin. Chem. Lett. *30*, 1843–1848. https://doi.org/10.1016/j.cclet.2019.07.062.